Modélisation micromagnétique de dynamique d'aimantation pilotée par transfert de spin dans des nanopiliers

Adrien Vaysset

UNIVERSITÉ DE GRENOBLE

THÈSE

pour obtenir le grade de

DOCTEUR DE L'UNIVERSITÉ DE GRENOBLE

Spécialité : Physique

Arrêté ministériel : 7 août 2006

Présentée par

Adrien VAYSSET

Thèse dirigée par **Jean-Christophe TOUSSAINT** et co-encadrée par **Liliana BUDA-PREJBEANU**

préparée au sein du

LABORATOIRE SPINTEC UMR 8191

dans l'**École Doctorale de Physique**

MICROMAGNETIC MODELLING OF SPIN-TRANSFER-DRIVEN MAGNETISATION DYNAMICS IN NANOPILLARS

Thèse soutenue publiquement le **7 Janvier 2013**, devant le jury composé de :

Dr. André THIAVILLE
Directeur de recherche CNRS, Rapporteur

Dr. Dafiné RAVELOSONA
Directeur de recherche CNRS, Rapporteur

Pr. Françoise HIPPERT
Professeur à l'Université de Grenoble, Membre

Pr. François ALOUGES
Professeur à l'École Polytechnique, Membre

Pr. Jean-Christophe TOUSSAINT
Professeur à l'Université de Grenoble, Directeur de Thèse

Dr. Liliana BUDA-PREJBEANU
Maître de Conférence à l'Université de Grenoble, Co-directrice de Thèse

Remerciements

Je tiens tout d'abord à remercier ma tutrice de thèse, Liliana Buda-Prejbeanu, pour m'avoir fait confiance durant ces trois années. Liliana, je te remercie pour avoir su me guider tout en me laissant la liberté d'approfondir les points qui me paraissaient plus intéressants ou plus importants. Je te suis aussi très reconnaissant pour ta volonté permanente de mettre en avant et de valoriser ton thésard. Je te remercie enfin pour ta gentillesse, ton écoute et ton soutien, y compris dans les moments les plus difficiles. Ton dynamisme et ton énergie sont pour moi un modèle que j'essaye de suivre au quotidien dans mon travail.

Je remercie également mon directeur de thèse, Jean-Christophe Toussaint, pour ses conseils avisés et ses remarques toujours très constructives. Jean-Christophe, je te remercie pour ton soutien permanent ainsi que pour ta patience et ta pédagogie lorsque tu me parlais de méthodes numériques et d'éléments finis. Je te remercie aussi pour tes nombreux encouragements qui m'ont beaucoup aidé pendant la difficile période de la rédaction.

Je remercie Alain Schuhl, directeur de Spintec jusqu'en 2010, pour m'avoir accueilli dans son laboratoire, ainsi que Jean-Pierre Nozières, actuel directeur de Spintec.

Je tiens à remercier les membres du jury : Françoise Hippert (présidente du jury), François Alouges, ainsi que les rapporteurs, André Thiaville et Dafiné Ravelosona, pour le temps qu'ils ont passé à lire et à commenter mon manuscrit. Je remercie Françoise Hippert également pour m'avoir orienté vers Spintec lorsque j'étais à la recherche d'un sujet de thèse. Je souhaite également adresser un grand merci à François Alouges pour sa collaboration et ses idées qui ont tant contribuée à faire de feeLLGood ce qu'il est aujourd'hui. Je voudrais aussi saluer la gentillesse et la disponibilité d'André Thiaville qui a porté beaucoup d'intérêt à mes "sauts en fréquence".

Je tiens à remercier Ursula Ebels pour ses remarques et ses nombreux conseils. Je suis aussi très reconnaissant envers Bernard Diény pour ses suggestions et ses commentaires toujours très éclairés. Merci aussi à Maïrbek Chshiev pour ses grandes qualités humaines et scientifiques, et merci à Olivier Klein pour son aide et pour les discussions que nous avons eues. J'adresse aussi un merci tout particulier à Daria Gusakova pour avoir toujours pris le temps de discuter avec moi des questions que je venais lui poser.

Je remercie Evaggelos Kritsikis dont le travail de thèse a permis de faire de feeLLGood un solveur rapide et précis, contribuant ainsi largement à la réussite de ma thèse. wag, je te remercie également pour ta bonne humeur et les longues discussions à Intermag Taïpeï.

Un grand merci à Helga Szambolics qui a eu la gentillesse et la patience de guider mes premiers pas dans le monde étrange du micromagnétisme. Merci Helga pour ton aide et pour ta sympathie !

Un merci particulier à Ioana Firastrau qui a rendu la salle de calcul bien plus chaleureuse durant ses séjours à Spintec. Merci Ioana pour les longues discussions (pas toujours scientifiques) que nous avons eues !

Un grand merci à Benjamin Séguret (alias “Grand Geek”) pour son aide précieuse avec les scripts PERL qui m'ont servi dans l'étude sur le renversement précessionnel.

There is one person I am extremely grateful to, because he has always been willing to share his knowledge and to offer his help. This person was taking so much of his time to help (me and many others in Spintec), that I often felt sorry to ask him (again) some help. I have had with this person very stimulating and fruitful scientific discussions, and I have to say that scientific discussion is what I enjoy the most in research. Felipe Garcia Sanchez, I want to thank you for this great collaboration and for your friendship. I have very much enjoyed working with you and hope we can work again together in the future. Thank you as well for contributing to the friendly atmosphere in Spintec!

Il y a beaucoup d'autres personnes que je souhaite remercier pour avoir donné à Spintec une ambiance si conviviale. Il y a évidemment mes co-bureaux : Michaël, Emeline, Gor et Julien. Mais je remercie aussi tous les autres : Alex (the English man), Lara, Elmer, Abhijit, HongXin, Emilie, Sylvain, Bertrand, Juan et Mario.

Je dois aussi remercier d'autres personnes qui n'ont pas grand chose à voir avec la spintronique... Je pense à la superbe bande de potes de PG, la “Chartreuse team” dont l'amitié compte évidemment beaucoup pour aider à franchir le cap de la thèse. Je remercie aussi ma mère et mon frère qui m'ont encouragé pendant ces trois ans. Et je rends hommage à mon père qui sera parti peu de temps avant que je ne devienne docteur.

Enfin, je veux remercier celle qui a été près de moi chaque jour, celle qui m'a supporté et qui m'a aidé à garder l'équilibre : Merci Hélène !

Résumé

Le but de cette thèse est double : tester un solveur micromagnétique utilisant les éléments finis (feeLLGood), et étudier la dynamique d'aimantation pilotée par transfert de spin dans le but de comprendre des mesures expérimentales de plusieurs composants spintroniques.

Deux schémas temporels implémentés dans le code ont été testés et comparés à d'autres solveurs, en particulier un code différences finies (ST_GL-FFT). Les comparaisons entre les résultats de simulations ont confimé la validité de feeLLGood, et ont montrés des artefacts numériques dans les simulations différences finies.

D'autres part, les simulations numériques ont permis des analyses approfondies de trois types de dispositifs spintroniques.

- Des sauts en fréquences ont été étudiés dans l'oscillateur à transfert de spin planaire. Grâce à des techniques de cartographies spectrales, les sauts ont été attribués à l'excitation de modes non-linéaires.

- Le diagramme d'état d'un oscillateur à transfert de spin composé d'un polariseur perpendiculaire et d'une couche libre planaire a été exploré, mettant en évidence plusieurs modes d'oscillation dépendant de l'état initial. De plus, le désaccord entre les simulations effectuées en différences finies et en éléments finis a montré l'effet d'un bord crennelé.

- La commutation précessionelle induite par couple de transfert de spin a été simulée pour comprendre l'influence du champ de fuite du polariseur sur la probabilité de renversement. Un bon accord avec les mesures expérimentales sur STT-MRAM a été obtenu.

Abstract

The goal of this PhD thesis has been two-fold: test a Finite Element micromagnetic solver (feeLLGood), and study spin-transfer-driven magnetisation dynamics to understand experimental measurements of several spintronic devices.

Two time schemes implemented in the code have been benchmarked against other solvers, in particular against a Finite Difference code (ST_GL-FFT). Comparisons of the simulation results confirmed the accuracy of feeLLGood and showed artefacts in Finite Difference simulations. On the other hand, numerical simulations have allowed in-depth analyses of three types of spintronic device.

- Frequency jumps have been studied in a planar Spin Torque Oscillator. Thanks to spectral mapping techniques, the jumps were shown to be linked to the excitation of non-linear modes.

- The state diagram of a perpendicular-polariser/planar-free-layer Spin Torque Oscillator has been explored, showing various oscillation modes depending on the initial state. Moreover, discrepancy between Finite Difference and Finite Element simulations showed the effect of a staircase-like edge.

- Precessional switching induced by spin transfer torque has been simulated to understand the influence of the polarisers stray field on the switching probability. A good agreement with experimental measurements of STT-MRAM has been found.

Contents

Introduction

Recent advances in characterisation techniques and fabrication of nanostructures has enabled the development of a very active field of research: *spintronics*, or *spin electronics*. In 1988, the discovery of the magnetoresistance effect by Albert Fert [2] and Peter Grünberg [3] led to several applications such as magnetic field sensor for read-heads and MRAM (Magnetic Random Access Memory). Eight years later, its reciprocal effect, the *spin transfer*, was theoretically established, giving promise to the control of magnetisation by a spin-polarised current. Manifest experimental demonstration of this effect was eventually carried out in 2000 [4], when switching was observed in nanopillars. Spin transfer is of interest in Spin Torque Oscillators, where a frequency-tuneable microwave signal is generated, but also to reverse magnetisation in STT-MRAM (Spin Transfer Torque MRAM). These non-volatile memory devices are much more energy-efficient than first generations of MRAM and can lead to a much higher bit density because generating an external magnetic field is no longer required. Spin transfer torque could also be used in another type of memory: the racetrack memory [5] which consists in an array of domain walls moving back and forth in a magnetic nanowire.

The magnetisation motion in such systems is very complex, with rapid and non-uniform variations of the magnetic state. Moreover, the magnetoresistance is very often the only piece of information accessible through experiments. Therefore, a thorough understanding of spin-transfer devices necessitates to simulate their magnetisation dynamics. Interest for micromagnetic simulations started to grow in the late 1990's with improvement of computers performance. Nowadays, they are commonly used to support the interpretation of experimental results. One of their main advantages is the possibility to vary easily the material parameters, the geometry, or any other "ingredient" in order to know its impact on the magnetisation motion. Doing so in experiments is much more intricate, but also more expensive. However, one should not expect micromagnetic simulations to provide quantitative predictions in complicated multilayer devices. Materials parameters are usually not exactly determined and a lot of physical mechanisms should be considered, especially in the transport properties of electrons. Moreover, in practice, defects can also play a significant role and process conditions are not always reproducible. In contrast, simulations are based on a model, which lies on fundamental hypotheses. Results are therefore analysed in the framework of this model. If the discrepancy is too large between simulations and experiments, one can still add new ingredients to the model (e.g. Oersted field, stray field, coupling between layers, non-uniformity of the current, thermal

fluctuations, new torques...) and check their influence one by one. The advantage of this procedure is the possibility to eventually know what are the prevailing effects in the device and to validate the model.

Two numerical methods exist to solve the evolution of the magnetisation in time and space: the Finite Difference Method (FDM) and the Finite Element Method (FEM). In the former, the magnetic volume is discretised with a regular grid; in the latter, the elements (usually tetrahedra) vary in size. The FDM is widely used due to its speed and straightforward implementation. Unfortunately, the reliability of this method is guaranteed only when the borders of the sample are parallel to the main axes of the grid. For other geometries, artifacts may appear [6]. This is particularly troublesome for circular and elliptical systems simulated in spintronics. One alternative is the FEM which gives a much better description of the edge of the sample. However, its implementation is tricky and the computation time is generally longer than in FDM.

The choice between fast and accurate simulations is a dilemma that can be solved in two ways: either by changing hardware (parallel computation or GPUs) or by using new numerical methods. This latter option has been chosen by our group that developed a finite element 3D micromagnetic solver. This code, named feeLLGood (Finite Element Equations for LLG with Object-Oriented Development), is the fruit of two previous PhDs achieved by Helga Szambolics [7] and Evaggelos Kritsikis [8] under the supervision of Jean-Christophe Toussaint in the joint simulation team at *Spintec* and *Institut Néel*. In this context, the goal of the PhD work presented in this thesis has been two-fold:

- benchmarking the versions of feeLLGood that include the spin transfer torque;
- studying spin-transfer-driven magnetisation dynamics to understand experimental results obtained by several teams in Spintec (the Spin Torque Oscillator group coordinated by Ursula Ebels and the MRAM group supervised by Bernard Diény.)

In particular, feeLLGood has been benchmarked against ST_GL-FFT, a Finite Difference software previously developed in our group. A first version of feeLLGood (order 1 in time) was available at the beginning of the PhD. Continuous developments have then allowed to test a faster version (order 2 in time) that dramatically decreased the computation time. Meanwhile, a cluster of CPUs was purchased, permitting to run a large number of simulations at the same time. The combination of a fast micromagnetic solver and powerful computers finally led to in-depth analyses of several spintronic devices. On the other hand, feeLLGood results made us aware of some of its strengths and weaknesses, and feedbacks allowed the programming team to improve the code.

The dissertation is organised as follows:

- In *Chapter 1*, theoretical aspects are presented. They are divided in three parts. Firstly, the Landau-Lifshitz-Gilbert (LLG) equation is derived and the different contributions to the effective field are detailed. Micromagnetic and macrospin models, both used during this PhD, are described. Secondly, a short overview of the spin-dependent transport theory is given. The spin torque term obtained is introduced

in the LLG equation to include the spin transfer effect. Finally, the numerical methods used for the simulations are presented, together with a decisive test for any micromagnetic solver: the NIST standard problem No. 4.

The three other chapters are dedicated to applications:

- The *Chapter 2* presents the study of a spin torque oscillator comprising a planar polariser and a planar free layer. The goal is to understand experimental measurements reported in ref. [1], in particular, jumps in frequency. An analysis of simulation data is conducted and spectral mapping techniques are used.

- The *Chapter 3* is dedicated to another type of spin torque oscillator comprising a planar free layer and two fixed ferromagnetic layers: a perpendicular polariser and a planar analyser. feeLLGood results are compared with ST_GL-FFT simulations [9], as well as the macrospin model and experiments [10]. Different oscillation modes are found depending on the initial state. The micromagnetic simulations of this system also showed an artifact in the Finite Difference simulations, induced by the staircase-like edge.

- In the *Chapter 4*, a similar system is simulated applying a current pulse instead of a dc current. Spin-torque-induced precessional switching is then observed. Varying the duration of the pulse and its intensity, the influence of the polariser's stray field is studied to understand the enhanced switching probability measured experimentally [11].

The results obtained confirm that the feeLLGood solver is well adapted to this kind of studies.

Chapter 1

Micromagnetic model

In this chapter, we will introduce the concepts necessary to understand the physics simulated by a micromagnetic solver. After deriving the terms of the Landau-Lifshitz-Gilbert equation, the spin torque term will be introduced. Finally, an overview of the main numerical methods will be given, and feeLLGood, the main software used during this PhD, will be presented.

1.1 Equations of magnetisation motion

1.1.1 From quantum mechanics to classical physics

In quantum mechanics, the spin $\mathbf{S}$ of an electron is associated with its magnetic moment $\boldsymbol{\mu}$ with the relation

$$\boldsymbol{\mu} = -\gamma \mathbf{S}, \tag{1.1}$$

where $\gamma \approx 1.76 \times 10^{11} \mathrm{rad\,s^{-1}T^{-1}}$ is the gyromagnetic ratio of the free electron, expressed as

$$\gamma = \frac{g|e|}{2m_e} > 0. \tag{1.2}$$

g is the Landé splitting factor, $|e|$ is the absolute value of the electron charge, and m_e is the electron mass. $g \approx 2$ for most common ferromagnetic metals. The convention adopted is that of a positive gyromagnetic ratio. The spin operator $\mathbf{S}$ is given by $\mathbf{S} = \frac{\hbar}{2}\boldsymbol{\sigma}$, where $\boldsymbol{\sigma}$ is the Pauli operator $\boldsymbol{\sigma} = \sigma_x \hat{x} + \sigma_y \hat{y} + \sigma_z \hat{z}$ involving the Pauli matrices.

A classical equation of the magnetic moment dynamics can be derived from quantum mechanics principles. The Heisenberg picture provides this link between quantum and classical physics. The time evolution of the observable μ is given by the Heisenberg equation

$$\frac{d}{dt}\langle \boldsymbol{\mu} \rangle = \frac{1}{i\hbar}\langle [\boldsymbol{\mu}, \mathcal{H}] \rangle + \left\langle \frac{\partial \boldsymbol{\mu}}{\partial t} \right\rangle \tag{1.3}$$

where [,] is the commutator, and $\mathcal{H}$ is the Hamiltonian operator. μ does not explicitly depend on time, therefore

$$i\hbar \frac{d}{dt} \langle \boldsymbol{\mu} \rangle = \langle [\boldsymbol{\mu}, \mathcal{H}] \rangle \tag{1.4}$$

This vectorial equation can be written as three scalar equations, each of them corresponding to one spatial coordinate. Using the expression 1.1, the commutator for one coordinate can be expressed as

$$\begin{aligned} [\mu_j, \mathcal{H}] &= -\gamma^2 [S_j, B_x S_x + B_y S_y + B_z S_z] \\ &= -\gamma^2 B_x [S_j, S_x] - \gamma^2 B_y [S_j, S_y] - \gamma^2 B_z [S_j, S_z] \end{aligned} \tag{1.5}$$

where $j = x, y,$ or z.

The components of the angular momentum are connected by the commutation relations

$$[S_x, S_y] = i\hbar S_z \tag{1.6}$$
$$[S_y, S_z] = i\hbar S_x \tag{1.7}$$
$$[S_z, S_x] = i\hbar S_y \tag{1.8}$$

Substituting these expressions in equation 1.5 yields

$$[\mu_x, \mathcal{H}] = i\hbar\gamma^2 \left(B_z S_y - B_y S_z\right) \tag{1.9}$$
$$[\mu_y, \mathcal{H}] = i\hbar\gamma^2 \left(B_x S_z - B_z S_x\right) \tag{1.10}$$
$$[\mu_z, \mathcal{H}] = i\hbar\gamma^2 \left(B_y S_x - B_x S_y\right) \tag{1.11}$$

Therefore, using again the relation 1.1, equation 1.4 becomes

$$\frac{d}{dt} \langle \boldsymbol{\mu} \rangle = -\gamma \langle \boldsymbol{\mu} \rangle \times \mathbf{B} \tag{1.12}$$

The quantum relation 1.4 has been transformed into a classical equation, since $\langle \boldsymbol{\mu} \rangle$ is a measurable physical quantity. Hereafter, $\langle \boldsymbol{\mu} \rangle$ will be denoted $\boldsymbol{\mu}$

Introducing the constant $\gamma_0 = \gamma\mu_0 = 2.21 \times 10^5$ m A^{-1} s^{-1}, and replacing $\mathbf{B}$ with the magnetic field $\mathbf{H}$ leads to

$$\frac{d\boldsymbol{\mu}}{dt} = -\gamma_0 \left(\boldsymbol{\mu} \times \mathbf{H}\right) \tag{1.13}$$

This equation describes the precessional motion of a single magnetic moment under the action of a field $\mathbf{H}$. Multiplying both sides by $\boldsymbol{\mu}$ leads to the fundamental property of the conservation of the norm

$$\frac{d}{dt} \left(\frac{1}{2} \boldsymbol{\mu}^2\right) = 0 \tag{1.14}$$

Moreover, assuming a constant field and multiplying equation 1.13 by $\mathbf{H}$ yields

$$\frac{d\left(\boldsymbol{\mu}\cdot\mathbf{H}\right)}{dt}=0 \tag{1.15}$$

meaning that the angle between $\boldsymbol{\mu}$ and $\mathbf{H}$ is constant. The magnetic moment is thus precessing about the field $\mathbf{H}$ at a constant angle with a frequency

$$f=\frac{\gamma_0 H}{2\pi} \tag{1.16}$$

called "Larmor frequency". The precessional motion is illustrated on figure 1.1.

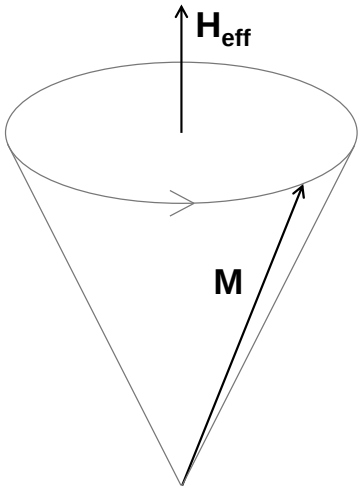

Figure 1.1: Undamped precession of a magnetic moment about the field $\mathbf{H_{eff}}$.

So far, only the intrinsic spin of the electro has been taken into account to calculate the magnetic moment, but the orbital moment $\boldsymbol{\ell}$ has to considered as well. Eventually, the magnetic moment $\boldsymbol{\mu}$ includes both contributions:

$$\boldsymbol{\mu}=-\frac{|e|}{2m_e}(\boldsymbol{\ell}+2\boldsymbol{S}) \tag{1.17}$$

The derived equation of motion is local, since it was derived for one single magnetic moment. However, considering an elementary volume δV containing several moments $\boldsymbol{\mu_i}$, and assuming a constant field within this volume, one can take the volume average of equation 1.13

$$\frac{1}{\delta V}\frac{\sum_i \boldsymbol{\mu_i}}{dt}=-\gamma_0\left(\frac{\sum_i \boldsymbol{\mu_i}}{\delta V}\times\mathbf{H}\right) \tag{1.18}$$

Defining the magnetisation vector field $\mathbf{M}$ as

$$\mathbf{M}=\frac{\sum_i \boldsymbol{\mu_i}}{\delta V} \tag{1.19}$$

the microscopic equation 1.13 can be rewritten as

$$\frac{\partial \mathbf{M}}{\partial t} = -\gamma_0 \left(\mathbf{M} \times \mathbf{H_{eff}}\right) \tag{1.20}$$

providing now a description at mesoscopic scale, suitable for study of ferromagnetic materials. This description lies on the continuum hypothesis, a fundamental hypothesis of the micromagnetic theory (see section 1.1.5). $\mathbf{M}$ and $\mathbf{H_{eff}}$ depend on time and space. $\mathbf{H_{eff}}$ is the local effective field experienced by the magnetisation inside the material. It is a sum of several contributions, as explained later, in section 1.1.3.

1.1.2 Energy dissipation

Introducing the damping

Equation 1.20 is conservative, since the magnetisation precesses endlessly keeping the same angle and the same energy. However, in real ferromagnetic materials, dissipation processes cause the system to minimise its energy. The energy minimum is reached when $\frac{\partial}{\partial t} = 0$, which is equivalent to $\mathbf{M} \times \mathbf{H_{eff}} = 0$, according to equation 1.20. Therefore, at equilibrium, the magnetisation is aligned with the effective field. In order to take account of dissipation, a term has to be added to equation 1.20, allowing the magnetisation to reach static equilibrium. In 1955, Gilbert [12] suggested to introduce the damping as a viscous force proportional to the time derivative of the magnetisation. The additional contribution

$$-\frac{\alpha}{\gamma_0 M_s}\frac{\partial \mathbf{M}}{\partial t} \tag{1.21}$$

is added to the effective field $\mathbf{H_{eff}}$. This term can be derived assuming a Rayleigh dissipation functional [13]. The constant M_s is the spontaneous magnetisation that will be defined in the next section. α is a dimensionless phenomenological constant, arising from all the dissipation processes, such as magnon-magnon scattering, magnon-phonon scattering, eddy currents... The meaning and the measurement of α is an intricate matter, since its value depends not only on the material, but also on experimental conditions. For the sake of simplicity, α will always be considered as a scalar constant hereafter. For most common ferromagnetic materials, $\alpha \sim 10^{-2}$.

The so-called Gilbert equation, including both the precessional and the damping term, reads

$$\boxed{\frac{\partial \mathbf{M}}{\partial t} = -\gamma_0 \left(\mathbf{M} \times \mathbf{H_{eff}}\right) + \frac{\alpha}{M_s}\left(\mathbf{M} \times \frac{\partial \mathbf{M}}{\partial t}\right)} \tag{1.22}$$

This equation is equivalent to the one introduced by Landau and Lifshitz [14]. Indeed, multiplying the Gilbert equation 1.22 by $\mathbf{M}$, then using the vector triple product formula and the identity $\mathbf{M} \cdot \frac{\partial \mathbf{M}}{\partial t} = 0$, one can show that

$$\mathbf{M} \times \frac{\partial \mathbf{M}}{\partial t} = -\gamma_0 \left[\mathbf{M} \times \left(\mathbf{M} \times \mathbf{H_{eff}}\right)\right] - \alpha M_s \frac{\partial \mathbf{M}}{\partial t}. \tag{1.23}$$

Substituting this expression in equation 1.22 leads to the Landau-Lifshitz equation

$$\boxed{\frac{\partial \mathbf{M}}{\partial t} = -\gamma_L \left(\mathbf{M} \times \mathbf{H_{eff}}\right) - \frac{\lambda}{M_s}\left[\mathbf{M} \times \left(\mathbf{M} \times \mathbf{H_{eff}}\right)\right]} \tag{1.24}$$

where the gyromagnetic ratio γ_L is

$$\gamma_L = \frac{\gamma_0}{(1+\alpha^2)} \tag{1.25}$$

and the damping constant λ is

$$\lambda = \frac{\gamma_0 \alpha}{(1+\alpha^2)}. \tag{1.26}$$

Usually $\alpha \ll 1$, therefore $\gamma_L \approx \gamma_0$ and $\lambda \approx \gamma_0 \alpha$. The Landau-Lifshitz equation 1.24 is of great interest for numerical resolution since the time derivative of $\mathbf{M}$ is directly expressed as function of $\mathbf{M}$ and $\mathbf{H_{eff}}$. Mallinson [15] pointed out the difference in the physical meaning of both equations. The precessional term of equations 1.22 and 1.24 are equivalent only in the limit of very low α value. For a very large damping constant, the dynamics are different since

$$[\text{Gilbert equation 1.22}] \Rightarrow \frac{\partial \mathbf{M}}{\partial t} \xrightarrow[\alpha \to \infty]{} 0 \tag{1.27}$$

$$[\text{Landau-Lifshitz equation 1.24}] \Rightarrow \frac{\partial \mathbf{M}}{\partial t} \xrightarrow[\lambda \to \infty]{} \infty \tag{1.28}$$

One would expect the magnetisation to move slower when the damping constant goes to infinity (a limit with no physical meaning). In this sense, the Gilbert equation is more intuitive than the Landau-Lifshitz form. The Gilbert damping α is therefore more appropriate for study of magnetisation dynamics. In this thesis "the damping constant" will always refer to α.

Comments on the conservation of the norm

One can notice that both equations 1.22 and 1.24 are norm conservative, like their undamped counterpart (see equation 1.14). At any point $\mathbf{r}$ in the ferromagnet,

$$\frac{d}{dt}\left(|\mathbf{M}|^2\right) = 0. \tag{1.29}$$

Therefore,

$$|\mathbf{M}(\mathbf{r}, t)| = |\mathbf{M}(\mathbf{r}, t_0)| = M_s \tag{1.30}$$

Inside a sample made of one material, M_s is assumed to be spatially constant. M_s is called *spontaneous magnetisation* or sometimes *saturation magnetisation*. $M_s V$ is the maximum magnetic moment of a ferromagnetic sample, obtained when all the magnetic

moments are aligned. For convenience, a normalised magnetisation

$$\mathbf{m}(\mathbf{r},t) = \frac{\mathbf{M}(\mathbf{r},t)}{M_s} \tag{1.31}$$

is defined. Thus, the amplitude of $\mathbf{m}(\mathbf{r},t)$ is equal to 1. It follows that the magnetisation motion at a given point of the sample can be described by a trajectory on the unit sphere. The magnetisation is then given by only two components: θ and φ, in the spherical coordinate system. In Cartesian coordinates, the third component can be deduced from the conservation of the norm $m_x^2 + m_y^2 + m_z^2 = 1$.

The normalised Gilbert equation reads

$$\boxed{\frac{\partial \mathbf{m}}{\partial t} = -\gamma_0 \left(\mathbf{m} \times \mathbf{H_{eff}}\right) + \alpha \left(\mathbf{m} \times \frac{\partial \mathbf{m}}{\partial t}\right)} \tag{1.32}$$

hereafter referred to as the Landau-Lifshitz-Gilbert equation (LLG equation).

Energy dissipation rate

The effective field is proportional to the variational derivative of the energy density ϵ_{tot}.

$$\mathbf{H_{eff}} = -\frac{1}{\mu_0 M_s}\frac{\delta \epsilon_{tot}}{\delta \mathbf{m}} \tag{1.33}$$

The total energy E_{tot} of the system is simply the integral of ϵ_{tot} over the whole magnetic volume Ω. If the energy density does not explicitly depend on time (which is generally true if the applied field is constant), then

$$\frac{dE_{tot}}{dt} = \int_\Omega \frac{\delta \epsilon_{tot}}{\delta \mathbf{m}} \cdot \frac{\partial \mathbf{m}}{\partial t} d\mathbf{r} \tag{1.34}$$

$$= -\mu_0 M_s \int_\Omega \mathbf{H_{eff}} \cdot \frac{\partial \mathbf{m}}{\partial t} d\mathbf{r} \tag{1.35}$$

The scalar product of equation 1.32 with $\mathbf{H_{eff}}$ leads to

$$\mathbf{H_{eff}} \cdot \frac{\partial \mathbf{m}}{\partial t} = -\alpha \frac{\partial \mathbf{m}}{\partial t} \cdot (\mathbf{m} \times \mathbf{H_{eff}}) \tag{1.36}$$

while the scalar product with $\partial \mathbf{m}/\partial t$ yields

$$\frac{\partial \mathbf{m}}{\partial t} \cdot (\mathbf{m} \times \mathbf{H_{eff}}) = -\frac{1}{\gamma_0}\left(\frac{\partial \mathbf{m}}{\partial t}\right)^2. \tag{1.37}$$

Combining these two relations and substituting the result in the LLG equation 1.32 leads

to the following expression of the energy dissipation rate

$$\boxed{\frac{dE_{tot}}{dt} = -\frac{\alpha\mu_0 M_s}{\gamma_0}\int_\Omega \left(\frac{\partial \mathbf{m}}{\partial t}\right)^2 d\mathbf{r}} \tag{1.38}$$

The rate at which the system loses its energy is therefore proportional to the damping constant α. In the particular case of $\alpha = 0$, the energy is conserved. Equation 1.38 holds at relaxation, when the external field is constant. Therefore, it does not apply to the case of a magnetisation driven by a field pulse, for example. Moreover, it is assumed that no energy is injected into the system. It means that this equation is wrong when the magnetisation experiences spin transfer torque, as it will be shown later on.

The energy dissipation is faster when α is large, therefore numerical simulations seeking the equilibrium state are usually performed at $\alpha = 1$ (or sometimes $\alpha = 0.5$). Starting from a given state, the magnetisation relaxes until the system reaches its closest energy minimum.

1.1.3 Effective magnetic field

The effective magnetic field involved in the Landau-Lifshitz-Gilbert equation is the sum of several contributions which have different physical origins. The most common magnetic fields included in the effective field are: the exchange field, the demagnetising field, the magnetocrystalline anisotropy field, the applied field, the magnetoelastic field, the thermal field and the Oersted field.

$$\mathbf{H_{eff}} = \mathbf{H_{ex}} + \mathbf{H_d} + \mathbf{H_{anis}} + \mathbf{H_{app}} + \mathbf{H_{elas}} + \mathbf{H_{th}} + \mathbf{H_{Oe}} \tag{1.39}$$

Solving the Landau-Lifshitz-Gilbert equation necessitates the evaluation of all these fields. It is worth noting the definition of $\mathbf{H_{eff}}$ is not unique. Indeed, in the LLG equation, $\mathbf{H_{eff}}$ is involved in a cross product with $\mathbf{m}$. Therefore, a vector proportional to $\mathbf{m}$ can be added to $\mathbf{H_{eff}}$, likewise for each contribution.

Similarly, the total energy, also called *Gibbs free energy*, is

$$E_{tot} = E_{ex} + E_d + E_{anis} + E_Z + E_{elas} + E_{th} + E_{Oe}. \tag{1.40}$$

In this section, we will give the expressions of all the fields, as well as their corresponding energies.

Exchange interaction

The exchange interaction is a short-range interaction coupling two neighbouring spins. It arises from the quantum mechanics principle of exchange symmetry stating that no observable physical quantity should change after exchanging two indistinguishable particles.

The Hamiltonian of the exchange interaction can be written as

$$\mathcal{H}_{ex} = -2 \sum_{\{i,j\}} J_{ij} \mathbf{S_i} \cdot \mathbf{S_j}, \tag{1.41}$$

where $J_{i,j}$ is the Heisenberg exchange integral. Since it is a short-range interaction, one can consider the sum being over the nearest neighbours only. The sign of J_{ij} determines whether the material is ferromagnetic (parallel alignment) or antiferromagnetic (anti-parallel alignment). Assuming a constant amplitude of the spins $|\mathbf{S_i}| = |\mathbf{S_j}| = S$, and a small misalignment between neighbouring spins, the scalar product $\mathbf{S_i} \cdot \mathbf{S_j}$ can be expressed as

$$\mathbf{S_i} \cdot \mathbf{S_j} = S^2 \left[1 - \frac{1}{2} \left[\Delta \mathbf{r_i} \cdot \nabla \mathbf{m}(\mathbf{r_i}) \right]^2 \right], \tag{1.42}$$

where $\Delta \mathbf{r_i}$ is the distance between the two neighbouring spins. Going from the microscopic equation 1.41 to a mesoscopic description is thus achieved by replacing the lattice of isolated spins with a magnetisation function continuously varying in space. Considering an isotropic exchange interaction ($J_{ij} = J$) and substituting equation 1.42 in 1.41, the following Hamiltonian is deduced:

$$\begin{aligned} \mathcal{H}_{ex} &= -2JS^2 + JS^2 \sum_i \left[\Delta \mathbf{r_i} \cdot \nabla \mathbf{m}(\mathbf{r_i}) \right]^2 \\ &= \text{Cst.} + JS^2 \sum_i \left[\left[\Delta \mathbf{r_i} \cdot \nabla m_x(\mathbf{r_i}) \right]^2 + \left[\Delta \mathbf{r_i} \cdot \nabla m_y(\mathbf{r_i}) \right]^2 + \left[\Delta \mathbf{r_i} \cdot \nabla m_z(\mathbf{r_i}) \right]^2 \right] \end{aligned} \tag{1.43}$$

Dropping the additive constant and summing over all the spins leads to the expression of the exchange energy

$$E_{ex} = \int_\Omega A_{ex} \left[\left(\nabla m_x(\mathbf{r}) \right)^2 + \left(\nabla m_y(\mathbf{r}) \right)^2 + \left(\nabla m_z(\mathbf{r}) \right)^2 \right] d\mathbf{r} \tag{1.44}$$

where A_{ex} is the exchange stiffness constant, having the dimension of an energy per unit length. Typical values of A_{ex} are in the order of 10^{-11}J/m. In the case of a simple cubic lattice, with lattice parameter a,

$$A_{ex} = \frac{JS^2}{a}. \tag{1.45}$$

The exchange field is derived similarly to the effective field (equation 1.33):

$$\mathbf{H_{ex}} = -\frac{2A_{ex}}{\mu_0 M_s} \Delta \mathbf{m}. \tag{1.46}$$

$\mathbf{H_{ex}}$ is therefore a local field: calculating it at a given point necessitates only the second-order spatial derivatives of $\mathbf{m}$ at this point.

The reason why the *effective field* is called such is now clear: it includes the exchange field which is not a "real" magnetic field, but rather accounts for a quantum mechanical effect.

Dipolar interaction

A ferromagnetic material contains several magnetic domains pointing in different directions. The exchange interaction explains the alignment of the magnetic moments inside a domain, but it does not allow to understand why domain walls are formed. In fact, a long-range interaction, called magnetostatic interaction accounts for the domain structure. Each magnetic moment in the ferromagnet is a dipole that produces a field experienced by other magnetic moments. Thus, a pair of dipole driven only by the magnetostatic interaction will point parallel along the line passing through their positions.

Exchange and dipolar interactions are in competition, the former aligning the moments in the same direction, and the latter creating opposite domains over long distances. It follows that the typical size of the domains results from the relative strengths of these two interactions. Unlike the exchange interaction which is local, the dipolar field at a given point is a sum over the contributions of all the magnetic moments in the whole magnetic volume. Subsequently, the numerical computation of this field is much more time-consuming than other fields.

Various names are given to the dipolar field. For the sake of clarity, it will be called *stray field* outside the material and *demagnetising field* inside. The demagnetising field is opposed to the magnetisation, hence its name.

The expression of the demagnetising field $\mathbf{H_d}$ can be derived from three fundamental equations: the relationship between $\mathbf{H}$ and $\mathbf{M}$, given by

$$\mathbf{B} = \mu_0(\mathbf{H} + \mathbf{M}), \tag{1.47}$$

and the following two Maxwell's equations (in absence of electrical current)

$$\nabla \cdot \mathbf{B} = 0 \tag{1.48}$$

$$\nabla \times \mathbf{H_d} = 0. \tag{1.49}$$

Equations 1.47 and 1.48 imply

$$\nabla \cdot \mathbf{H} = -\nabla \cdot \mathbf{M} \tag{1.50}$$

In this equation, $\mathbf{H}$ is the total field. In fact, the divergence of all the fields apart from $\mathbf{H_d}$ is zero, such that one can write

$$\nabla \cdot \mathbf{H_d} = -\nabla \cdot \mathbf{M} \tag{1.51}$$

According to 1.49, the dipolar field is irrotational, which means that $\mathbf{H_d}$ is a conservative vector field. Therefore, there exists a scalar potential ϕ such that

$$\mathbf{H_d} = -\nabla\phi \tag{1.52}$$

Combining equations 1.51 and 1.52 yields

$$\Delta\phi = \nabla \cdot \mathbf{M} \tag{1.53}$$

By analogy with electrostatics, the volume charge density is expressed as

$$\rho_m = -\nabla \cdot \mathbf{M}, \tag{1.54}$$

such that the problem of solving the demagnetising field inside the magnetic volume reduces to the Poisson equation

$$\boxed{\Delta\phi_{in} = -\rho_m}. \tag{1.55}$$

Outside the magnetic volume, $\mathbf{M} = \mathbf{0}$, hence the Laplacian equation

$$\boxed{\Delta\phi_{out} = 0}. \tag{1.56}$$

The previous equations were derived inside or outside the magnetic body Ω. However, the boundary $\partial\Omega$ induces a discontinuity of the dipolar field that has to be treated. The following conditions apply at the surface $\partial\Omega$:

$$\mathbf{n} \cdot \left(\mathbf{H_d^{out}} - \mathbf{H_d^{in}}\right) = \mathbf{n} \cdot \mathbf{M} \tag{1.57}$$

$$\mathbf{n} \times \left(\mathbf{H_d^{out}} - \mathbf{H_d^{in}}\right) = 0 \tag{1.58}$$

The above equations state that the component of the dipolar field normal to the surface is discontinuous, whereas its tangential component is continuous. This is expressed in terms of magnetic potential by the condition

$$\boxed{\left.\frac{\partial\phi_{out}}{\partial\mathbf{n}}\right|_{\partial\Omega} - \left.\frac{\partial\phi_{in}}{\partial\mathbf{n}}\right|_{\partial\Omega} = -\sigma_m}, \tag{1.59}$$

where

$$\sigma_m = \mathbf{M} \cdot \mathbf{n} \tag{1.60}$$

is the surface charge density. Moreover, the magnetic potential is chosen to be continuous at the boundary, and to vanish at infinity.

The problem posed by equations 1.55, 1.56, 1.59 is solved by the Green's method. The magnetic potential reads

$$\phi(\mathbf{r}) = \frac{1}{4\pi}\int_\Omega \frac{\rho_m(\mathbf{r}')}{|\mathbf{r}-\mathbf{r}'|}d\mathbf{r}' + \frac{1}{4\pi}\int_{\partial\Omega} \frac{\sigma_m(\mathbf{r}')}{|\mathbf{r}-\mathbf{r}'|}d\mathbf{r}'. \tag{1.61}$$

Denoting G the Green's function

$$G(\mathbf{r}-\mathbf{r}') = \frac{1}{4\pi|\mathbf{r}-\mathbf{r}'|}, \tag{1.62}$$

the dipolar field is then calculated by applying the gradient operator to ϕ:

$$\mathbf{H_d}(\mathbf{r}) = -\int_\Omega \nabla G(\mathbf{r}-\mathbf{r}')\rho_m(\mathbf{r}')d\mathbf{r}' - \int_{\partial\Omega} \nabla G(\mathbf{r}-\mathbf{r}')\sigma_m(\mathbf{r}')d\mathbf{r}' \tag{1.63}$$

$$= -\left[\nabla G * \rho_m\right](\mathbf{r}) - \left[\nabla G * \sigma_m\right](\mathbf{r}), \tag{1.64}$$

where $*$ is the convolution product.

This latter expression of $\mathbf{H_d}$ is very convenient, especially in the Finite Difference Method (see section 1.3.1): ∇G is computed once at the beginning of the simulation, and only the magnetic charges need to be updated after each time step. More details about the demagnetising field computation will be given in section 1.3.

The mutual energy of a pair of dipoles is given by a reciprocity theorem stating that

$$\begin{aligned} E_{ij} &= -\mu_0(\boldsymbol{\mu_i}\cdot\mathbf{H_j}(\mathbf{r_i})) \\ &= -\mu_0(\boldsymbol{\mu_j}\cdot\mathbf{H_i}(\mathbf{r_j})) \\ &= -\frac{1}{2}\mu_0(\boldsymbol{\mu_i}\cdot\mathbf{H_j}(\mathbf{r_i}) + \boldsymbol{\mu_j}\cdot\mathbf{H_i}(\mathbf{r_j})) \end{aligned} \tag{1.65}$$

where $\mathbf{H_j}(\mathbf{r_i})$ is the field produced by the dipole j at the location of dipole i. Therefore, the total magnetostatic energy inside the magnetic volume is

$$E_d = -\frac{1}{2}\mu_0 \sum_{i=1}^{N}\sum_{j=1}^{N} \boldsymbol{\mu_j}\cdot\mathbf{H_i}(\mathbf{r_j}) \tag{1.66}$$

where N is the total number of elementary dipoles. Going from the discrete to the continuous description yields

$$E_d = -\frac{1}{2}\mu_0 M_s \int_\Omega \mathbf{m}(\mathbf{r})\cdot\mathbf{H_d}(\mathbf{r})d\mathbf{r} \tag{1.67}$$

The system minimises its energy by minimising the magnetic charges, following the pole-avoidance principle [16]. This is equivalent, for the demagnetising field to follow closed paths, as illustrated on figure 1.2. The formation of domains leads to a reduced magnetostatic energy, and also to an increased exchange energy.

Since surface magnetostatic charges are located at the boundaries, the magnetisation tends to align along the edge. Thus, in the single-domain approximation (see section 1.1.6), the magnetisation is preferentially pointing in the longest dimension of the sample. The so-called *shape anisotropy* is therefore ascribed to the magnetostatic interaction.

Magnetocrystalline anisotropy

In crystalline materials, magnetisation tends to be aligned along certain symmetry directions, referred to as *easy axes*. Magnetocrystalline anisotropy arises mostly from spin-orbit interaction. Uniaxial anisotropy is the most common situation, corresponding to the existence of one only anisotropy axis. The uniaxial anisotropy energy is rotationally-

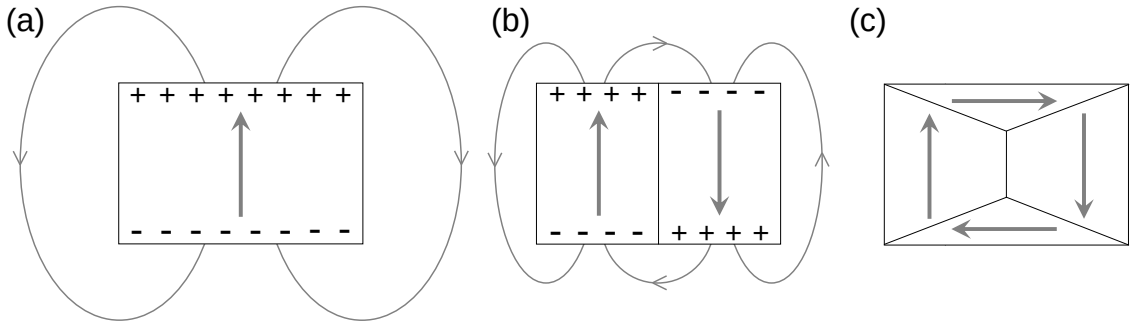

Figure 1.2: Dipolar field generated by a ferromagnetic sample. (a) Single-domain configuration. (b) Two-domain configuration. (c) Flux-closure domains. The total dipolar energy is decreased when going from (a) to (c) thanks to the formation of domains. Surface magnetic charges exist in configurations (a) and (b) but disappear in (c). The counterpart is the formation of volume magnetic charges at the domain walls.

symmetric with respect to this axis and depends only on the relative angle θ between the anisotropy axis and the magnetisation. The general form of the uniaxial anisotropy energy can be written as an even function of $\sin^2\theta$

$$\frac{E_{anis}}{V} = K_0 + K_1 \sin^2\theta + K_2 \sin^4\theta + K_3 \sin^6\theta + ... \tag{1.68}$$

where V is the volume, and K are the anisotropy constants, which have the dimension of energy per unit volume. Usually, this Taylor expansion is truncated after the $\sin^2\theta$ term. If $K_1 > 0$, then E_{anis} is minimum when the magnetisation lies along the anisotropy axis, which is therefore an *easy axis*. If $K_1 < 0$, then E_{anis} is maximum if the magnetisation is aligned with the anisotropy axis and it is minimum if it is perpendicular to this axis. There is then an *easy plane*. In this thesis, we will not deal with the case of easy plane, therefore we will always refer to uniaxial anisotropy when it is connected with the existence of an easy axis.

Since an energy is defined up to an additive constant, K_0 can be chosen arbitrarily. It is set to zero, such that the energy minimum is zero. $K_1 \sin^2\theta$ can be rewritten as $1 - (\mathbf{u_K} \cdot \mathbf{m})^2$. The uniaxial anistropy energy reads

$$E_{anis} = \int_\Omega K_u \left[1 - (\mathbf{u_K} \cdot \mathbf{m}(\mathbf{r}))^2\right] d\mathbf{r} \tag{1.69}$$

where $K_u = K_1$. Using an expression similar to equation 1.33, the anisotropy field $\mathbf{H_{anis}}$ is derived, leading to

$$\mathbf{H_{anis}} = \frac{2K_u}{\mu_0 M_s}(\mathbf{u_K} \cdot \mathbf{m})\mathbf{u_K} \tag{1.70}$$

where $\mathbf{u_K}$ is the unit vector aligned along the easy axis.

It is to note that another anisotropy term, the Néel surface anisotropy, arising from interface interactions, can have a major influence in thin films. An effective anisotropy

constant K_{eff} is then expressed as the sum of the bulk and surface anisotropies:

$$K_{eff} = K_u + 2K_s/t. \tag{1.71}$$

K_s is the Néel surface anisotropy constant, and t is the layer thickness. This equation holds in the case when both top and bottom layers have the same surface anisotropy (hence the factor 2) and the magnetocrystalline anisotropy axis $\mathbf{u_K}$ is out-of-plane.

More details about surface and interface effects will be given in section 1.1.4.

Zeeman

When an external field $\mathbf{H_{app}}$ is applied, it creates a torque $\mathcal{T} = -\mu_0 \mathbf{m} \times \mathbf{H_{app}}$. This "force" gives rise to a potential energy called *Zeeman energy*, given by

$$E_Z = -\mu_0 \int_\Omega M_s \left[\mathbf{m}(\mathbf{r}) \cdot \mathbf{H_{app}}(\mathbf{r})\right] d\mathbf{r} \tag{1.72}$$

In the case of a uniform applied field, the Zeeman energy can vary between $-\mu_0 M_s V H_{app}$ (uniform magnetisation aligned with $\mathbf{H_{app}}$) and $+\mu_0 M_s V H_{app}$ (uniform magnetisation opposite to $\mathbf{H_{app}}$).

Magnetoelastic energy

Magnetoelastic interaction accounts for magnetostriction as well as its inverse effect, called *Villari effect*. The magnetostriction is the property of a ferromagnetic material to change its dimensions when an external field is applied. The inverse magnetostrictive effect is the generation of a magnetic field when the sample is subjected to a mechanical stress. The expression of the strain field is

$$\mathbf{H_{elas}} = \frac{3\lambda_s \sigma}{\mu_0 M_s} \left(\mathbf{m} \cdot \mathbf{u_\sigma}\right) \mathbf{u_\sigma}, \tag{1.73}$$

where λ_s is the magnetostrictive expansion at saturation, σ is the stress and $\mathbf{u_\sigma}$ is the direction of the applied stress. The strain field acts as the anisotropy field, except that its direction is given by the stress instead of the easy axis.

The corresponding magnetoelastic energy reads

$$\mathbf{E_{elas}} = -\int_\Omega \frac{3\lambda_s \sigma}{2} \left(\mathbf{m} \cdot \mathbf{u_\sigma}\right)^2 d\mathbf{r}. \tag{1.74}$$

The definition of the magnetoelastic field and energy is given for the sake of completeness. Indeed, in this thesis, the magnetoelastic interaction will always be neglected. Moreover, it is worth noting that permalloy $Ni_{81}Fe_{19}$ (one of the most common materials in spintronics) has a near zero magnetostriction [17], which is a useful property for RF devices, such as spin-torque oscillators (see chapters 2 and 3).

Thermal random field

According to Brown [16], thermal fluctuations can be modelled by a random magnetic field if the temperature is much less than than the Curie temperature (limit between the ferromagnetic and the paramagnetic state). The mean value of the thermal field is zero

$$\langle \mathbf{H_{th}}(\mathbf{r_i}, t_k) \rangle = 0 \tag{1.75}$$

and its auto-correlation function is given by

$$\langle \mathbf{H_{th}}(\mathbf{r_1}, t_1) \cdot \mathbf{H_{th}}(\mathbf{r_2}, t_2) \rangle = D\delta(\mathbf{r_1} - \mathbf{r_2})\delta(t_1 - t_2), \tag{1.76}$$

where D is the variance expressed as

$$D = \frac{2\alpha k_B T}{\mu_0 M_s V \gamma_0}. \tag{1.77}$$

Consequently, the field has a Gaussian distribution centred about zero with a variance proportional to the temperature and to the damping factor α, and inversely proportional to the magnetic volume V. In the single-domain approximation, V is the total magnetic volume, whereas in finite-difference micromagnetics (see section 1.3.1) V is the volume of mesh cell.

Since $\mathbf{H_{th}}$ is a random field, it accounts for non-deterministic processes. Therefore, running several times the same simulation at finite temperature will lead to a distribution of magnetisation trajectories. The larger the temperature, the broader the distribution. In contrast, a simulation in absence of the random field $\mathbf{H_{th}}$ is deterministic, which means that running several times the same simulation will always give exactly the same result.

Oersted field

The Oersted field, also called *Ampère's field*, is the magnetic field generated by a current of charge, following thus the Maxwell's equation

$$\nabla \times \mathbf{H_{Oe}} = \mathbf{j}. \tag{1.78}$$

Integrating over a contour $\mathcal{C}$ yields the Ampère's circuital law

$$\oint_{\mathcal{C}} \mathbf{H_{Oe}} \cdot d\boldsymbol{\ell} = I_{enclosed}, \tag{1.79}$$

where $I_{enclosed}$ is the current passing through the loop $\mathcal{C}$. In the very particular case of an infinite cylinder of circular cross-section traversed by a rotationally-symmetric current distribution (e.g. uniform current), the Oersted field is directed along $\mathbf{u_\theta}$. Then, choosing a circular contour $\mathcal{C}$ centred about the cylinder axis, the equation 1.79 becomes

$$H_{Oe} = \frac{I_{enclosed}}{2\pi r}, \tag{1.80}$$

where r is the radius of $\mathcal{C}$. If r is greater than the cylinder radius R, then the Oersted field decreases with $1/r$. Assuming a uniform current density j_0 inside the cylinder, $I_{enclosed} = j_0 \pi r^2$, and therefore $H_{Oe} = j_0 r/2$ when $r < R$. Subsequently, the Oersted field is maximum at the edge of the cylinder; it is equal to $j_0 R/2$. Therefore, the maximum intensity of the Oersted field inside a nanopillar depends on its lateral size.

1.1.4 Boundary conditions and interface effects

In the most general case, the boundary condition [18, 19] can be expressed as

$$\mathbf{m} \times \left[\frac{\partial \epsilon_s}{\partial \mathbf{m}} + \frac{\partial \epsilon}{\partial (\nabla \mathbf{m})} \mathbf{n} \right] = \mathbf{0} \tag{1.81}$$

where ϵ_s is the surface energy density (in J/m^2) and ϵ is the volume energy density (in J/m^3). The term $\frac{\partial \epsilon}{\partial (\nabla \mathbf{m})}$ is a matrix.

In the case when there is no surface interaction ($\epsilon_s = 0$), the equation 1.81 reduces to

$$\mathbf{m} \times \left[\frac{\partial \epsilon}{\partial (\nabla \mathbf{m})} \mathbf{n} \right] = \mathbf{0} \tag{1.82}$$

Only the exchange energy depends on the magnetisation gradient. Therefore, in absence of surface interaction, the boundary conditions arise solely from the symmetry breaking of the exchange interaction at the surface, yielding the so-called *free boundary conditions*:

$$\mathbf{m} \times \left[2A_{ex} \left(\mathbf{n} \cdot \nabla \right) \mathbf{m} \right] = \mathbf{0}, \tag{1.83}$$

implying the *Brown's condition*

$$\frac{\partial \mathbf{m}}{\partial \mathbf{n}} = \mathbf{0}, \tag{1.84}$$

which is a Neumann boundary condition. It ought to be mentioned that $\frac{\partial \mathbf{m}}{\partial \mathbf{n}}$ denotes the spatial derivative of $\mathbf{m}$ along the normal to the boundary, that is

$$\frac{\partial \mathbf{m}}{\partial \mathbf{n}} = \nabla \mathbf{m} \cdot \mathbf{n} = \left(\nabla m_x \cdot \mathbf{n} \right) \mathbf{u_x} + \left(\nabla m_y \cdot \mathbf{n} \right) \mathbf{u_y} + \left(\nabla m_z \cdot \mathbf{n} \right) \mathbf{u_z} \tag{1.85}$$

In 1953, Néel introduced [20, 21] a surface anisotropy with a corresponding energy density

$$\epsilon_{s,Néel} = K_s \left[1 - \left(\mathbf{m} \cdot \mathbf{n} \right)^2 \right], \tag{1.86}$$

where the surface anisotropy coefficient K_s is an energy per unit area, with typical values of about $10^{-3} - 10^{-4}$ J/m^2. A positive K_s constant leads to a magnetisation preferentially aligned perpendicular to the surface.

When a ferromagnetic layer is in contact with another one or with an antiferromagnet, an exchange interaction couples both layers at the interface. In the general case [22, 23], this interlayer exchange coupling can be phenomenologically modelled by the surface

energy density

$$\epsilon_{s,interlayer} = J_1[1 - \mathbf{m}\cdot\mathbf{m}'] + J_2\left[1 - (\mathbf{m}\cdot\mathbf{m}')^2\right], \tag{1.87}$$

where J_1 is the bilinear coefficient and J_2 is the biquadratic coefficient. $J_1 > 0$ favours a parallel orientation (ferromagnetic coupling) and $J_1 < 0$ tends to align the layers antiparallel (antiferromagnetic coupling).

From the two surface energy terms (eq. 1.86 and 1.87), it follows that the derivative of the total surface energy density with respect to $\mathbf{m}$ is

$$\frac{\partial \epsilon_s}{\partial \mathbf{m}} = -2K_s\left(\mathbf{m}\cdot\mathbf{n}\right)\mathbf{n} - J_1\mathbf{m}' - 2J_2\left(\mathbf{m}\cdot\mathbf{m}'\right)\mathbf{m}' \tag{1.88}$$

Substituting the latter expression in equation 1.81, and applying a cross-product with $\mathbf{m}$ leads to the boundary condition

$$A\frac{\partial \mathbf{m}}{\partial \mathbf{n}} = K_s(\mathbf{n}\cdot\mathbf{m})[\mathbf{n} - (\mathbf{n}\cdot\mathbf{m})\mathbf{m}] + \frac{1}{2}[J_1 + 2J_2\mathbf{m}'\cdot\mathbf{m}][\mathbf{m}' - (\mathbf{m}'\cdot\mathbf{m})\mathbf{m}] \tag{1.89}$$

Historically, boundary conditions in presence of surface anisotropy were first derived by Rado and Weertman [18].

A more convenient expression of the boundary conditions is often adopted for the study of spin waves in thin bounded ferromagnets [24, 25, 26, 27]. Considering a small oscillation angle θ about the out-of-plane axis z, the following boundary conditions were derived by Soohoo [28]:

$$\frac{\partial m_x}{\partial n} + d\cos(2\theta)\ m_x = 0 \qquad\qquad \frac{\partial m_y}{\partial n} + d\cos^2(\theta)\ m_y = 0, \tag{1.90}$$

where d is the pinning parameter. The absence of pinning ($d = 0$) results in the condition of *free magnetic moments* expressed by the Brown's equation 1.84. In the other limiting case of $d \to \infty$, a *perfect pinning* is found, expressed by the condition of a fixed $\mathbf{m}$. This condition was first proposed by Kittel [29].

Non-uniformity of the demagnetising field near the edge can also be taken into account in the boundary conditions, as shown in references [26, 27].

1.1.5 Assumptions of the micromagnetic theory

Following the derivation of the Landau-Lifshitz-Gilbert equation and the various fields, it turns out that several assumptions have been made. The two main assumptions supporting the micromagnetic theory are the following:

- The magnetisation is supposed to vary slowly and continuously in space, in particular there is a small misalignment at the scale of the lattice constant.

- The norm of the magnetisation is constant ($|\mathbf{m}| = 1$).

These two hypotheses mean that micromagnetism is not valid in some peculiar situations, such as states involving a Bloch point singularity. Simulations taking account of quantum-mechanical effects have to be used in that case.

In micromagnetic simulations, a particular attention has to be paid to length scales in order to always comply with the fundamental hypotheses of the micromagnetic model. The simulated system is divided into elementary cells, the micromagnetic equations being solved in each of these elements. The accuracy of the result depends strongly on the element size; the smaller, the more accurate, but also the longer the simulation. Therefore, an appropriate cell size has to be chosen. Since the exchange interaction has the shortest range, its strength with respect to other forces determines the typical scale over which the magnetisation can vary. Two characteristic lengths can be defined: the exchange length l_{ex} and the Bloch length l_B. The former results from the competition between the exchange interaction and the demagnetising field; it is proportional to the size of a Bloch line (vortex core):

$$l_{ex} = \sqrt{\frac{2A_{ex}}{\mu_0 M_s^2}} \tag{1.91}$$

On the other hand, the Bloch length is the typical width of a Bloch wall (transition between two domains over which the magnetisation rotates perpendicularly to the plane of the wall). It is given by the relative strength of the exchange interaction over the magnetocrystalline anisotropy:

$$l_B = \sqrt{\frac{A_{ex}}{K_u}} \tag{1.92}$$

For accurate micromagnetic simulations, the element size has to be smaller than these two lengths. For instance, in permalloy, the cell dimension is limited by the exchange length which is about 5nm. Therefore an accurate simulation requires a typical cell size of about 2.5nm.

1.1.6 Macrospin

Uniformly magnetised ellipsoid

Generally, the effective field inside a ferromagnetic sample is non-uniform. However, in the particular case of a body whose the surface is of second-degree, a uniform magnetisation state implies a uniform demagnetising field, hence a single-domain state at equilibrium. Choosing the Cartesian coordinates along the principal axes of the system, the equation of the surface boundary is

$$\left(\frac{x}{a}\right)^2 + \left(\frac{y}{b}\right)^2 + \left(\frac{z}{c}\right)^2 = 1, \tag{1.93}$$

where a, b and c are the semi-axis lengths. If $c \to \infty$, the surface is an infinite cylinder of elliptical cross-section. If a, b and c all take finite values, the body is an ellipsoid. For a uniformly magnetised ellipsoid, there is no magnetostatic volume charges ($\rho_m = 0$).

Writing the expression of the surface charges σ_m and recasting it into equation 1.64, it can be shown [30, 31, 32] that the demagnetising field is also uniform. There exists a demagnetisation tensor $\mathcal{N}$ such that

$$\mathbf{H_d} = -\mathcal{N}\mathbf{M}. \tag{1.94}$$

This equation is very convenient, since the demagnetising field does not require heavy computation, contrary to the general case of non-uniform magnetisation. The tensor $\mathcal{N}$ is diagonal if expressed in the basis of the principal axes:

$$\mathcal{N} = \begin{pmatrix} N_{xx} & 0 & 0 \\ 0 & N_{yy} & 0 \\ 0 & 0 & N_{zz} \end{pmatrix} \tag{1.95}$$

The demagnetising coefficients N_{xx}, N_{yy} and N_{zz} are positive, since the field $\mathbf{H_d}$ "demagnetises" the sample. Moreover, the trace of $\mathcal{N}$ is equal to 1, i.e.

$$N_{xx} + N_{yy} + N_{zz} = 1. \tag{1.96}$$

The analytical expressions of the demagnetising factors are well-known for the three types of ellipsoids of revolution: (1) $a = b = c$: sphere, (2) $a = b > c$: oblate spheroid, (3) $a = b < c$: prolate spheroid. The case of the sphere is the most simple, with $N_{xx} = N_{yy} = N_{zz} = \frac{1}{3}$, due to the symmetry. The formulae in the two other cases can be found in ref. [33].

The expression of the demagnetising energy is much more simple than in the general case, due to the uniformity of $\mathbf{H_d}$. Substituting formula 1.94 in equation 1.67 yields

$$E_d = \frac{1}{2}\mu_0 V M_s^2 \left(N_{xx}m_x^2 + N_{yy}m_y^2 + N_{zz}m_z^2\right) \tag{1.97}$$

In fact, the demagnetising factors are related to the aspect ratio of the system: if the ellipsoid is long in the z-direction (c is large), then N_{zz} is small; in contrast, a flat ellipsoid will have a largel N_{zz} value. According to equation 1.97, a system governed by the magnetostatic energy will have a ground state along the axis with the smallest demagnetising factor. Therefore, the magnetisation is preferentially aligned along the largest dimension of the system. This principle is known as *shape anisotropy*. The shape anisotropy must not be confused with magnetocrystalline anisotropy: the former arises from the surface charges distribution σ_m induced by a certain shape of the sample, whereas the latter stems from lattice symmetry. The easy axis of the shape anisotropy is not related to the easy axis of the magnetocrystalline anisotropy. In experiments, the direction called easy axis is in fact a combination of both anisotropies.

The macrospin approximation

As seen in section 1.1.5, the typical length of magnetisation variation is the exchange length l_{ex} (or the Bloch length l_B). Therefore, if the lateral size of a ferromagnetic sample is equal to a few times the exchange length, the magnetisation can be considered as uniform. This approximation is called *macrospin approximation* (or *single-domain approximation*, or *uniform-mode approximation*). Instead of using the complicated formula 1.64, the mean demagnetising field and the magnetostatic energy can be calculated easily with an equivalent demagneting tensor (equation 1.94). The macrospin approximation is of great interest to build simple analytical models. Moreover, the LLG equation is solved for only one spin (a "macro-spin"), which makes macrospin simulations much faster than micromagnetic computations. Analytical expressions of demagnetising factors are known for cylinders [34, 35, 36] and rectangular platelets [37]. Numerical computations are also possible for arbitrary shapes (for more details, see ref. [38] and references therein).

In macrospin, the Gibbs free energy is

$$E_{tot} = \frac{1}{2}\mu_0 M_s^2 V \left(N_{xx}m_x^2 + N_{yy}m_y^2 + N_{zz}m_z^2\right) + K_u V \left[1 - (\mathbf{u_K}\cdot\mathbf{m})^2\right] - \mu_0 M_s V \mathbf{m}\cdot\mathbf{H_{app}} \tag{1.98}$$

The exchange energy is zero, since the magnetisation is uniform.

The energy landscape can be plotted within the macrospin approximation since the state of the system is fully given by two independent parameters (the third one being deduced from the conservation of the norm). This is particularly useful to gain an insight into dynamic processes, such as magnetisation reversal for example. Simple models can also be constructed and solved analytically, such as the Stoner-Wohlfarth model [39] explaining magnetic hysteresis during switching, and the Kittel law [40] giving the FMR (Ferromagnetic Resonance) frequency of the uniform mode as a function of the applied field:

$$f = \frac{\gamma_0}{2\pi}\sqrt{\left(H_{app} + (N_{yy} - N_{zz})M_s\right)\left(H_{app} + (N_{xx} - N_{zz})M_s\right)}, \tag{1.99}$$

in the case $K_u = 0$ and $\mathbf{H_{app}} = H_{app}\mathbf{\hat{u}_z}$. This equation is derived with $\alpha = 0$; therefore, the oscillation trajectory has a constant energy.

The whole model presented here has been developed in absence of current. The main equation of this section, the LLG equation 1.32, is indeed dissipative. In the next section, we will add the current and will give a simple description of the spin transfer effect.

1.2 Spin-dependent transport theory

The magnetoresistance is related to the action of the magnetic state on a spin-polarised current. Conversely, the spin transfer is the effect of a spin-polarised current on the magnetisation. In metallic multilayer, the giant magnetoresistance (GMR) effect, discovered by Fert [2] and Grünberg [3] can be explained by a difference in the resistivity for spin up

and spin down electrons in metallic multilayer. It is useful in various applications such as Magnetic Random Access Memory (MRAM) because it allows to detect the magnetic state of the storage layer. The spin-transfer effect was predicted in 1996 by Slonczewski [41] and Berger [42], and experimentally observed from 1998 [43, 44, 45, 4]. Since then, spin-transfer has been a very active research topic due to its potential applications, such as STT-MRAM [45, 4, 46, 47, 48, 49, 50], Spin-Torque Oscillator [51, 52], and racetrack memory [5]. In STT-MRAM, switching is induced by spin-torque instead of being triggered by a magnetic field; in Spin-Torque Oscillator, magnetisation oscillation is driven by a spin-polarised current, which allows to tune the frequency by varying the current intensity; finally, spin-torque-induced domain wall motion may be utilised to write series of data bits in racetrack memory.

The aim of this section is to introduce the spin-torque term that will be introduced in the LLG equation for micromagnetic simulations.

1.2.1 Ballistic model

The system studied is illustrated on figure 1.3. It comprises two ferromagnetic layers (F_1 and F_2) separated by a thin Cu layer. Each ferromagnets is connected to a metallic electrode. A current flows perpendicular to the plane of the layers from the left to the right-hand side. F_1 is thick such that its magnetisation $\mathbf{M_1}$ is assumed to be fixed. F_2 is thin and its magnetisation $\mathbf{M_2}$ is free to move under the action of the current. For simplicity, $\mathbf{M_1}$ and $\mathbf{M_2}$ are supposed uniform (macrospin approximation). Thus, the system can be reduced to a 1D-model. Moreover, we consider the case of non-collinear magnetisations $\mathbf{M_1}$ and $\mathbf{M_2}$.

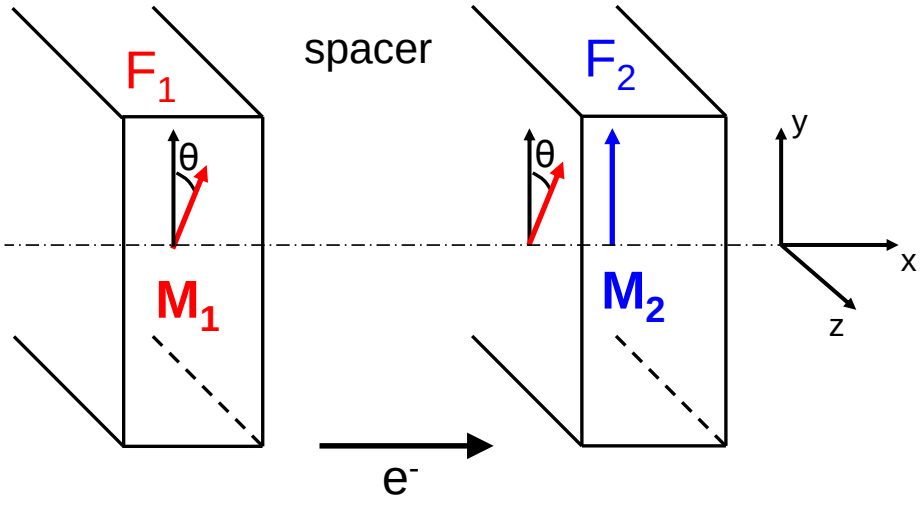

Figure 1.3: Model of trilayer studied. F_1 is ferromagnetic layer with fixed magnetisation. The spin transfer torque acts on F_2.

In transition metals (Fe, Ni, Co), the conduction electrons are mainly $4s$ electrons, while electrons in the $3d$ shell contribute to the local magnetisation. The $s-d$ exchange interaction accounts for *spin filtering* that aligns the spins of s and d electrons.

In the fixed ferromagnet F_1, the spins are aligned with $\mathbf{M_1}$. However, in F_2, where the magnetisation has a different angle, the spins cannot stay in the same direction, due to the $s-d$ exchange interaction. Therefore, they tend to align with $\mathbf{M_2}$. Since the angular momentum has to be conserved, it means that the transverse component of the spin is absorbed and transferred to $\mathbf{M_2}$. This "spin transfer" yields a torque that is exerted on $\mathbf{M_2}$. The *Spin-Transfer Torque* (STT) is zero if the two macrospins $\mathbf{M_1}$ and $\mathbf{M_2}$ are parallel. In reality, a torque is also exerted on $\mathbf{M_1}$, but it is weaker, due to the asymmetry of the layers.

If the electrons flow from the right to the left-hand side, they are polarised in F_2 and transmitted through the spacer. At the interface Cu/F_1, the longitudinal component is transmitted in F_1 while the transverse component is mainly reflected. Consequently, F_2 experiences a torque that pushes its magnetisation to be antiparallel to M_1.

In such a structure, called *spin valve*, the magnetisation of a thin layer can therefore be oriented parallel or antiparallel to the thick layer magnetisation; a spin-transfer magnetic memory is thus realised.

The expression of the spin torque can be derived using simple arguments. Hereafter, θ denotes the angle between $\mathbf{M_1}$ and $\mathbf{M_2}$, j the current density, j_s the spin current density equal to $-\frac{\hbar}{2|e|}(j_\uparrow - j_\downarrow)$ (where $j_\uparrow$ and $j_\downarrow$ are the current densities for spin up and spin down), $\mathcal{P}$ will be the spin polarisation in the spacer, that is the average of the projection of the spins along the $\mathbf{m_1}$ direction, and A will denote the cross-sectional area of the spin-valve.

The number of electrons crossing F_2 by unit time is $Aj/|e|$. In the spacer, the mean spin of the electrons is $\mathcal{P}\hbar/2$. Therefore, the spin current along $\mathbf{m_1}$ is $\frac{\mathcal{P}\hbar}{2}\frac{Aj}{|e|}$. The spin torque in F_2, is equal to the spin current transverse to $\mathbf{M_2}$ at the spacer/F_2 interface. Projecting the spin current in the direction perpendicular to $\mathbf{M_2}$ yields

$$\boldsymbol{\mathcal{T}} = A\mathcal{P}\sin\theta\,\frac{\hbar j}{2|e|}\mathbf{u_z} \tag{1.100}$$

This formula shows that the torque depends on the direction of the current, as mentioned earlier. Since $\sin\theta\,\mathbf{u_z} = \mathbf{m_2}\times(\mathbf{m_2}\times\mathbf{m_1})$, then

$$\boldsymbol{\mathcal{T}} = A\mathcal{P}\frac{\hbar j}{2|e|}\mathbf{m_2}\times(\mathbf{m_2}\times\mathbf{m_1}) \tag{1.101}$$

To obtain the variation of $\mathbf{m_2}$ due to the spin torque, $\boldsymbol{\mathcal{T}}$ has to be multiplied by γ_0/M_s and divided by the volume of F_2, which is $V = At$ (with t being the thickness of F_2). Therefore, one obtains

$$\left(\frac{d\mathbf{m_2}}{dt}\right)_{ST} = \mathcal{P}\frac{\gamma_0\hbar j}{2t|e|M_s}\mathbf{m_2}\times(\mathbf{m_2}\times\mathbf{m_1}) \tag{1.102}$$

This spin-torque term can then be added to the LLG equation (1.32), yielding

$$\frac{\partial \mathbf{m_2}}{\partial t} = -\gamma_0 \left(\mathbf{m_2} \times \mathbf{H_{eff}}\right) + \alpha \left(\mathbf{m_2} \times \frac{\partial \mathbf{m_2}}{\partial t}\right) + \mathcal{P} \frac{\gamma_0 \hbar j}{2t|e|M_s} \mathbf{m_2} \times \left(\mathbf{m_2} \times \mathbf{m_1}\right) \tag{1.103}$$

In reality, the polarisation factor depends on the angle between the two magnetisations. In ref [41], Slonczewski gave an expression of $\mathcal{P}$:

$$\mathcal{P}(\theta) = \left[-4 + \frac{(1+\eta)^3}{4\eta^{3/2}} \left(3 + \mathbf{m_1} \cdot \mathbf{m_2}\right)\right]^{-1} \tag{1.104}$$

where η is a fixed parameter. Later on in this thesis, this function will be called $g(\eta, \theta)$. It is plotted on the figure 1.4.

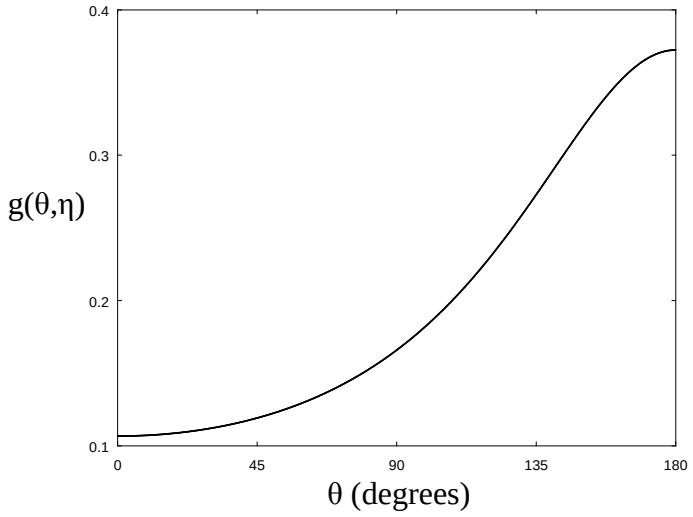

Figure 1.4: The spin efficiency $g(\eta, \theta)$ as a function of the angle θ between the polarisation vector $\mathbf{p}$ and the magnetisation $\mathbf{m}$. Here, the polarisation value is $\eta = 0.3$.

This form of the spin efficiency has been generalised by Xiao *et al.* [53]:

$$\mathcal{P}(\theta) = \frac{q_+}{B_0 + B_1 \cos\theta} + \frac{q_-}{B_0 - B_1 \cos\theta}. \tag{1.105}$$

However, the Slonczewski formula 1.104 will be used in the micromagnetic simulations instead of the more general one because only one parameter (namely, η) is required.

Henceforth, we will refer to the equation

$$\boxed{\frac{\partial \mathbf{m}}{\partial t} = -\gamma_0 \left(\mathbf{m} \times \mathbf{H_{eff}}\right) + \alpha \left(\mathbf{m} \times \frac{\partial \mathbf{m}}{\partial t}\right) + \gamma_0 a_J \mathbf{m} \times \left(\mathbf{m} \times \mathbf{p}\right)} \tag{1.106}$$

as the Landau-Lifshitz-Gilbert-Slonczewski (LLGS) equation. $\mathbf{p}$ is the direction of the

"pinned" layer and a_J is

$$a_J(\theta,\eta) = \frac{\hbar}{2|e|}\frac{g(\theta,\eta)}{\mu_0 M_s t}J, \tag{1.107}$$

with $g(\eta,\theta)$ having the expression of $\mathcal{P}$ in equation 1.104.

The spin-torque is another non-conservative term in the equation of motion. Depending on the direction of $\mathbf{m}\times(\mathbf{m}\times\mathbf{p})$, it can increase or decrease the energy of the system. A sustained oscillation is possible when the magnetisation trajectory is such that the damping and the spin-torque compensate over one period.

In this model, several assumptions have been made:

- Scattering inside the spacer is neglected.
- Electrons keep the direction of their spin when crossing the spacer, which results in current polarised along $\mathbf{m_1}$ at the spacer/F_2 interface.
- The decay length of the transverse component of the spin is smaller than t, the thickness of F_2 and smaller than the mean free path, hence the *ballistic* approach.
- The longitudinal component is conserved in F_2.

When the electrons are transmitted in the ferromagnet F_2, spin up and spin down electrons have different wave vectors $k_\uparrow$ and $k_\downarrow$, due to the $s-d$ interaction. The difference in velocity results in a phase shift $\Delta\phi(x) = \phi(x) - \phi(0) = \Delta k\, x$ that causes the spins to precess in space. The decay length is $l_\perp \approx \pi/|k_\uparrow - k_\downarrow|$. *Ab-initio* calculations [54, 55] and experiments [56] showed that, at the Cu/Co interface, the transverse component is completely absorbed after $l_\perp \approx 1\,\text{nm}$. Thus, the spin-torque can be considered as an interface effect but the Heisenberg exchange interaction that connects local magnetic moments propagate the influence of the spin-torque to the whole layer.

The absorption of the transverse component, responsible for the spin-torque occurs on a very short scale which is smaller than the typical thickness t of F_2 in spin-valves. However, the longitudinal component, assumed to be conserved in the previous section, is also absorbed, but on a much larger distance l_{sf}, called the *spin-flip length* or *spin diffusion length*. To summarise,

$$l_{sf} \gg t \gg l_\perp \tag{1.108}$$

The ratios between these length scales support the ballistic approach describing the transverse component and the diffusive treatment of the longitudinal spins.

1.2.2 Diffusive approach

From the point of view of quantum mechanics, the charge current density $\mathbf{j_e}$ associated to the charge density $n_e = -|e|\psi^*\psi$ is defined as

$$\mathbf{j_e} = -\frac{i\hbar e}{2m}\left(\psi\nabla\psi^* - \psi^*\nabla\psi\right) = -\frac{\hbar e}{m}\mathrm{Im}\left(\psi^*\nabla\psi\right), \tag{1.109}$$

where ψ is the wave function. In addition, the spin current associated to the spin density $\mathbf{n_s} = \frac{\hbar}{2}\psi^*\boldsymbol{\sigma}\psi$ is

$$\mathbf{Q} = \frac{i\hbar^2}{4m}\left(\psi\boldsymbol{\sigma}\nabla\psi^* - \psi^*\boldsymbol{\sigma}\nabla\psi\right) = \frac{\hbar^2}{2m}\mathrm{Im}\left(\psi^*\boldsymbol{\sigma}\otimes\nabla\psi\right). \tag{1.110}$$

where $\otimes$ denotes the tensor product. $\mathbf{Q}$ is a 3×3 matrix since there are three spatial coordinates and three components for the spin.

Moreover, the *spin accumulation* is defined as

$$\delta\mathbf{m} = \left(|\mathbf{n_s}| - |\mathbf{n_{s,eq}}|\right)\hat{\mathbf{n}}_\mathbf{s} \tag{1.111}$$

The continuity equations related to the charge and the spin are

$$\frac{\partial n_e}{\partial t} + \nabla\cdot\mathbf{j_e} = 0 \tag{1.112}$$

$$\frac{\partial \mathbf{n_s}}{\partial t} + \nabla\cdot\mathbf{Q} = -\frac{\delta\mathbf{m}}{\tau_{sf}} - \frac{1}{\tau_{sd}}\mathbf{n_s}\times\mathbf{m} \tag{1.113}$$

The charge is conserved, hence the zero value in the right-hand side of equation 1.112. In contrast, the transverse and the longitudinal components of the spin are not conserved. Thus, in equation 1.113, the first term on the right-hand side accounts for *spin-flip*, that is the reversal of the longitudinal component, due to the interaction with the lattice. The spin-flip characteristic time τ_{sf} is about 10^{-12} s [57]. Finally, the last term of equation 1.113 describes the absorption of the transverse component due to the $s-d$ interaction, and therefore is proportional to the spin-torque. The order of magnitude of the $s-d$ time constant is $\tau_{sd}\sim 10^{-14}$ s [57].

Moreover, according to ref.[58], the charge current $\mathbf{j_e}$ and the spin current $\mathbf{Q}$ are solutions of the equations

$$\mathbf{j_e} = 2C_0\mathbf{E} - D_0\nabla n_e - \mathbf{D}\cdot\nabla\mathbf{n_s} \tag{1.114}$$

$$\mathbf{Q} = 2\mathbf{C}\mathbf{E} - \mathbf{D}\nabla n_e - D_0\nabla\mathbf{n_s} \tag{1.115}$$

where C_0 is a scalar number and $\mathbf{C}$ is a 2×2 matrix representing the conductivity, and D_0 is a scalar number and $\mathbf{D}$ is a 2×2 matrix representing the diffusion constant. These two equations have to be solved together with the two continuity equations 1.112 and 1.113 in order to compute the charge and spin accumulation for given a distribution of magnetisation and electric field. Once the spin accumulation has been computed in each node of the system mesh, the spin torque can be calculated and injected into the modified LLG equation

$$\frac{\partial\mathbf{m}}{\partial t} = -\gamma_0\left(\mathbf{m}\times\mathbf{H_{eff}}\right) + \alpha\left(\mathbf{m}\times\frac{\partial\mathbf{m}}{\partial t}\right) + \frac{V_0 M_s}{\hbar\mu_B}\boldsymbol{\mathcal{T}}_{\mathbf{spin\text{-}transfer}} \tag{1.116}$$

where μ_B is the Bohr magneton, V_0 is the elementary volume occupied by a magnetic

moment, and $\boldsymbol{\mathcal{T}}_{\mathbf{spin\text{-}transfer}} = -(\mathbf{n_s} \times \mathbf{m})/\tau_{sd}$. The equations are coupled because the magnetisation at the end of the new time step is then injected into the transport equation 1.113 that can be rewritten

$$\frac{\partial \mathbf{n_s}}{\partial t} + \nabla \cdot \mathbf{Q} = -\frac{\delta \mathbf{m}}{\tau_{sf}} + \boldsymbol{\mathcal{T}}_{\mathbf{spin\text{-}transfer}} \tag{1.117}$$

The magnetisation motion modifies the spin accumulation which changes the spin-torque acting on the magnetisation. Solving this system numerically is possible. The characteristic times of spin relaxation are much shorter than the typical time of magnetisation precession, therefore one can assume that at each time step, the spin accumulation is at equilibrium. Thus, one can remove the time-varying term in equation 1.117. After each time step leading to a new position of the magnetisation vector, the spin accumulation is computed in the whole nanostructure. Then, a new value of the spin-torque is deduced and inserted in the LLG equation 1.116. A numerical solver using this method is currently under development in Néel Institut and Spintec and a similar approach is used in the commercial software Spinflow 3D™ [59].

Field-like torque

In reality, electrons are not totally transmitted at the spacer/F_2 interface (figure 1.3); a part is reflected. Integrating equation 1.117 over a pillbox straddling the spacer/F_2 interface yields

$$\boldsymbol{\mathcal{T}}_{\mathbf{spin\text{-}transfer}} = \left(\mathbf{Q}^{\mathbf{incident}} + \mathbf{Q}^{\mathbf{reflected}} - \mathbf{Q}^{\mathbf{transmitted}}\right) \cdot \mathbf{u_x} \tag{1.118}$$

The equation is derived at equilibrium ($\partial/\partial t = 0$) and the term accounting for spin-flip is neglected given the large value of the spin diffusion length.

After further derivation, the influence of the reflected electrons leads to a new term in the spin torque, proportional to $\mathbf{m} \times \mathbf{p}$. The total spin-torque is then

$$\boldsymbol{\mathcal{T}}_{\mathbf{spin\text{-}transfer}} = \gamma_0 a_J \mathbf{m} \times (\mathbf{m} \times \mathbf{p}) + \gamma_0 b_J \mathbf{m} \times \mathbf{p} \tag{1.119}$$

where b_J is a phenomenological constant. The term $\gamma_0 b_J \mathbf{m} \times \mathbf{p}$ can be included in the expression of the effective field, it is therefore called the *field-like torque*. In contrast, $\gamma_0 a_J \mathbf{m} \times (\mathbf{m} \times \mathbf{p})$ is often referred to as the *Slonczewski torque* or the *in-plane torque*.

In spin valves, the b_J coefficient is usually much smaller than the a_J term. Therefore, only the Slonczewski torque is considered in the simulations.

The equation 1.119 is a very general expression of the spin torque. It can also be used to model Magnetic Tunnel Junction (MTJ) where the metallic layer is replaced with a tunnel barrier (most often MgO). In MTJ, the b_J coefficient is larger (typically, 20% of the a_J value).

All the physical concepts have now been introduced. In the next section, we will summarise the main numerical methods used in the micromagnetic solvers and finally present our 3D Finite Element code: feeLLGood.

1.3 Numerical micromagnetism

In most cases, the macrospin model is a very rough approximation. Micromagnetic simulations are required for a description of non-uniform magnetisation. There are two types of micromagnetic simulations: either the equilibrium state is sought, or a complete time-varying computation is run to study magnetisation dynamics. Usually, the equilibrium state is needed to initialise the dynamic simulation. The most common method to find the micromagnetic equilibrium state is to relax the system with a large α value, as mentioned at the end of section 1.1.2.

For simulations of magnetisation dynamics, the Landau-Lifshitz-Gilbert equation is solved numerically. Time and space are discretised and the effective field is calculated in each element (or cell) at each time step. An approximate solution is given, but it has to converge to the exact result when the element size and the time step go to zero. Typical time step is about 0.1ps (for typical cell size, see section 1.1.5). The input parameters of any micromagnetic simulation are: the saturation magnetisation M_s, the exchange constant A_{ex} and the anisotropy constant K_u. Moreover, the temperature T can be included as well as the current density J and the spin polarisation η (for STT simulations with the Slonczewski model).

There exists mainly two numerical methods to solve micromagnetic equations: the Finite Difference Method (FDM) and the Finite Element Method (FEM). They will be presented in this section.

1.3.1 Finite Difference Method

The Finite Difference Method (FDM) is the most common numerical method for micromagnetic simulations, because it is easier to implement than the Finite Element Method (FEM) and because it is also faster. The most widely used micromagnetic code utilising the FDM is certainly the OOMMF software [60], but many other software can be cited, such as LLG Micromagnetic Simulator by M. R. Scheinfein [61], MicroMagus by D. V. Berkov and N. L. Gorn [62], MuMax by A. Vansteenkiste and B. Van de Wiele [63], GoParallel by L. Torres and E. Martinez [64], and MicroMagnum by A. Drews [65]. The last three software use graphics cards (GPUs) whereas the other ones run only on single processors (CPU). GPU computing has been intensively developed for the past ten years due to the ability of recent GPUs to process rapidly a great amount of data. However, not all algorithms efficiently run on GPUs because they need to be "parallelisable": the input is split and processed at the same time by a large number of cores that perform the same operation. Basic operations like addition and multiplication can be executed, but advanced mathematical functions still require a CPU.

During this PhD, Finite Difference simulations were performed with a software called ST_GL-FFT, developed in *Néel Institut* and *Spintec*. Therefore, in this section, emphasis will be placed on the numerical methods utilised in this code.

The FDM consists in discretising the system into small cells, usually identical rectangular prisms. As a consequence, the edge of rounded geometries is described by a "staircase" instead of a smooth curve (figure 1.5). In this case, the simulated system is therefore not exactly the one aimed at being simulated. Moreover, the roughness of the edge does not mimic the real roughness of the sample because it breaks its symmetry. In some cases, the staircase-like edge generates artefacts which are not easy to identify as such. Most often, users of micromagnetic codes are not aware of these issues and can be misled by the results of their simulations. All in all, Finite Difference softwares provide consistent output for rectangular shapes, but the results on elliptical systems have to be interpreted with caution.

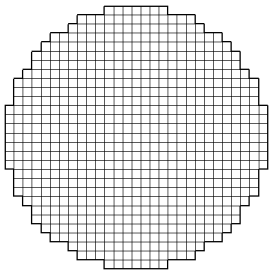

Figure 1.5: Finite difference mesh of a circular sample. The regular grid results in a rough border.

The regular Finite-Difference mesh comprises N_x cells along the x-direction, N_y cells in the y-direction and N_z cells along z. Each cell has a volume $\delta_x\delta_y\delta_z$ and will be labelled with the indices ijk (with $(i,j,k) \in \{1..N_x\} \times \{1..N_y\} \times \{1..N_z\}$). The LLG equation is solved in the centre of the cells, and the effective field is evaluated after each time step.

Spatial derivatives

In FDM, spatial derivatives are easily computed from the magnetisation difference between neighbouring cells. This is very useful for the calculation of the demagnetising field requiring the first-order derivative and for the exchange field computed from the second-order derivative. According to the *centred-difference approximation*, the expressions of the first- and second-order spatial derivatives are

$$\frac{\partial \mathbf{m}}{\partial x}(i,j,k) = \frac{\mathbf{m}(i+1,j,k) - \mathbf{m}(i-1,j,k)}{2\delta_x} + \mathcal{O}(\delta_x^2) \tag{1.120}$$

$$\frac{\partial^2 \mathbf{m}}{\partial x^2}(i,j,k) = \frac{\mathbf{m}(i+1,j,k) - 2\mathbf{m}(i,j,k) + \mathbf{m}(i-1,j,k)}{\delta_x^2} + \mathcal{O}(\delta_x^2) \tag{1.121}$$

Exchange field

Following equations 1.46 and 1.121, the exchange field is

$$\mathbf{H_{ex}} = \frac{2A_{ex}}{\mu_0 M_s}\left[\frac{\mathbf{m}(i+1,j,k)-2\mathbf{m}(i,j,k)+\mathbf{m}(i-1,j,k)}{\delta_x^2} + \frac{\mathbf{m}(i,j+1,k)-2\mathbf{m}(i,j,k)+\mathbf{m}(i,j-1,k)}{\delta_y^2} + \frac{\mathbf{m}(i,j,k+1)-2\mathbf{m}(i,j,k)+\mathbf{m}(i,j,k-1)}{\delta_z^2}\right] + \mathcal{O}(\delta_x^2,\delta_y^2,\delta_z^2) \quad (1.122)$$

Other expressions of the spatial derivatives could be used [19] in order to obtain the same accuracy for the exchange field, but with larger cells. However, Donahue and McMichael [66] showed the drawbacks of these methods.

Demagnetising field

The most common approach consists in considering that the magnetisation is uniform inside each cell [67, 68, 69, 70, 71]. Thus, the distribution of surface charges is constant on each face of the cells and there is no volume charges (since $\nabla \cdot \mathbf{M} = 0$). Another approach, referred to as the *constant volume charges method* [72], lies on the hypothesis that $\nabla \cdot \mathbf{M}$ is constant within each cell. These two methods are compared in ref. [73].

The equation 1.64 expresses the demagnetising field as a function of the magnetic charge distribution and the Green's function. The convolution product involved in this equation is not very convenient for numerical computations. However, a theorem states that the Fourier transform of a convolution product is equal to the product of the Fourier transforms. Using this theorem, the equation 1.64 can be rewritten as

$$\mathbf{H_d}(\mathbf{r}) = -\mathcal{F}^{-1}\left[\mathcal{F}\left(\nabla G\right)\mathcal{F}\left(\rho_m\right) + \mathcal{F}\left(\nabla G\right)\mathcal{F}\left(\sigma_m\right)\right], \quad (1.123)$$

where $\mathcal{F}$ and $\mathcal{F}^{-1}$ denote the Fourier transform and its inverse. As mentioned earlier, the mesh is regular; this property proves very useful for the computation of the Fourier Transform. Indeed, it is replaced with a Discrete Fourier Transform that can be calculated easily with the well-known Fast Fourier Transform (FFT) algorithm (see ref. [74] for a deeper insight).

Magnetocrystalline anisotropy

The derivation of the uniaxial anisotropy field is straightforward:

$$\mathbf{H_{anis}}(i,j,k) = \frac{2K_u}{\mu_0 M_s}\left[\mathbf{m}(i,j,k)\cdot\mathbf{u_K}\right]\mathbf{u_K} \quad (1.124)$$

Time schemes

In explicit schemes, the unknown variable (here $\mathbf{m}$) at time $t + \Delta t$ is explicitly expressed as a function of the state of the system at current time t. Approximating $\mathbf{f}(t + \Delta t)$ by

$$\mathbf{f}(t, \mathbf{m}_t) = \frac{\mathbf{m}_{t+\Delta t} - \mathbf{m}_t}{\Delta t} + \mathcal{O}(\Delta t) \tag{1.125}$$

yields

$$\mathbf{m}_{t+\Delta t} = \mathbf{m}_t + \mathbf{f}(t, \mathbf{m}_t)\Delta t + \mathcal{O}(\Delta t^2), \tag{1.126}$$

known as the *explicit Euler method* or *forward Euler method*.

Instead of being expressed at time $t + \Delta t$, the approximate derivative can also be written at the instant t. In this case,

$$\mathbf{f}(t + \Delta t, \mathbf{m}_{t+\Delta t}) = \frac{\mathbf{m}_{t+\Delta t} - \mathbf{m}_t}{\Delta t} + \mathcal{O}(\Delta t) \tag{1.127}$$

Then, the implicit scheme (*backward Euler method*) reads

$$\mathbf{m}_t \approx \mathbf{m}_{t+\Delta t} - \mathbf{f}(t + \Delta t, \mathbf{m}_{t+\Delta t})\Delta t + \mathcal{O}(\Delta t^2). \tag{1.128}$$

Finding $\mathbf{m}_{t+\Delta t}$ requires solving this algebraic equation. Further computation is therefore needed.

Other methods can be used to solve the magnetisation dynamics, such as the Crank-Nicolson ("semi-implicit") method. Summing equations 1.125 and 1.127 of the forward and backward Euler methods leads to

$$\frac{\mathbf{f}(t + \Delta t, \mathbf{m}_{t+\Delta t}) + \mathbf{f}(t, \mathbf{m}_t)}{2} \approx \frac{\mathbf{m}_{t+\Delta t} - \mathbf{m}_t}{\Delta t}, \tag{1.129}$$

that can be rewritten as

$$\mathbf{m}_{t+\Delta t} - \frac{\Delta t}{2}\mathbf{f}(t + \Delta t) \approx \mathbf{m}_t + \frac{\Delta t}{2}\mathbf{f}(t), \tag{1.130}$$

As for the implicit Euler method, solving the state at $t + \Delta t$ for the Crank-Nicolson method requires a few more calculation steps [74]. The Crank-Nicolson scheme is not exactly order 2, because of the renormalisation.

Implicit (and "semi-implicit") methods do not give explicitly $\mathbf{m}(t + \Delta t)$ and therefore necessitate solving a system of linear equations. Consequently, the computation time of one step is longer than for the explicit method. However, they are more stable than the explicit Euler method, meaning that time steps can be larger. For this reason, implicit time schemes are preferred. Nonetheless, specific explicit schemes exist [75] which conserve the norm of $\mathbf{m}$ constant at each time step. One of them is detailed below.

The ST_GL-FFT time scheme

The ST_GL-FFT code used for some simulations during this PhD utilises an explicit scheme that we are going to present. In this section, the time is renormalised with the transformation

$$t \leftarrow \frac{\gamma_0 t}{1+\alpha^2}. \tag{1.131}$$

Denoting $\mathbf{H}$ the field

$$\mathbf{H}(t) = \mathbf{H_{eff}}(t) + \alpha \mathbf{m}(t) \times \mathbf{H_{eff}}(t), \tag{1.132}$$

it follows that the LLG equation can be written as

$$\frac{\partial \mathbf{m}}{\partial t} = -\mathbf{m}(t) \times \mathbf{H}(t). \tag{1.133}$$

The magnetisation vector at time $t + \Delta t$ can be derived by Taylor expansion:

$$\begin{aligned} \mathbf{m}(t+\Delta t) &= \mathbf{m}(t) + \sum_{n=1}^{\infty} \frac{(\Delta t)^n}{n!} \frac{d^n \mathbf{m}}{dt^n} \\ &= \mathbf{m}(t) + \sum_{p=0}^{\infty} \frac{(\Delta t)^{2p}}{(2p)!} \frac{d^{2p}\mathbf{m}}{dt^{2p}} + \sum_{p=1}^{\infty} \frac{(\Delta t)^{2p+1}}{(2p+1)!} \frac{d^{2p+1}\mathbf{m}}{dt^{2p+1}} \end{aligned} \tag{1.134}$$

In the limit of $\mathbf{H}$ varying slowly with time, using equation 1.133, the even-order and odd-order derivatives can be expressed as

$$\frac{d^{2p}\mathbf{m}}{dt^{2p}} = (-H^2)^{p-1} \frac{d^2\mathbf{m}}{dt^2} = (-H^2)^{p-1} \mathbf{H} \times \frac{d\mathbf{m}}{dt} \tag{1.135}$$

$$\frac{d^{2p+1}\mathbf{m}}{dt^{2p+1}} = (-H^2)^{p} \frac{d\mathbf{m}}{dt} \tag{1.136}$$

which yields

$$\mathbf{m}(t+\Delta t) = \mathbf{m}(t) + \sum_{p=0}^{\infty} \frac{(\Delta t)^{2p}}{(2p)!} (-1)^p H^{2p} \frac{d\mathbf{m}}{dt} + \sum_{p=1}^{\infty} \frac{(\Delta t)^{2p+1}}{(2p+1)!} (-1)^{p-1} H^{2p-2} \mathbf{H} \times \frac{d\mathbf{m}}{dt} \tag{1.137}$$

One recognises the Taylor expansion of the sine and cosine functions, which leads to the analytical formula

$$\mathbf{m}(t+\Delta t) = \mathbf{m}(t)\cos(H\Delta t) + \frac{\sin(H\Delta t)}{H} (\mathbf{H} \times \mathbf{m}(t)) + (1 - \cos(H\Delta t)) \frac{\mathbf{m}(t)\cdot\mathbf{H}}{H^2}\mathbf{H} \tag{1.138}$$

which conserves the norm.

As mentioned earlier, explicit schemes are usually less stable than implicit schemes. Therefore an analysis of the stability is important to determine the maximum time step.

For the ST_GL-FFT time scheme, in the two-dimensional case, this limit is

$$\Delta t_{limit} = \frac{\mu_0 M_s}{8A_{ex}} \left(\frac{1}{\delta_x^2} + \frac{1}{\delta_y^2} + \frac{1}{\delta_z^2} \right)^{-1} \frac{2\alpha}{\alpha^2 + 1} \tag{1.139}$$

In practice, the time step must be chosen much smaller than Δt_{limit} to describe with precision rapid variations magnetisation.

Spin transfer

The Slonczewski spin torque expressed by the last term of the LLGS equation 1.106 can be taken into account by adding a new field to the effective field. Thus, the "spin torque field"

$$\mathbf{H_{ST}} = a_J \, \mathbf{m} \times \mathbf{p} \tag{1.140}$$

is added to $\mathbf{H_{eff}}$ in the LLG equation 1.32. This field does not derive from an energy.

In the FDM, the expression of $\mathbf{H_{ST}}$ is simply

$$\mathbf{H_{ST}}(i,j,k) = a_J \, \mathbf{m}(i,j,k) \times \mathbf{p} \tag{1.141}$$

1.3.2 Finite Element Method

The Finite Element Method (FEM) is a numerical technique for finding approximate solutions to partial differential equations. The studied system is divided into small elements where the equations are solved. Most of the simulations run during this PhD have been performed with a FEM-based software. This micromagnetic solver, called feeLLGood ("Finite Element Equations for LLG with Object-Oriented Development"), was mainly developed at *Institut Néel* by Jean-Christophe Toussaint and Evaggelos Kritsikis who continued the work started by Helga Szambolics [7]. In the magnetism community, FEM-based micromagnetic codes are less often used than the Finite Difference ones, due to their lower speed and the complexity to implement the method itself. However, they have other advantages that justify their use. They are perfectly designed to deal with any kind of geometry, including rounded shapes that the FDM does not describe properly. Indeed, the mesh is unstructured and the elements are not necessarily rectangular prisms but are most often tetrahedra (or triangles in 2D). A typical Finite Element mesh is showed on figure 1.6.

Among other FEM-based micromagnetic solvers, one can cite Nmag, developed by H. Fangohr, M. Franchin and T. Fischbacher, Magpar by W. Scholz, FEMME by D. Suess and T. Schrefl, TetraMAG by R. Hertel, FastMag by V. Lomakin, SallyMM by O. Bottauscio and A. Manzin [76] and Spinflow 3D™, sold by the company *InSilicio* [59].

The main difference between all these codes is the time scheme used to integrate the LLG equation. After presenting generalities about the FEM, the time scheme implemented in feeLLGood will be described in details.

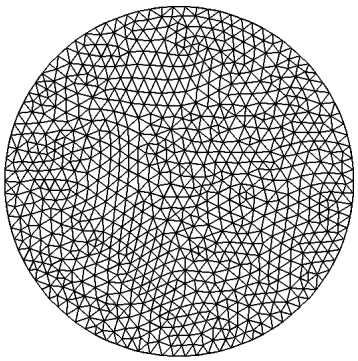

Figure 1.6: Tetrahedral Finite Element mesh of a circular sample. The edge is described with a series of straight lines, almost indistinguishable from a perfectly circular contour.

FEM: a general description

In FEM, the partial differential equation is projected onto test-functions that are piecewise polynomials vanishing at all but one node. Then, the integral over the corresponding domain is solved. The smoothness requirement on the solution is weakened, hence the name *weak formulation*. The method described here is the Galerkin method for FEM. The solving process can be summarised as followed:

1. Determine the weak form by projecting the physical equation onto test functions.
2. Discretise the domain into small elements in order to write the total integral as a sum over each element.
3. Assemble all the element-equations by taking into account the connections between the nodes.
4. Solve the linear system associated with the weak form.
5. Update the magnetisation vector at each node and at each time step.

At step 2, an affine transformation is performed from any element to a reference element in order to express the derivatives of the test-functions.

Time scheme in feeLLGood

In ref [77], Yang and Fredkin suggested to seek the solution of the LLG equation in the space

$$V = \left\{ \sum_{i=1}^{N} \phi_i \mathbf{w_i}, \quad \mathbf{w_i} \in \mathbb{R}^3 \right\} \tag{1.142}$$

where ϕ_i are linear functions in each elements. To enforce the constrain $|\mathbf{m}| = 1$, the magnetisation vector is renormalised after each time step. In ref. [78], Szambolics *et al.* showed the detrimental effect of such a renormalisation, namely, an overestimated dissipation for small α values. These observations support the development of a new

weak formulation [79] (the *Alouges weak form*) keeping the norm of the magnetisation constant. Noticing that $|\mathbf{m}| = 1$ is equivalent to $\mathbf{m} \cdot \frac{\partial \mathbf{m}}{\partial t} = 0$, it is natural to look for the solution of $\partial \mathbf{m}/\partial t$ in the subspace

$$K^n = \left\{ \sum_{i=1}^{N} \phi_i \mathbf{w}_i, \quad \mathbf{w}_i \in \mathbb{R}^3, \quad \mathbf{w}_i \cdot \mathbf{m}_i^n = 0 \right\}, \tag{1.143}$$

where $\mathbf{m}_i^n$ is the value of $\mathbf{m}$ at the node i and time step n. Thus, $\partial \mathbf{m}/\partial t$ at each node is solved in the plane tangent to the unit sphere at the extremity of $\mathbf{m}$.

The equation 1.23 can be rewritten

$$\alpha\, \partial_t \mathbf{m} + \mathbf{m} \times \partial_t \mathbf{m} = \gamma_0 \mathbf{H}_{\mathbf{eff}} - \gamma_0 \left[(\mathbf{H}_{\mathbf{eff}} \cdot \mathbf{m})\, \mathbf{m} \right]. \tag{1.144}$$

Then the weak form can be written: find $\mathbf{v} \in K^n$ such that for all $\mathbf{w} \in K^n$

$$\alpha(\mathbf{v}, \mathbf{w}) + (\mathbf{m}^n \times \mathbf{v}, \mathbf{w}) = \gamma_0 (\mathbf{H}_{\mathbf{eff}}, \mathbf{w}) \tag{1.145}$$

The last term of equation 1.144 being cancelled due to the tangent plane.

Once the equation is solved, the magnetisation is renormalised at the nodes. Denoting k the time step and $\mathbf{m}^{n,1} = \mathbf{m}^n + k\mathbf{v}$, then the renormalised magnetisation is

$$\mathbf{m}^{n+1} = \frac{\mathbf{m}^{n,1}}{|\mathbf{m}^{n,1}|} \tag{1.146}$$

Figure 1.7 illustrates this renormalisation.

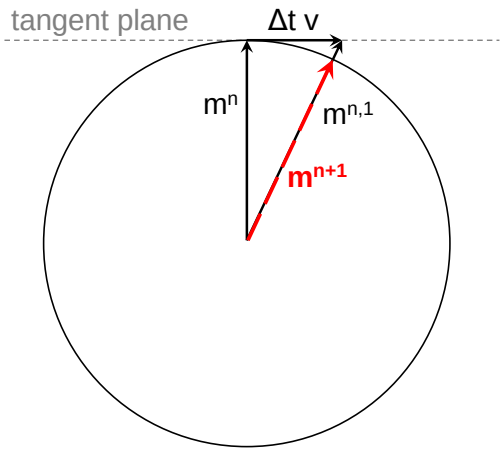

Figure 1.7: Illustration of the normalisation of the magnetisation vector at the end of a time step. Even though $\mathbf{v}$ is sought in the tangent plane, a normalisation is still required.

In a system dominated by the exchange interaction, the renormalisation of the mag-

netisation vector tends to decrease the energy according to Bartel's theorem.

$$\int A_{ex} \left|\nabla m^{n+1}\right|^2 \leq \int A_{ex} \left|\nabla m^{n,1}\right|^2 \tag{1.147}$$

The θ-scheme

To stabilise the numerical scheme, a θ-scheme has been implemented in feeLLGood. It consists in estimating the magnetisation at time $t = (n+\theta)k$ in equation 1.144.

Writing the effective field $\mathbf{H_{eff}}$ as the sum of the exchange field $A_{ex}\Delta\mathbf{m}$ and the contribution of all the other fields $\mathbf{H_r}$, the equation 1.145 becomes

$$\alpha(\mathbf{v},\mathbf{w}) + (\mathbf{m}^n \times \mathbf{v}, \mathbf{w}) = -\gamma_0 \frac{2A_{ex}}{\mu_0 M_s} (\nabla \mathbf{m}^n, \nabla \mathbf{w}) + \gamma_0 (\mathbf{H}_\mathbf{r}^n, \mathbf{w}) \tag{1.148}$$

This scheme is generalised by applying a θ-scheme for the Laplacian, which means that $\mathbf{m}^n$ is replaced with $\mathbf{m}^n + \theta\, k\mathbf{v}$ with $0 \leq \theta \leq 1$. The equation 1.148 becomes

$$\alpha(\mathbf{v},\mathbf{w}) + (\mathbf{m}^n \times \mathbf{v}, \mathbf{w}) + \theta k\gamma_0 \frac{2A_{ex}}{\mu_0 M_s} (\nabla \mathbf{v}, \nabla \mathbf{w}) = -\gamma_0 \frac{2A_{ex}}{\mu_0 M_s} (\nabla \mathbf{m}^n, \nabla \mathbf{w}) + \gamma_0 (\mathbf{H}_\mathbf{r}^n, \mathbf{w}) \tag{1.149}$$

Considering only the exchange field, it was proved [8] that the time scheme is unconditionally stable if $\theta \geq 1/2$. If $\theta < 1/2$, the stability depends on the length of the time steps. Indeed, Bartel's theorem [80] leads to an energy decrease:

$$E(n+1) \leq E(n). \tag{1.150}$$

The stability was also proved [81] including the other fields (namely, demagnetising field, anisotropy field and external field).

Towards a second-order time scheme

It would be interesting to obtain a higher-order time scheme allowing the same accuracy with larger time steps. Such a scheme may reduce substantially the simulation time. In fact, it is possible to have a higher-order scheme if the θ-scheme is applied to the whole right-hand side of equation 1.148 and not only to the Laplacian term. In the new time scheme, the weak formulation is expressed as

$$\begin{aligned}\alpha(\mathbf{v},\mathbf{w}) + (\mathbf{m}^n \times \mathbf{v}, \mathbf{w}) + \theta k\gamma_0 \frac{2A_{ex}}{\mu_0 M_s} (\nabla \mathbf{v}, \nabla \mathbf{w}) = &-\gamma_0 \frac{2A_{ex}}{\mu_0 M_s} (\nabla \mathbf{m}^n, \nabla \mathbf{w}) + \gamma_0 (\mathbf{H}_\mathbf{r}^n, \mathbf{w}) \\ &+ \theta k\gamma_0 (\partial_\mathbf{m} \mathbf{H_r}(\mathbf{v}), \mathbf{w}) \\ &+ \theta k\gamma_0 \left(\left[\frac{2A_{ex}}{\mu_0 M_s} |\nabla \mathbf{m}^{n+s}|^2 - \mathbf{H}_\mathbf{r}^n \cdot \mathbf{m}^n \right] \mathbf{v}, \mathbf{w} \right)\end{aligned} \tag{1.151}$$

The solution $\mathbf{v}$ is

$$\mathbf{v} = \partial_t \mathbf{m} + \theta k P(\partial_{tt} \mathbf{m}) + \mathcal{O}(k^2) \tag{1.152}$$

where P denotes the tangential part, that is the projection onto K^n. An important idea at this point is that for all $\mathbf{v} \in K^n$,

$$\frac{\mathbf{m} + k\mathbf{v}}{|\mathbf{m} + k\mathbf{v}|} = \mathbf{m} + k\mathbf{v} - \frac{k^2}{2}|\mathbf{v}|^2\mathbf{m} + \mathcal{O}(k^3) \tag{1.153}$$

so that normalisation, up to order 2, does not change the tangential part. m^{n+1} is defined as in equation 1.146. In virtue of equations 1.152 and 1.153,

$$P(\mathbf{m}^{n+1}) = k\mathbf{v} + \mathcal{O}(k^3) \tag{1.154}$$

$$= P(\mathbf{m} + \partial_t \mathbf{m} + \theta k^2 \partial_{tt} \mathbf{m}) + \mathcal{O}(k^3). \tag{1.155}$$

If θ is larger than $1/2$, then both sides of the equation are equal in norm up to the order 2. Therefore, $\mathbf{m}^{n+1}$ is the desired second-order approximation.

The stability can be proved similarly to the order 1. Moreover, if $s = 1$ in equation 1.151, then unconditional stability is obtained, but a unique solution cannot be guaranteed. Fig 1.8 illustrates the influence of the s parameter on the relaxation process in a ferromagnetic cube. A sinusoidal profile spreading over the cube's width was chosen as initial magnetization state. One can see that $s = 1$ is more dissipative.

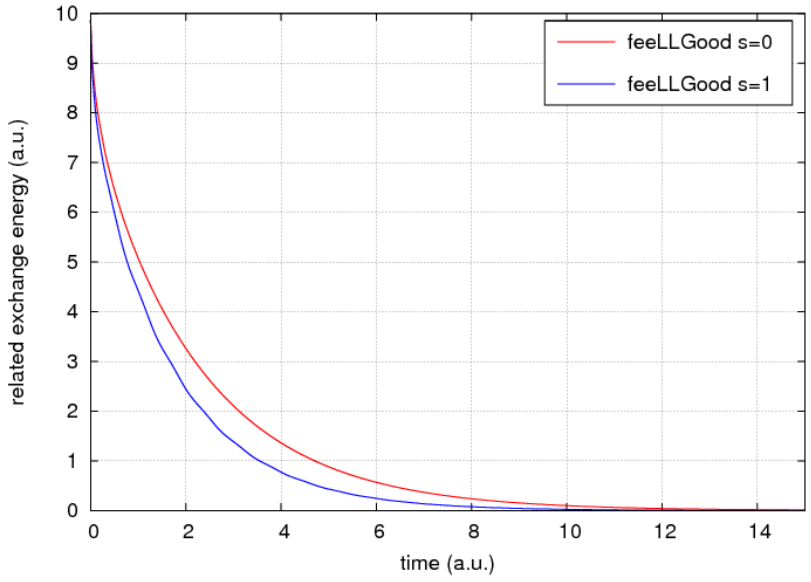

Figure 1.8: Evolution of exchange energy in a ferromagnetic cube. The harmonic flow equation was integrated with both $s = 0$ and $s = 1$, with time step fixed at $\gamma_0 \Delta t = 5 \times 10^{-3}$.

Demagnetising field computation: Non-uniform Fast Fourier Transform (NFFT)

The computation speed of the demagnetising field is the bottleneck of FEM-based micromagnetic simulations. In the FDM, the Fast Fourier Transform can be used for an efficient computation, which is not possible in the FEM because the nodes are not placed on a regular grid. feeLLGood user can choose between two numerical methods for the magnetostatic field computation: the Non-uniform Fast Fourier Transform (NFFT) and the FMM (Fast Multipole Method). NFFT will be explained in this section.

As mentioned previously, the magnetostatic field is the gradient of the magnetic potential ϕ whose the expression is given by the integral 1.61. This integral has to be calculated numerically and therefore becomes a discrete sum:

$$\phi(\mathbf{r}) = \sum_{i=0}^{S} \rho_i G(\mathbf{r}, \mathbf{r}_i) \tag{1.156}$$

where $\mathbf{r}_i$ is the position of the source, $G(\mathbf{r}, \mathbf{r}_i)$ is the Green's function, ρ_i is the density of magnetic charges and S is the number sources (a fixed number per element). S being proportional to the number of mesh nodes N, the direct summation 1.156 has a cost $\mathcal{O}(N^2)$. The NFFT algorithm implemented in feeLLGood allows faster computation of the magnetic potential.

NFFT uses a Fourier expansion of the Green's function with coefficients G_κ.

$$\phi(\mathbf{r}_j) = \sum_{i=0}^{M} \rho_i \left(\sum_{\kappa} G_\kappa e^{i\kappa(\mathbf{r}_j - \mathbf{r}_i)} \right) \tag{1.157}$$

$$= \sum_{\kappa} G_\kappa \left(\sum_{i=0}^{M} \rho_i e^{-i\kappa \mathbf{r}_i} \right) \tag{1.158}$$

where κ is the index of the modes in the Fourier expansion. The number of modes must be proportional to the mesh size. The regular FFT cannot be used for sums of the type $\sum f_j e^{i\kappa r_j}$ when the (r_j) are not on a grid. The idea of the NFFT [82, 83] is to diffuse, by Gaussian convolution, the data onto a grid, where the FFT can be applied. Deconvolution is then done in the frequency domain. Since the Gaussian function is localized, the convolution has a linear cost; likewise the deconvolution, which is a mere division of Fourier coefficients. Thus, the NFFT has the same overall cost as the FFT: $\mathcal{O}(N \log N)$.

Demagnetising field computation: Fast Multipole method (FMM)

In multipole methods, neighbouring sources are grouped into a cluster. Cluster contributions are evaluated at each target as multipole expansions. When the system is hierarchically divided into log N levels, each source contributes to log N parent clusters and $\mathcal{O}(\log N)$ clusters are evaluated at each target. The overall cost of $\mathcal{O}(N \log N)$ can be reduced to $\mathcal{O}(N)$ if information transits between clusters by expansion translation

[84, 85]. However, a $\mathcal{O}(N \log N)$ algorithm can be faster than $\mathcal{O}(N)$ on practical sizes if the prefactor is smaller.

The Halbach sphere: a test-case for demagnetising field computation

The Halbach sphere is a hollow sphere with an inner radius R_1 and an outer radius $R_2 = 2R_1$, with a magnetisation distribution $\mathbf{m} = \cos\theta\,\mathbf{e}_r + \sin\theta\,\mathbf{e}_\theta$ in polar coordinates. In a cross-section, the magnetization rotates twice as fast as the polar angle, as illustrated on figure 1.9. The Halbach sphere was chosen as a test-case for magnetostatic computation since there are both volume and surface charges and an analytical expression of the demagnetising energy is known:

$$E_d = \frac{2\pi}{27}\left(\frac{17}{3}(R_2^3 - R_1^3) - 8R_1^3 \log\frac{R_2}{R_1}\right)\mu_0 M_s^2. \tag{1.159}$$

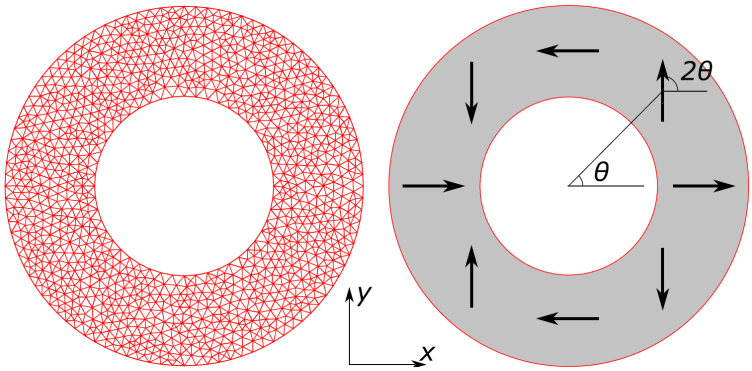

Figure 1.9: *Extracted from ref. [83].* Cross-section of the Halbach sphere. Left-hand side: Finite Element mesh. Right-hand side: magnetisation distribution.

We compared feeLLGood's fast summation methods with the Nmag solver, using the same meshes. Computations were performed on an Intel 2.2 GHz server with 32 GB RAM. Multipole expansions are cut off at nine terms.

The Nmag code uses a coupled Finite Element/Boundary Element Method (FEM/BEM) to solve the Poisson equation, which typically requires $\mathcal{O}(N^{4/3})$ time. The difference in performance between such a polynomial algorithm and feeLLGood's quasilinear ones is illustrated on fig. 1.10. The speed-up factor of NFFT over other methods is 5 on a 7×10^4-node mesh, while accuracy is similar.

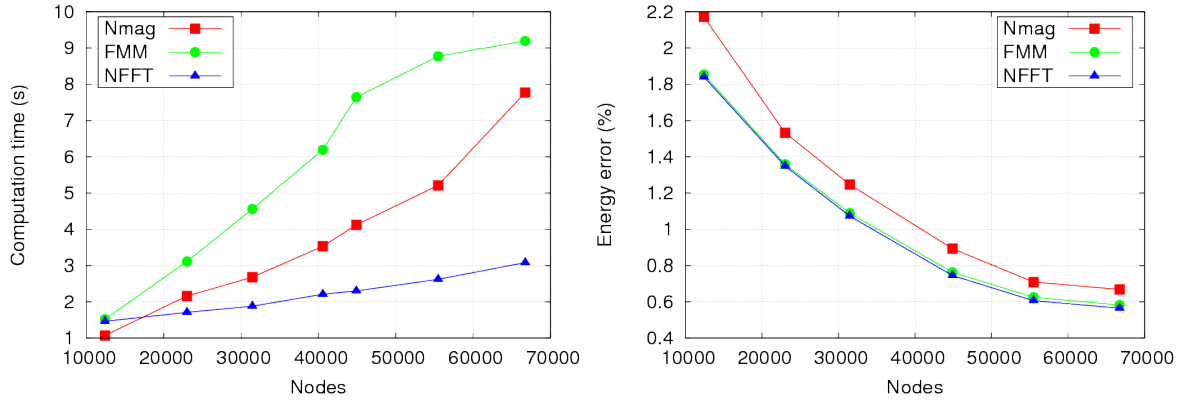

Figure 1.10: *Extracted from ref. [86].* Performance comparison of three algorithms computing the demagnetising field on the Halbach sphere problem: Nmag that uses the FEM/BEM method, feeLLGood using the Fast Multipole Method, and feeLLGood using the Non-uniform Fast Fourier Transform. Left-hand side: computation time as a function of the number of nodes. Right-hand side: energy error ($100 \times \frac{|E_{d,\text{simulation}} - E_{d,\text{analytical}}|}{|E_{d,\text{analytical}}|}$) as a function of the number of nodes.

1.3.3 NIST standard problem No. 4

The micromagnetic modelling group at the National Institute of Standards and Technology (NIST) proposes four standard micromagnetic problems. The goal is to compare the solution provided by different micromagnetic solvers. Results are displayed on the webpage [87] of the NIST group. The fourth standard problem is the only one focusing on dynamics. It consists in solving the dynamical response of a rectangular thin film platelet subjected to a field step along a given direction. The system's lateral dimensions are 500×125 nm and the thickness is 3 nm. The material parameters are chosen similar to Permalloy: $\alpha = 0.02$, $A_{\text{ex}} = 1.3\ 10^{-11}$ J/m, $M_s = 8\ 10^5$ A/m, $K_u = 0$ J/m^3. The exchange length is $l_{\text{ex}} = \sqrt{2A_{\text{ex}}/\mu_0 M_s^2} \approx 6$ nm; therefore, the magnetization is almost constant along (Oz).

The initial state of the dynamical computation is an equilibrium S-state along (Ox), obtained by applying an external field along the [111] direction and reducing its magnitude from 2 T to zero, by 0.02 T steps. Starting from the remanent state, the problem is divided in two sub-problems, corresponding to the response to two uniform field steps:

1. $\mu_0 H_x = -24.6$ mT, $\mu_0 H_y = 4.3$ mT, $\mu_0 H_z = 0.0$ mT *(which is a field approximately 25 mT, directed 170 degrees counterclockwise from the positive x-axis).*

2. $\mu_0 H_x = -35.5$ mT, $\mu_0 H_y = -6.3$ mT, $\mu_0 H_z = 0.0$ mT *(which is a field approximately 36 mT, directed 190 degrees counterclockwise from the positive x-axis).*

It turns out that the comments in brackets, which are written on the website, are misleading. Simulations performed with both FDM and FEM showed that the response is substantially different depending on which condition is applied. An approximation closer

to usable for the field direction is 170.085 degrees in the first case and 190.063 degrees in the second case. Figure 1.11 shows the results obtained with the finite difference solver micro3D in the sub-problem 2 for the two wordings. The system is in fact very sensitive to the angle of the field.

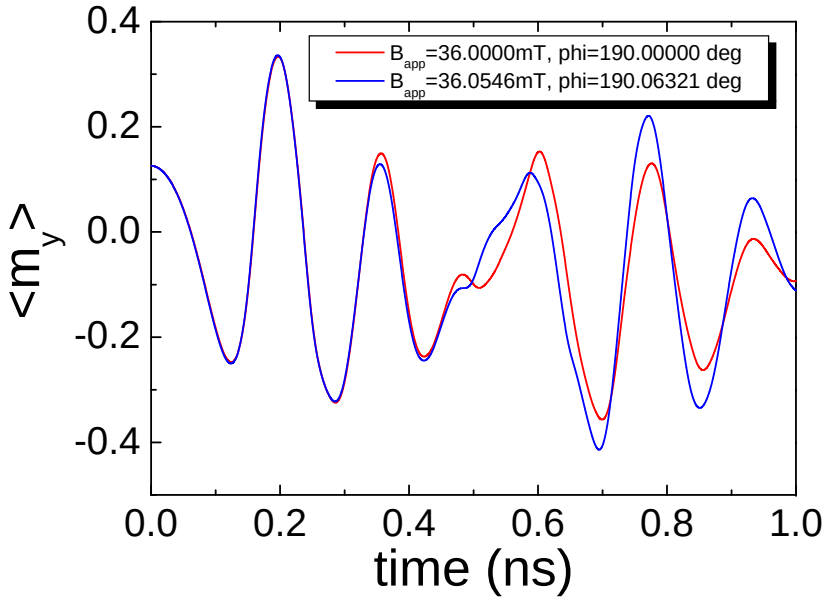

Figure 1.11: Results of micro3D, a Finite Difference micromagnetic solver developed in our group. $\langle m_y \rangle$ is plotted as a function of time. Red curve: subproblem 2 with wording given in terms of amplitude and angle. Blue curve: subproblem 2 with wording in Cartesian coordinates. The dynamics is very sensitive to the angle of the applied field.

In both sub-problems, the magnetization rotates towards the direction of the applied field. In the first sub-problem, the rotation is faster at the ends than in the centre of the platelet, but is in the same direction (counterclockwise). No compressed domain walls are created, and then no localized magnetic charges. Therefore, a coarse approximation is sufficient to estimate the demagnetizing field. In the second sub-problem, the magnetization rotates in opposite directions at the ends and in the centre, leading to the formation of compressed 360° domain walls. The reversal is achieved with the relaxation of these. Here we focus on this more critical numerical test. The field is $\mu_0 H_x = -35.5$ mT, $\mu_0 H_y = -6.3$ mT, $\mu_0 H_z = 0.0$ mT.

The simulations were performed on tetrahedral meshes with in-plane size $h = 2.5$ nm $< l_{\text{ex}}$. A double-layer mesh is necessary to reproduce magnetostatic field variations along the thickness, since the field is derived from a linear interpolation of the scalar potential. As seen in fig. 1.12, the dynamics computed by feeLLGood matches well that of Nmag using exactly the same mesh. Moreover, feeLLGood-FMM and feeLLGood-NFFT give almost identical results. Figure 1.13 shows that the dynamics is dissipative, as expected.

An adaptive time step is used in both Nmag and feeLLGood. The above results were obtained with the default Nmag tolerance parameter (10^{-6}), while feeLLGood controls the magnetization variation per iteration, which was bounded by $du_{\max} =$

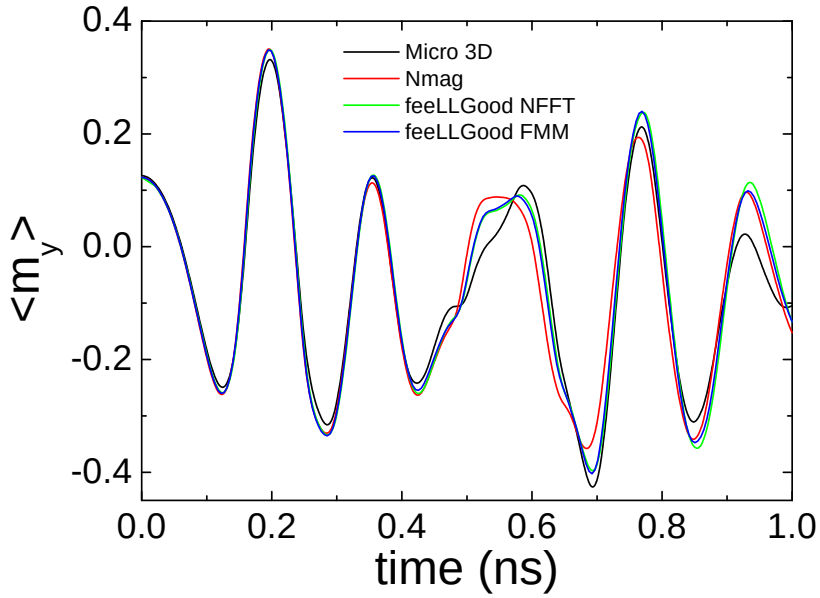

Figure 1.12: Comparison of three micromagnetic solvers on the NIST standard problem No. 4.

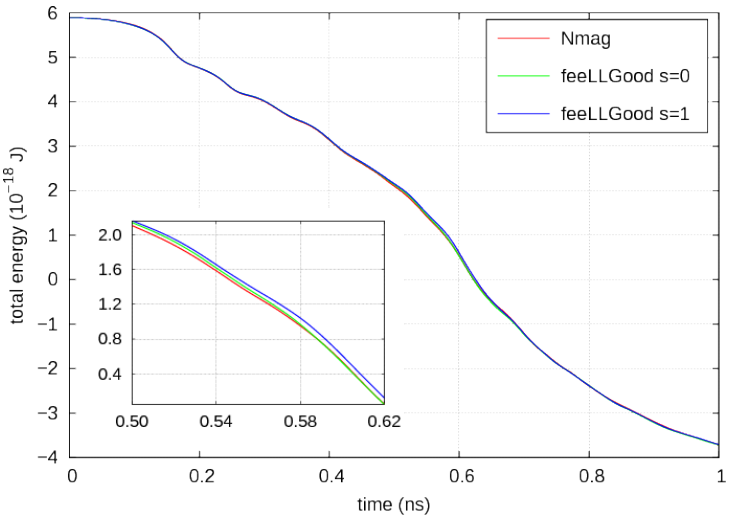

Figure 1.13: *Extracted from ref. [86].* Total energy as a function of time. Decreasing of the energy is verified for the three numerical methods.

$\max\left(\left|\mathbf{m}^{n+1}-\mathbf{m}^{n}\right|\right) = 0.01$. The dynamics computed for other values of $du_{\max}$ (with $s = 0$) are seen in fig. 1.14. The criterion $du_{\max} = 0.01$ is close to convergence. Large values tend to filter out high frequencies as the integrator cannot reproduce fast variations (see the rebound appearing at $t = 0.48$ ns for $du_{\max} = 0.1$). In addition, a shift toward low frequencies can be observed.

Fig. 1.15 shows the magnetization distribution computed by feeLLGood at selected times: when the average x-component vanishes (a), or when the exchange energy is maximal (b,c,d). These maxima correspond to the expulsion of narrow domain walls. Although the mesh is unstructured, centro-symmetry from the initial S-state is conserved

with an error as low as 2% after 1 ns, as expected by the LLG equation. This reflects the reliability of the feeLLGood solver.

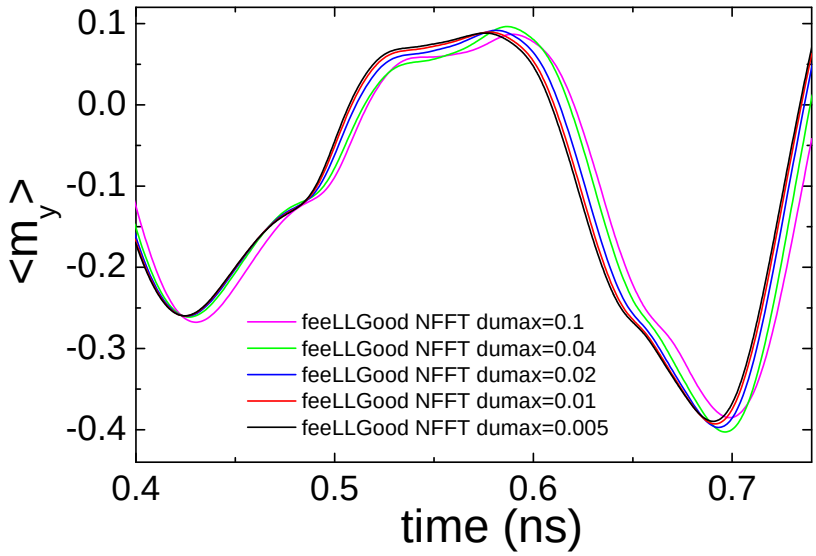

Figure 1.14: Zoom on the $\langle m_y \rangle$ curve for several $du_{\max}$ values. $du_{\max} = 0.01$ is close to convergence. These simulations were performed with feeLLGood order 2 and $s = 0$.

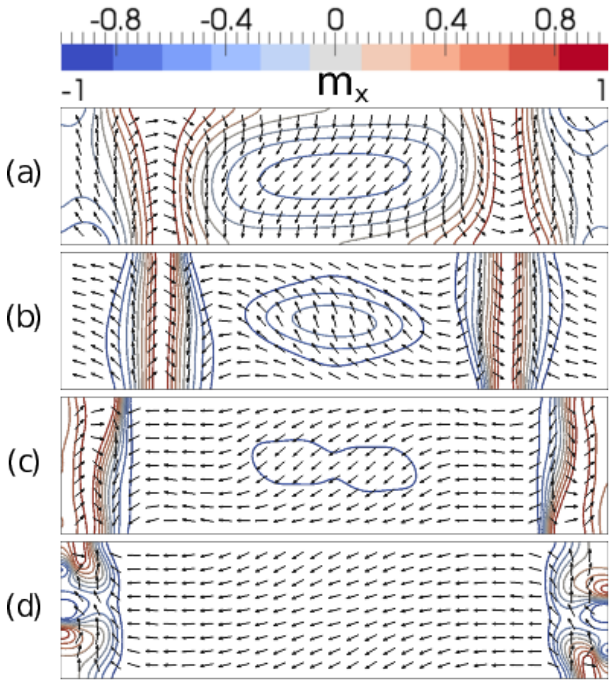

Figure 1.15: Micromagnetic configurations at times 0.135 ns, 0.218 ns, 0.446 ns and 0.548 ns. Contour lines of m_x exhibit a conservation of the centro-symmetry.

1.4 Conclusions of the chapter

In this chapter, the main physical concepts have been introduced. The LLG equation has been derived and a detailed description of the effective field has been given. Finally, the two numerical methods utilised in micromagnetism, FEM and FDM, have been presented together with the two micromagnetic software used during this PhD: ST_GL-FFT and feeLLGood.

In the following chapters, the aim is two-fold: testing feeLLGood in presence of spin torque, and understanding the dynamics of spintronic devices for applications.

Chapter 2

Planar Spin-Torque Oscillator

Contents

In this chapter, a spin torque oscillator is studied. The main goal is to understand the jumps in frequency observed in the experiment performed by Houssameddine *et al.* [1]. After a brief description of the macrospin dynamics for this type of system and a summary of Houssameddine's experiment, we will present earlier experimental and numerical observations of frequency jumps in similar systems. Then, the results of feeLLGood simulations will be reported and thoroughly analysed to explain the jumps.

2.1 Macrospin model

The system studied is illustrated on figure 2.1a. It is composed of a planar free layer and a planar polariser separated by a spacer (typically, Cu). Since the magnetisation of the polariser is fixed, the magnetisation dynamics is solved only for the free layer that is modelled as a macro-spin. The current traversing the free layer is polarised in the plane, with a sign convention defined on figure 2.1. A magnetic field is applied in-plane along the easy axis. The free layer magnetisation obeys the LLGS equation 1.106.

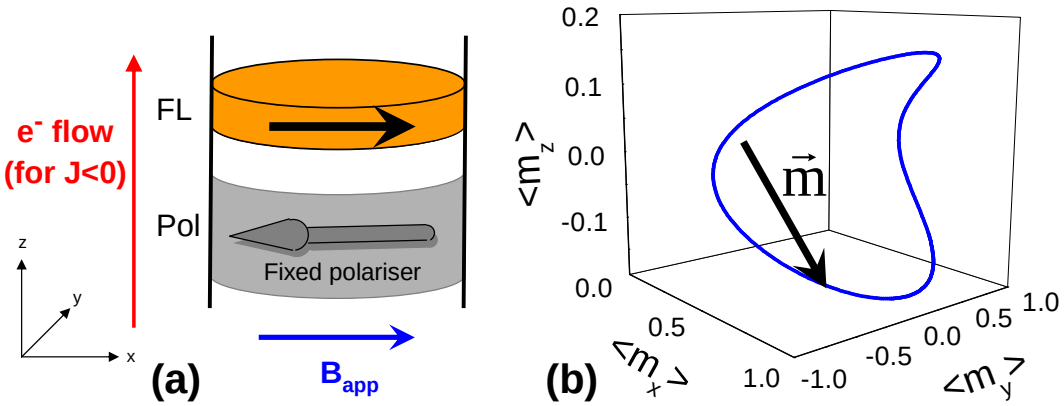

Figure 2.1: Left-hand side: planar spin torque oscillator. Right-hand side: magnetisation trajectory of an IPP.

The free layer has two equilibrium states: $m_x = +1$ and $m_x = -1$. Sun [88] shows a self-sustained oscillation appear when the current density J is above a critical current

$$J_{c1} = \alpha \frac{2e}{\hbar} \frac{\mu_0 M_s t}{g(\theta = \pi)} \left(H_K + H_{app} + \frac{M_s}{2} \right). \tag{2.1}$$

For $0 < J < J_{c1}$, any deviation is simply damped, going back to equilibrium. Above J_{c1}, the magnetisation oscillates periodically about the effective field (i.e. about the easy axis, in our case). This oscillation, called In-Plane Precession (IPP) is illustrated in figure 2.1b with the plot of the magnetisation trajectory. The IPP is very squeezed in the out-of-plane direction due to the shape anisotropy, but its in-plane incursion angle $\phi_{\max}$ can be very large.

In IPP, the spin torque and the damping torque are compensated in average over one period. The spin torque is therefore often considered as an "anti-damping" which is not true in the general case. Figure 2.2 shows the evolution of the IPP frequency and the maximum in-plane angle as a function of current. Interestingly, at J_c (onset of IPP), there is a vertical asymptote in the plot of $\phi_{\max}$, which means that the IPP amplitude grows very rapidly as soon as $J > J_{c1}$. Moreover, one can see that the frequency is maximum at J_{c1} and then decreases monotonically.

Figure 2.2 shows that there is a bifurcation at a current $J_{c2} > J_{c1}$. Above J_{c2}, the dynamics is more complicated with in particular the possibility to get out-of-plane

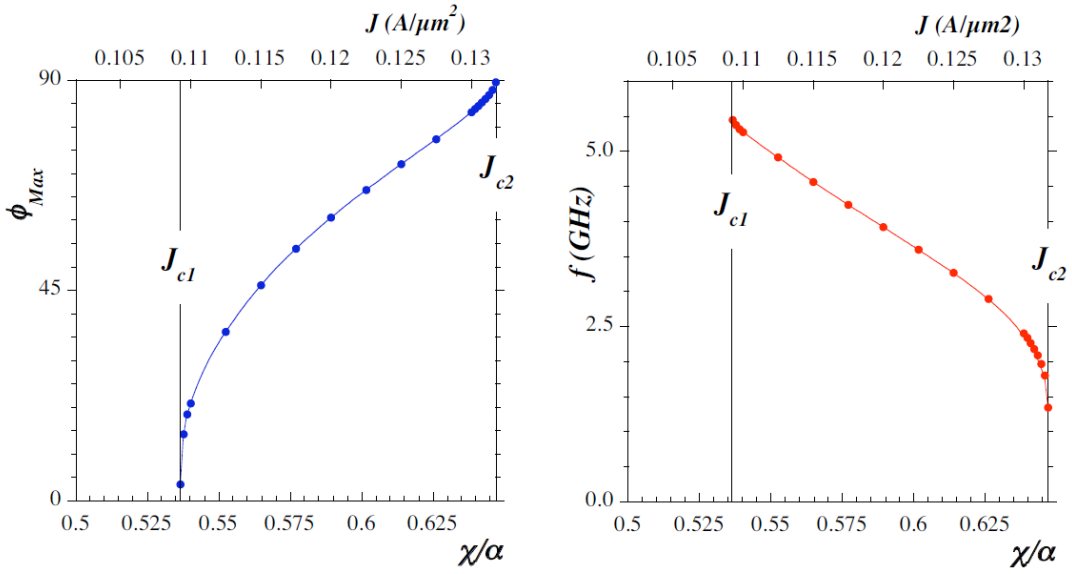

Figure 2.2: *Extracted from ref [89].* Left-hand side: maximum in-plane incursion angle as a function of normalised current. Right-hand side: frequency as a function of normalised current.

precessions, as shown in figure 2.3.

The state diagram is plotted on figure 2.3. This diagram was obtained with a convention for the current sign different from ours. Therefore, the x-axis has to be reversed to comply with our convention.

In the following, we will be interested in IPP, and particularly scans of current just above the critical current J_{c1}, corresponding to vertical lines inside the IPP region in the state diagram. The next section is dedicated to an experimental measurement of IPP oscillations.

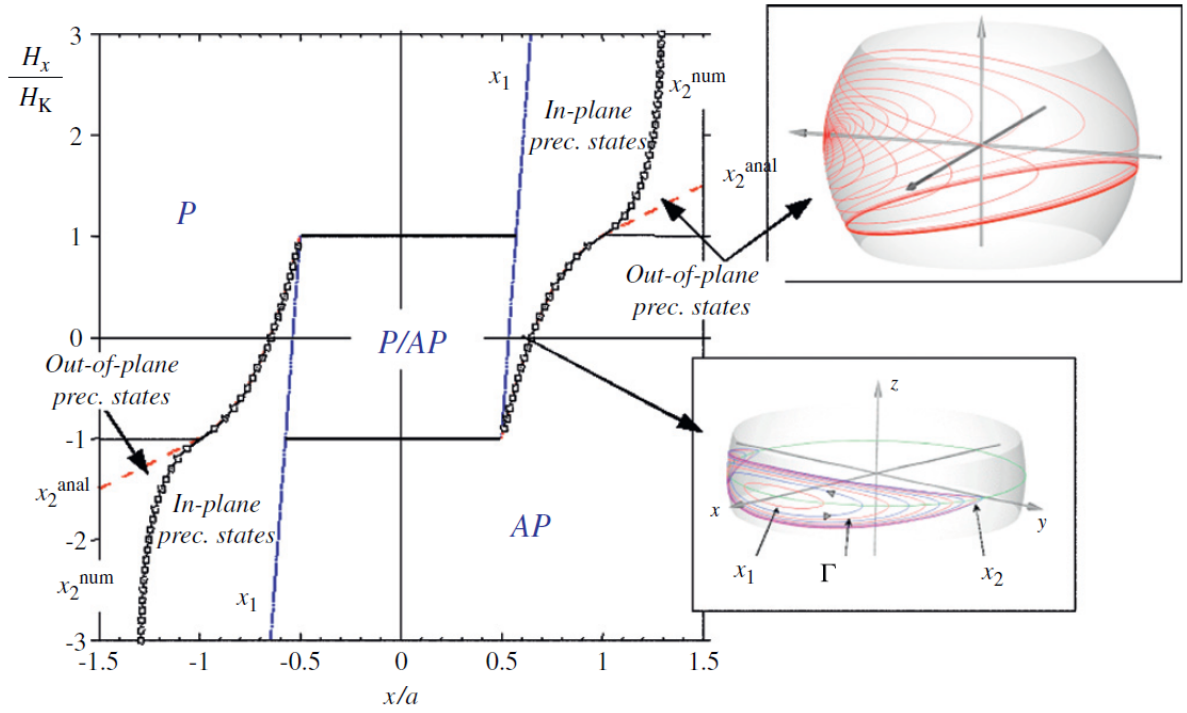

Figure 2.3: *Extracted from ref [90].* State diagram of magnetisation oscillations driven by an in-plane polarised current and an in-plane field; normalised field versus normalised current. The sign convention for the current is opposite to our convention.

2.2 An experimental observation of IPP: Houssameddine *et al.* [1]

In ref [1] by Houssameddine *et al.*, RF measurements performed in Spintec are reported. Frequency, linewidth and integrated power were studied in MgO magnetic tunnel junction nanopillars. The stack was composed of: Seedlayers / IrMn(6.1) / PL / MgO(0.9) / FL / Ru(6). The pinned layer (PL) was a CoFe(1.8) / Ru / CoFeB(2) SAF trilayer, while the free layer (FL) was a CoFe(0.5) / CoFeB(3.4) bilayer. The resistance and the Tunnel Magnetoresistance (TMR) of the devices were measured. Although they were all fabricated on the same wafer, they fall into two distinct categories: HTMR samples with high resistance and high TMR ($\approx 100\%$), and LTMR samples with low resistance and low TMR ($\approx 30\%$). The lower performance of LTMR devices is believed to be caused by defects in the tunnel barrier. The nanopillars were either circular with 80 nm diameter or elliptical with a lateral size of $65 \times 130\,\mathrm{nm}^2$.

Below a threshold current, the samples exhibit oscillations typical to ferromagnetic resonance. Such an oscillatory behaviour is induced by thermal fluctuations and is called *thermally excited FMR*. Above the critical current, steady state in-plane precessions of the free layer are observed.

Henceforth, the results on the circular samples will be described, the elliptical nanopillars having a similar behaviour. The RF characteristics of LTMR and HTMR devices

are very distinct. The linewidth of LTMR devices can be as low as 10 MHz whereas the linewidth of HTMR samples is larger than 100 MHz. The plots of the frequency and the linewidth as a function of field are shown in figure 2.4 for both types of sample at current greater than the critical current.

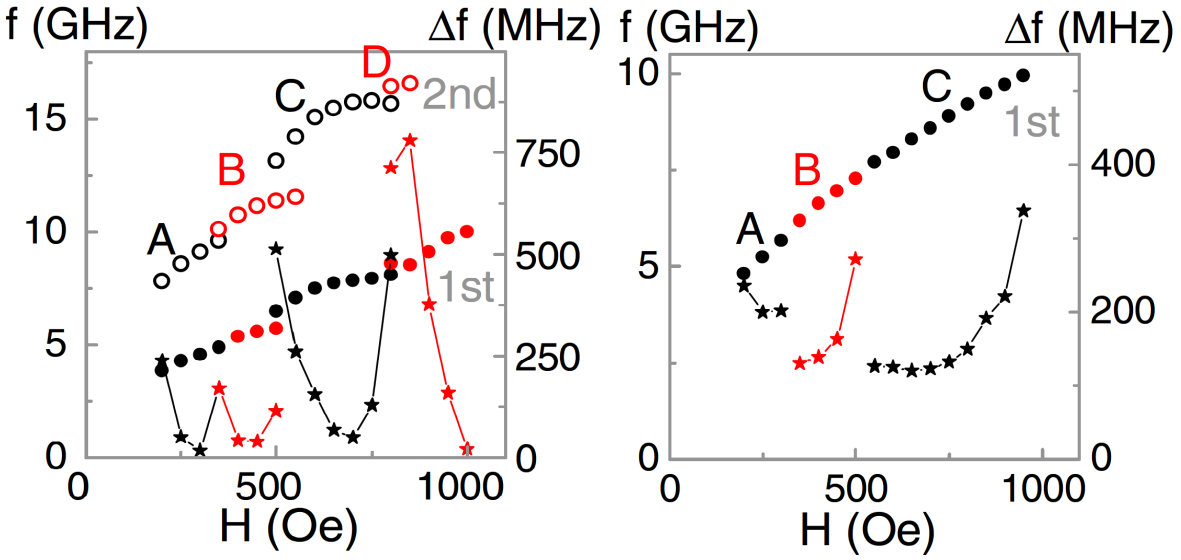

Figure 2.4: *Extracted from ref [1].* Measures of an LTMR sample (left-hand side) and an HTMR sample (right-hand side). Full circles: frequency of the first harmonic. Empty circles: frequency of the second harmonic. Stars: linewidth Δf.

Frequency increases with field, like in the Kittel mode. The most striking feature of these plots is the existence of several "branches". For LTMR sample, the frequency changes abruptly at several field values. This is particularly visible on the second harmonic. Moreover, these frequency jumps are correlated with linewidth maxima. The large linewidth value at the frequency discontinuities is likely due to the presence of two peaks in the Fourier spectrum that blend together. On the plot corresponding to an HTMR sample, the frequency discontinuities do not appear so clearly. However, the large increase of linewidth at some field values is evidence of a similar underlying behaviour.

The correlation between linewidth and frequency jumps shows that the origin of the different branches has to be understood to control the coherence of STOs. Reducing the linewidth is necessary for applications and therefore the frequency jumps have to be avoided. The rest of this chapter will be mainly dedicated to the study of these jumps.

Other experiments have measured frequency jumps of IPP oscillations. The next section is dedicated to a review of theses studies.

2.3 Frequency jumps in earlier experimental studies

Kiselev *et al.* [91] observed spin-torque induced magnetisation precession in a spin-valve with out-of-plane external magnetic field. They measured frequency jumps when the current is varied. Macrospin simulations provide a good qualitative explanation of these results, showing that a frequency jump corresponds to a change in the direction of the precession axis.

Rippard *et al.* [92] have reported on frequency discontinuities in point-contact geometries. In a point-contact spin valve, the free layer is not a patterned but is instead a continuous film. In Rippard's experiment, the angle of the external field is varied from in-plane to out-of plane. At intermediate angles, a very complex dynamics is observed with current-dependent frequency jumps. Near the jumps, two branches exist at the same current and field. This is not a hysteretic behaviour but rather the coexistence of two peaks in the spectral output of the device. It can be attributed to mode hopping between two trajectories with different oscillation frequencies.

Muduli *et al.* [93] have reported on experimental observation of frequency hopping in MTJ-based spin-torque oscillators. Measured samples are circular nanopillars of 240 nm diameter with a CoFeB free layer of 3.5 nm. The reference layer is planar, like the free layer. An external field is applied in-plane, and it angle is varied. Time traces of the voltage signal are collected at different angles and currents, then the frequency is analysed. Frequency jumps occurring in time are found, confirmed by micromagnetic simulations at $T = 300\,K$. An optimal angle and optimal angle of applied field are deduced.

An experimental observation of frequency jumps in STO was reported in 2005 by Krivorotov *et al.* [94]. Spin-transfer driven excitations were measured in a nanopillar of elliptical cross-section 130 nm × 60 nm, consisting of two 4 nm-thick permalloy layers separated by an 8nm-thick Cu layer. The angle between the equilibrium magnetisation of the two ferromagnetic layers was about 30°. A plot of the frequency versus voltage (fig 1D in ref [94]) shows clearly two abrupt changes of the frequency. However, according to this graph, the frequency was not discontinuous. These experimental data reveal a complex underlying dynamics that is not explained by macrospin simulations. Micromagnetic simulations are necessary, as shown in the section 2.4.2.

Before showing the results of our simulations, it is interesting to take a look at previous numerical studies of frequency jumps. The next section is dedicated to these previous simulation works.

2.4 Frequency jumps in earlier numerical studies

2.4.1 Macrospin simulations

In ref. [95], macrospin simulations of coupled ferromagnetic layers are performed. The simulated system, illustrated in figure 2.5a, is a spin valve comprising a planar Synthetic Anti-Ferromagnet (SAF) [1] polariser and a planar free layer (FL). The LLG equation is solved numerically for the three ferromagnetic layers. The top and bottom layers of the SAF are linked only by RKKY interaction [2].

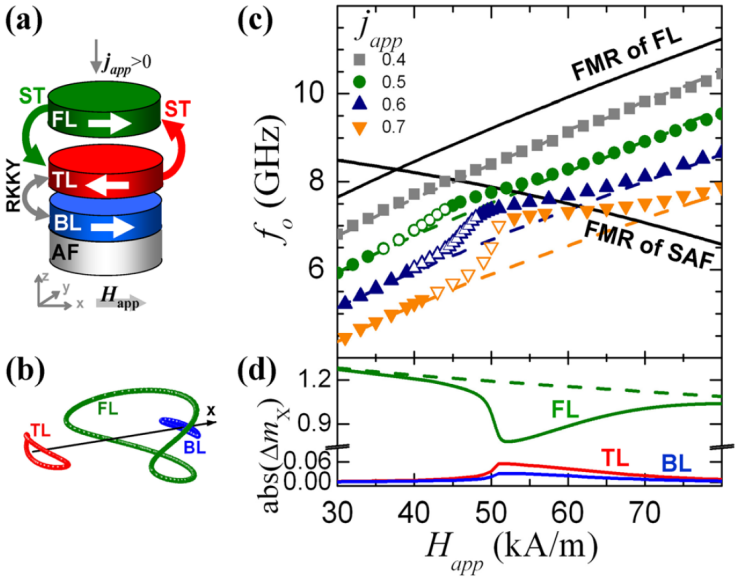

Figure 2.5: *Extracted from 2.5.* (a) Simulated system. (b) Magnetisation trajectories. (c) Frequency vs field. (d) m_x amplitude vs field.

Firstly, the FMR frequencies of the uncoupled FL and SAF are calculated (the STT, indicated by red and green arrows on 2.5a, is ignored). Frequency f_0 versus applied field H_{app} is plotted in black on the figure 2.5. H_{app} being in the same direction as the FL magnetisation, the FL frequency increases when H_{app} increases. In contrast, the SAF excitation is dominated by the oscillation of the top layer because the bottom layer is pinned by an anti-ferromagnet. The field being applied opposite to the top layer magnetisation, the FMR frequency decreases with H_{app}. Crossing between the two frequencies occurs at 37 kA/m.

Secondly, the spin torque is added on the free layer. The spin polarisation of the current is given by the direction of the top layer magnetisation (red arrow in figure 2.5a). Dashed lines in figure 2.5c represent the FL frequency obtained for these simulations. The frequency decreases with current. The curvature of the frequency line remains almost the same as the current is increased.

[1] For more details about SAF, see the second paragraph of section 4.2.1.
[2] For more details about RKKY coupling, see the second paragraph of section 4.2.1.

Finally, the spin torque caused by the FL is added on the top layer (green arrow in figure 2.5a), considering thus a mutual spin transfer interaction between the two layers. Oscillations of the top layer magnetisation are then generated and transmitted to the bottom layer via the RKKY interaction. Free and bottom layers act then as two coupled oscillators while the bottom layer is a resonator. The three layers oscillate at the same frequency. Their typical clam-shell trajectories are plotted in figure 2.5b. The bottom layer has the smallest amplitude due to the anti-ferromagnetic pinning. The most striking characteristic of this set of simulations compared to the previous one appears at large current. While the frequency curve is unchanged at low current, the mutual spin-torque affects dramatically the oscillation frequency at large current (figure 2.5c). A strong deviation occurs in the range of 50 to 60 kA/m. In fact, far from this range, the frequency is the self-frequency of the FL, which is, by far, the most excited. When the frequency of the system becomes close to the self-frequency of the SAF, the amplitude of top and bottom layers increases, while the FL amplitude decreases (figure 2.5d). This dynamic behaviour is characterised by a strong variation of the frequency (figure 2.5c). Even though the frequency varies smoothly in the simulations, an abrupt jump can be observed in the case of a conservative coupling between FL and top layer, as shown by Kudo *et al.* [96] in the case of dipolar interaction.

Including thermal fluctuations in the simulations, Gusakova *et al.* studied the linewidth. It was found to be slightly increased between 35 and 45 kA/m and greatly lowered between 45 kA/m and 65 kA/m (figure 2a of ref[95]). In the region of $35-45\,\mathrm{kA/m}$ the system is more sensitive to thermal fluctuations, while it is stiffer in $45-65\,\mathrm{kA/m}$ (which, in more technical terms, means a greater relaxation rate Γ_p).

The dynamics observed by Houssameddine *et al.* [1] is much more complex than the macrospin dynamics presented above because there are several frequency jumps, which cannot be explained in a simple macrospin model, hence the interest of micromagnetic simulations.

2.4.2 Micromagnetic simulations

The experiments by Houssameddine [1] (section 2.2) and by Krivorotov [94] (section 2.3) have a lot of common points: FL and PL are planar, out-of-plane precessions are measured, frequency jumps are observed, and these jumps cannot be explained by macrospin. Therefore, to understand the origin of the frequency discontinuities in Houssameddine's experiment, it is useful to review the earlier work simulating Krivorotov's experiment. These micromagnetic simulations were mainly performed by Montigny and Miltat [97], Berkov *et al.* [98, 90], and Finocchio *et al.* [99, 100].

Berkov *et al.* [98, 90]

In ref [98], results of a detailed micromagnetic study are presented to describe the experiment of Krivorotov *et al.* [94]. Simulations are performed with the FDM-based software MicroMagus [62]. The LLGS equation is solved for the free layer only. As

illustrated on the figure 2.6, the magnetisations of the pinned and the free layer are non-collinear. The external magnetic field is applied with an angle of 45° with respect to the long axis of the ellipse.

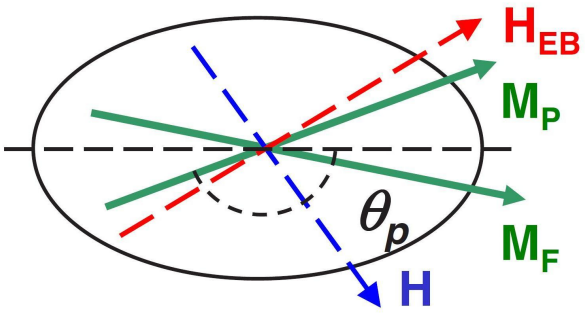

Figure 2.6: *Extracted from ref [98].* $\mathbf{H_{EB}}$: exchange bias field between the antiferromagnet and the polariser. $\mathbf{M_P}$: pinned layer magnetisation. $\mathbf{M_F}$: free layer equilibrium magnetisation. $\mathbf{H}$: applied field.

A "minimal model" is first considered whereby thermal fluctuations and Oersted field are neglected and the spin torque efficiency is supposed symmetric. The missing ingredients are then added one by one in order to study the influence of each one. All in all, the main characteristics of the plot of f vs I from ref [94] are reproduced with a fairly good agreement. At low current IPP are observed, while at larger current the minimal model leads to out-of plane precession, and the complete model leads to spatially incoherent magnetization dynamics. It is interesting to note that, similarly to the experiment by Houssameddine *et al.* [1], the linewidth increases when approaching a frequency jump. Thus both experiments (Krivorotov and Houssameddine) share a lot of similar characteristics. A spectral mapping technique (see section 2.6.4) is used to analyse the zones of the free layer which are the most excited. Even though theses maps are different for each branch, the fundamental reason of the frequency discontinuities remains unclear. One is not able to predict for which current values the jumps will occur. This issue is summarised in the article by:

> *Spatially resolved spectral analysis of our simulation data reveals that these jumps correspond to transitions between strongly non-linear oscillation modes [...]. With each frequency jump, the mode becomes more localized but the oscillation power is still concentrated in one single-connected spatial region which has no node lines. [...] An analytical theory of the nonlinear eigenmodes of a resonator having the correct shape would be required to achieve a thorough understanding of this phenomenon.*

Some of the results of this article are summarised in ref [90].

Finocchio *et al.* [99, 100]

The numerical study reported in [100] aims at simulating the experimental results published in [98]. The FL and the PL are both solved dynamically taking into account

the feedback effect of the spin torque from the FL on the PL. The field is applied with an angle of 45° with respect to the easy axis. Thermal fluctuations are not included. Two dynamical regimes are found depending on the amplitude of the current. At low current density, the oscillation is periodic, whereas at large current a more complex mode is found, and qualified as "chaotic". Although the main point of the article is the study of linear power and non-linear power, another fact is also of interest. Thanks to the wavelet scalogram method [101], the frequency is plotted as a function of time. Abrupt changes of the frequency are observed, arising from random domain-wall nucleation and propagation across the free layer. A similar study was published by the same group in the reference [99].

Montigny and Miltat [97]

In Montigny's PhD thesis [97], simulations of the Krivorotov's experiment are analysed in details. The results obtained with the "classical" FDM are presented and compared to the "improved" FDM (developed by Miltat) that performs an "edge correction" to smooth the staircase edge. However, it is not mentioned whether the edge correction is made for the dipolar field, for the exchange field, or for both. In fact, the "classical FDM" and the "edge-corrected FDM" give almost identical results, with frequency jumps occurring at the same current values. It proves that the origin of the jumps is not induced by the mesh roughness. Simulations at $\alpha = 0.01$ exhibit real frequency jumps. In comparison, frequency variations in the simulations at $\alpha = 0.025$ look more continuous. The Micromagnetic Spectral mapping Technique is also used by Montigny and Miltat. They find some differences with the maps obtained by Berkov, but this is likely due to the Oersted field which is ignored in Berkov's model. The FMR eigen-modes are calculated for the free layer and compared to the maps of the simulated IPP. Similarities are found, but the frequency jumps are not clearly related to hopping from one eigen-mode to another. One hypothesis is that the system locks on some FMR eigen-modes over a certain range of current. It is worth noting that other simulations were reported in the same PhD thesis where the applied field, the pinned layer and the FL equilibrium state were all aligned with the long axis of the ellipse. Such a system is comparable to the one measured by Houssameddine *et al.* [1]. However, here no frequency jump was observed in their simulations.

All the previous micromagnetic simulations that reported on jumps of IPP frequency were performed with the Finite Difference Method. As shown later, the interpretation of such simulations is delicate because of possible edge artefacts. However, applying a field at a certain angle with the easy axis may help to avoid edge effects which are intrinsic to FDM. We believe this might be one of the reasons why the external field is very often non-collinear to the easy axis in FDM simulations of IPP mode. In contrast, treating rounded shapes with the Finite Element Method is more reliable due to the better description of the edge. feeLLGood is therefore is the appropriate tool for this study.

2.5 Simulation results with feeLLGood

Macrospin and FDM simulations of Houssameddine's experiment [1] were simulated. As shown in figure 2.7, the macrospin approximation predicts a smooth variation of the frequency, whereas FDM simulations exhibit frequency jumps. Nevertheless, due to known edge effects of Finite Difference meshes (see section 3.2.3 in the next chapter), feeLLGood is the appropriate tool to simulate the system. One of the major motivation of this work is the applicative interest to understand the frequency jumps because of their link with the linewidth.

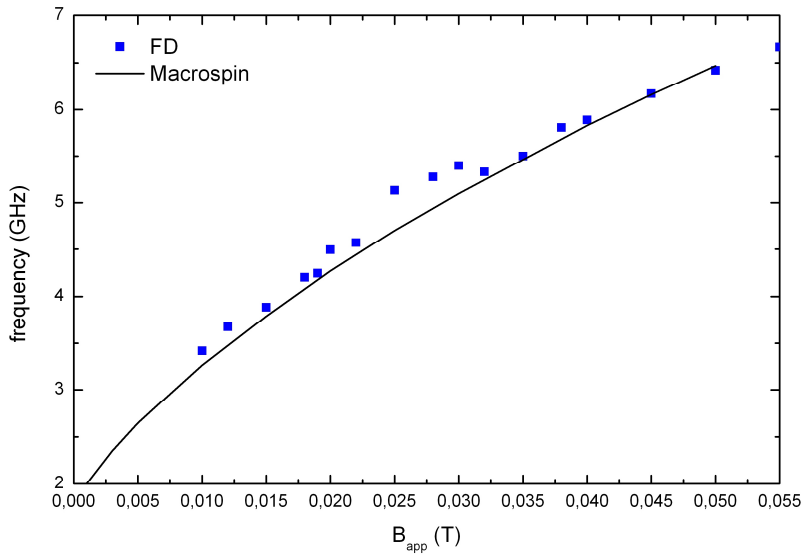

Figure 2.7: Frequency versus applied field for macrospin simulations (grey line) and Finite Difference simulations (blue squares) of In-Plane-Precession oscillations.

2.5.1 Frequency versus current and field

First, a few simulations were run with the version that is order 1 in time, and then they were checked with the order 2. A very good agreement was found, and therefore all the other simulations were run with the order 2. Each point on the curve requires, in average, a computation time of 8 days. A cluster of more than 100 CPUs was used, allowing to run a large number of simulations at the same time. The mean computation time was less than two weeks with a very strict criterion of precision ($du_{max} = 0.01$). The demagnetising field is computed with the FMM method.

The LLGS equation is solved for the FL, while the polariser is supposed fixed. There is no magnetocrystalline anisotropy ($K_u = 0$), but the slight ellipticity of the FL (90 nm $\times$ 80 nm) gives rise to a small shape anisotropy. Thus, at equilibrium, the FL magnetisation

lies along the long axis of the ellipse (x-axis). $\mathbf{p}$, the magnetisation of the PL, is pointing along $-\hat{\mathbf{x}}$. The simulations are started from a uniform in-plane state tilted by 5° with respect to the easy axis such that the spin torque is non-zero at initial time, and IPP can start. The applied field $\mathbf{H_{app}}$ is in-plane, directed along $+\hat{\mathbf{x}}$, such that the damping torque tends to return the magnetisation along its equilibrium direction $+\hat{\mathbf{x}}$. The spin torque is opposite (along $-\hat{\mathbf{x}}$), due to a negative current (electrons flowing from the pinned to the free layer). Steady oscillations arise then from the competition between the spin torque and the damping torque.

A_{ex}	2×10^{-11} J/m
$\mu_0 M_s$	1.2566 T
K_u	0 J/m^3
$\mathbf{p}$	[−1 0 0]
α	0.02
η	0.3
lateral size	90 nm × 80 nm
thickness	3.9 nm
mesh1	2846 nodes
mesh2	4930 nodes

Table 2.1: Input parameters of the FEM simulations.

Input parameters of FEM simulations are summarised in the table 2.1. Oersted field, thermal fluctuations and polariser's stray field are neglected. Moreover, the spin torque contains only the a_J term. b_J should be also included for a more realistic model of the MTJ measured in ref [1]. However, a basic model is always preferred in a first approach, more "ingredients" can still be added afterwards (but limited time did not allow to go further during this PhD). The extracted frequency is the frequency of $\langle m_y \rangle$, which is the precession frequency and is equal to twice the frequency of $\langle m_x \rangle$.

In the first simulations, the FL was discretised in a 2846-node mesh (14617 elements). The amplitude of the applied field was varied at fixed current values. Self-sustained IPP were found only above a certain threshold current ($J_c \approx -3.2 \times 10^{11}$A/m^2). Above J_c, the frequency decreases with current amplitude. This behaviour is also predicted by the macrospin model. Like in Houssameddine experiment [1], frequency jumps are observed, shown in figure 2.8a. Several "modes" appear, represented by different colours. Between these modes, the gaps become larger when the current is increased. Three or four modes are particularly distinct. At large field, the separation between the branches is not very clear due to a more complex dynamics. Indeed, some oscillations could not stabilise and therefore are not represented on the figure. One can also notice, around 27 mT, that the curve of $J = -4 \times 10^{11}$A/m^2 and $J = -5 \times 10^{11}$A/m^2 overlap. This type of non-linear effect is not explained by macrospin.

In fact, a mesh of 2846 nodes is a bit coarse for a CoFe/CoFeB free layer of 90 nm × 80 nm × 3.9 nm. Consequently, the same simulations were performed with a refined mesh of 4930 nodes (25588 elements) (see fig. 2.8b). The results are not only interesting for

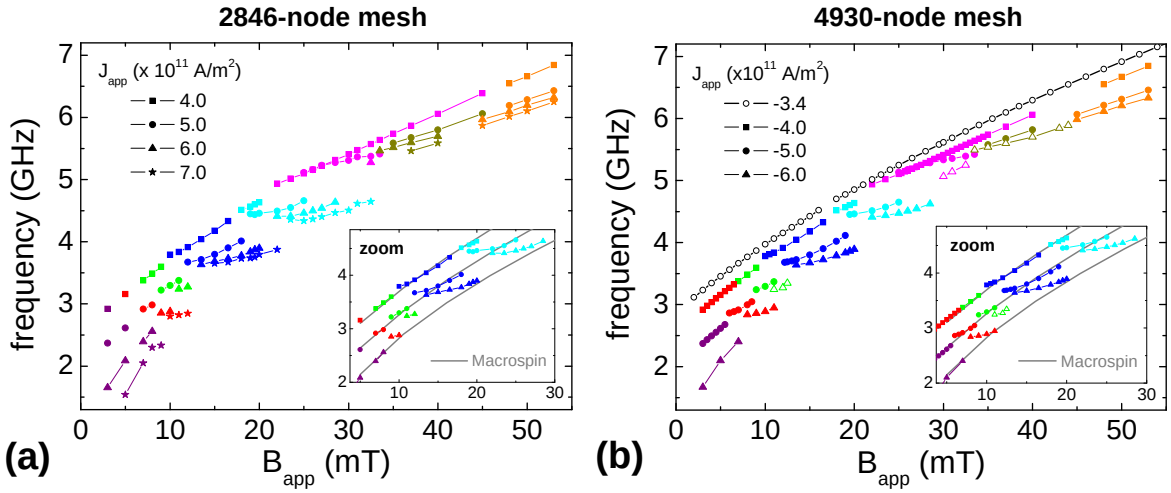

Figure 2.8: Frequency as a function of applied field. Simulations performed with a mesh of 2846 nodes (a) and a refined mesh of 4930 nodes (b). Insets in the two figures show as well macrospin curves for $J = -4 \times 10^{11}\mathrm{A/m}^2$, $J = -5 \times 10^{11}\mathrm{A/m}^2$ and $J = -6 \times 10^{11}\mathrm{A/m}^2$.

physics but also for numerics. The agreement between the two meshes is very good, with the same "modes" separated by the same "band gaps" at the same field values. However, some differences exist. The most striking difference is at $J = -7 \times 10^{11}\mathrm{A/m}^2$ where many simulations run with refined mesh could not stabilise. A large current leads more easily to a chaotic-like behaviour with a fine mesh. In fact, smaller elements allow spin waves of smaller wavelength to develop. These spin waves can disrupt the main precession mode and then lead to chaos. In contrast, a mesh with fewer elements will be less "stiff" and less sensitive to chaos.

A current value of $J = -3.4 \times 10^{11}\mathrm{A/m}^2$, just above the critical current, was simulated in the refined mesh. No obvious frequency jump appear on this curve. Therefore, it seems that the jumps are intrinsic to large-amplitude oscillations: the gap between two consecutive branches tends to zero when the critical current tends to the critical current. The curve found at $J = -3.4 \times 10^{11}\mathrm{A/m}^2$ is almost the Kittel mode (FMR mode), as shown later in the section 2.6.5.

When the field is varied, the energy landscape is modified. However, varying the current at a given field leaves the energy landscape unchanged. Consequently, it is maybe more intuitive to fix the field and vary the current in order to explore the energy landscape. Such series of simulations were also performed. The results are shown in the figure 2.9.

Similarly to the micromagnetic simulations of the Krivorotov experiment (section 2.4.2), downward frequency jumps are always observed. The jumps are smaller for smaller field values and for smaller current values, which is consistent with the previous plot. Like in the previous simulations, some oscillations at large current and large field did not stabilise and consequently do not appear on the figure. Interestingly, no obvious pattern appears in the series of frequency jumps, unlike the previous plot. Therefore, f versus H_{app} is a much better representation, which is more relevant to understand why

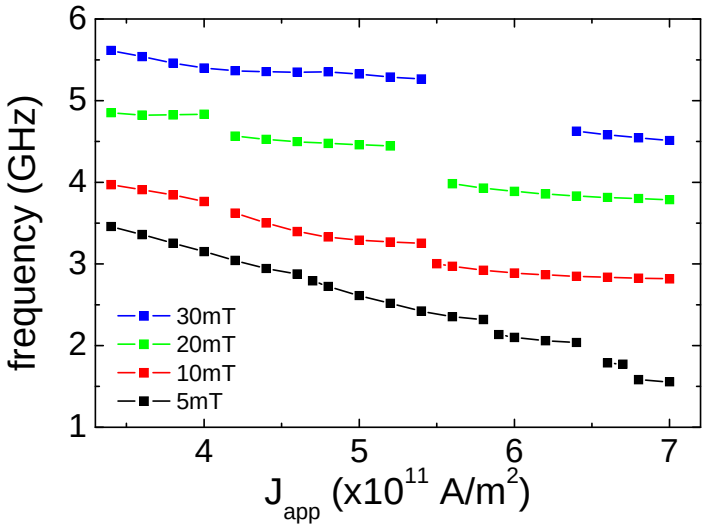

Figure 2.9: Frequency vs current density for various values of the applied magnetic field.

the frequency jumps occur at some particular field values. It would be very interesting to see the simulations of Berkov *et al.* and Montigny *et al.* plotted as f versus H_{app}. Similar "gaps" may also appear.

2.5.2 Critical current

IPPs exist above a threshold called "critical current", denoted J_c. According to the macrospin model, the critical current varies linearly with the applied field, following the equation 2.1. The curve obtained from this equation for the parameters of our simulation is plotted in the figure 2.10. The critical current varies very little, between $-4 \times 10^{11}\mathrm{A/m}^2$ and $-4.3 \times 10^{11}\mathrm{A/m}^2$ over the range of applied field.

The order 2 version of feeLLGood showed its first (and only) weakness at the test of critical current. Simulations are started with a uniform magnetisation tilted by 5° with respect to the easy axis. H_{app} and J are varied. If $\langle m_x \rangle$ vanishes to zero, then $J < J_c$; if the oscillation is stabilised, then $J > J_c$. Instead of finding a linear increase of J_c with H_{app}, a linear decrease was found as shown in figure 2.10. Such a variation is physically impossible because the critical current becomes negative above a certain field, which means that steady oscillations would be possible without current. In absence of thermal fluctuations, there should be no excitation at $J = 0$.

In fact, the simulations performed with the order 1 version of feeLLGood exhibit a much more consistent behaviour with an almost constant critical current of $J = -3.2 \times 10^{11}\mathrm{A/m}^2$ over the whole field range (figure 2.10). Further simulations have shown that the problem inherent to the order 2 version affects only the dynamics near the critical current. All the results presented in this chapter are therefore absolutely reliable.

The discrepancy between macrospin ($J_c \approx 4 \times 10^{11}\mathrm{A/m}^2$) and micromagnetic simulations ($J_c = 3.2 \times 10^{11}\mathrm{A/m}^2$) can be explained in the following way. Steady oscillations appear when the the spin torque overcome the damping torque around the equilibrium

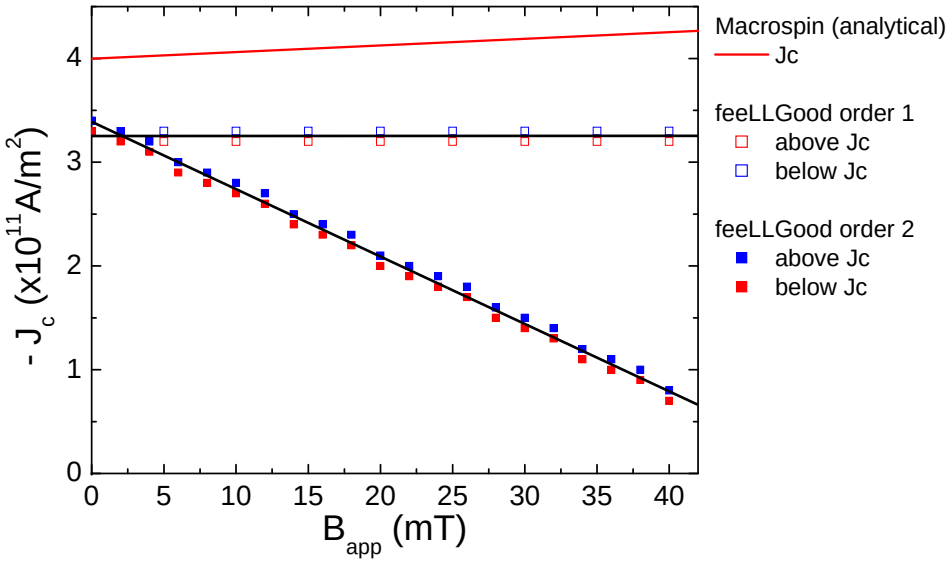

Figure 2.10: Critical current as a function of applied in-plane field. In red: macrospin calculations (formula 2.1). In black: feeLLGood simulation results for order 1 and order 2. The critical current given by the order 2 version is wrong at large fields.

state. The macrospin approximation consists in a kind of average of the magnetisation. Therefore, spin torque needs to overcome damping "in average" over the magnetic volume. In micromagnetic simulations, the spin torque can locally overcome the damping torque whereas both are not compensated in average. The local excitation is then transmitted to the rest of the FL via the exchange interaction, which leads to a critical current lower than in macrospin. A comparison could be drawn with magnetisation reversal by an external field: the coercive field predicted by macrospin is larger than the coercive field predicted by micromagnetism due to local excitations that are transferred to the whole sample.

2.5.3 The "quasi-periodic regime": towards a chaotic motion

Simulations plotted in figure 2.8 b are not all perfectly periodic. In fact, the full symbols in fig.2.8 b represent periodic stabilised oscillations whereas the hollow triangles correspond to non-periodic oscillations. These oscillations appear at large current. The non-periodic oscillations found with the 2846-node mesh are not shown, but some were found at $J = -7 \times 10^{11}\mathrm{A/m}^2$. Interestingly, this type of non-periodic oscillations start to appear at a smaller current ($J = -6 \times 10^{11}\mathrm{A/m}^2$) on the refined mesh of 4930 nodes. In fact, the smaller elements enable stronger variations, resulting in complex oscillations at smaller currents. Even if the two meshes give overall very similar results, we see that development of a strongly non-linear dynamics can depend very much on the mesh size.

Two of these non-periodic oscillations are shown in figures 2.11 and 2.12.

In general, a periodic signal of frequency f_0 modulated by a slower oscillation at $f_1 \ll f_0$ is seen in the Fourier spectrum as a main peak at f_0 surrounded by two neigh-

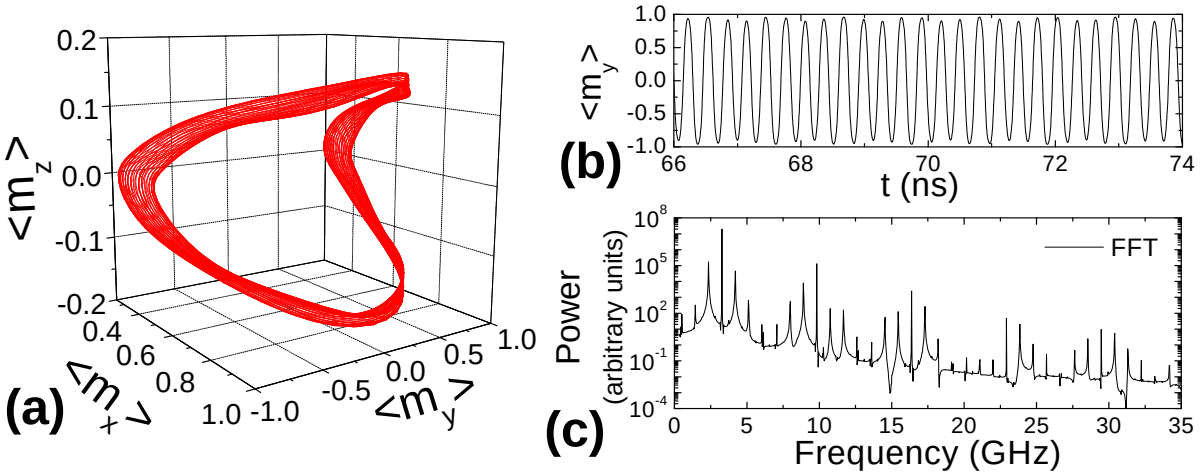

Figure 2.11: Simulation at $B = 12\,\mathrm{mT}$ and $J = -6 \times 10^{11}\mathrm{A/m}^2$. (a) Mean magnetisation trajectory. (b) Time trace of $\langle m_y \rangle$. (c) Fourier spectrum.

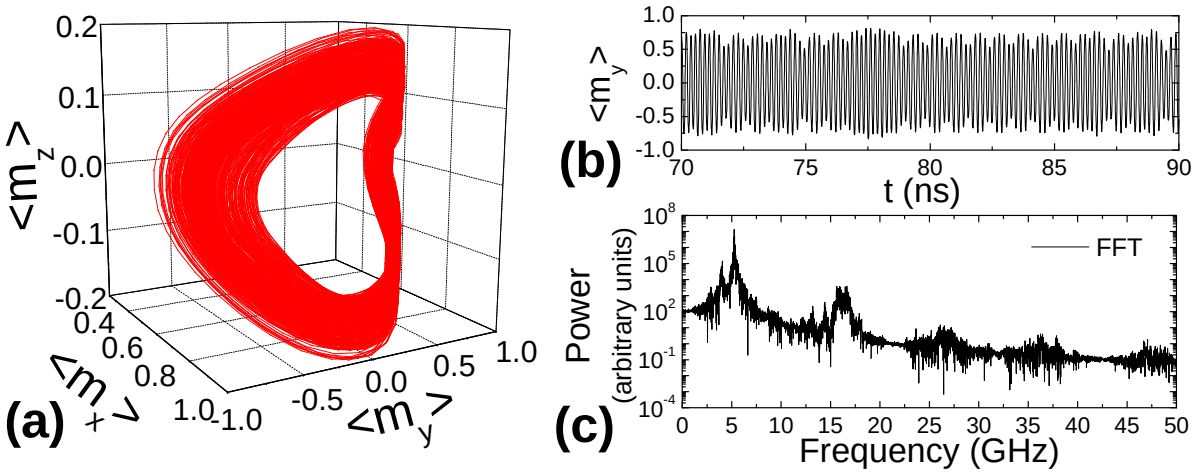

Figure 2.12: Simulation at $B = 32.5\,\mathrm{mT}$ and $J = -6 \times 10^{11}\mathrm{A/m}^2$. (a) Mean magnetisation trajectory. (b) Time trace of $\langle m_y \rangle$. (c) Fourier spectrum.

bouring peaks at $f_0 + f_1$ and $f_0 - f_1$. Here, the figure 2.11b shows a time trace with modulations at several frequencies. This pseudo-periodic signal results in a Fourier spectrum exhibiting multiple peaks, but still discrete.

In contrast, the oscillation represented in figure 2.12 has very strong variations of its amplitude and its frequency. It was of course not reported on the frequency curve. Even though it is still an IPP (figure 2.12 a), its Fourier spectrum is very complex. Such dynamics may be qualified as "chaotic". However, a specific study of chaos has not been conducted in this system, and therefore evidence for a chaotic motion has not been demonstrated. In particular, high sensitivity to initial conditions has to be shown for chaos.

After a detailed presentation of the simulation results, a thorough analysis is performed to understand the origin of jumps.

2.6 Data analysis

It is remarkable that frequency jumps exist in such a simple model where a lot of assumptions are made and the polariser is supposed fixed. One may think that frequency discontinuities are due to excitation of other layers, but FEM simulations show that oscillations of a single layer can already lead to very complex dynamics. In the following, we will be interested only in the periodic oscillations previously observed. Moreover, the word "branch" will refer to the precessional modes of figure 2.8 that are distinguished by different colours. For example the "branch 4" of $J = -5 \times 10^{11}\mathrm{A/m}^2$ is the blue branch ranging from 12 mT to 18 mT, whereas "branch 5" is the one coloured in cyan ranging from 19 mT to 25 mT.

2.6.1 Mean magnetisation characteristics

Mean magnetisation trajectories

As explained in section 2.1, the magnetisation trajectory is an In-Plane Precession about the x-axis. In this part, we will be interested in the magnetisation vector averaged over the volume of the FL.

The mean magnetisation trajectories are plotted in figure 2.13 for a current density $J = -5 \times 10^{11}\mathrm{A/m}^2$. Each line correspond to a particular branch on the figure 2.8, which means each line is separated by a frequency jump. The typical clam-shell shape is observed in the "3D trajectory" (first column), while the other two columns show $\langle m_y \rangle$ vs $\langle m_z \rangle$ and $\langle m_z \rangle$ vs $\langle m_x \rangle$.

As mentioned earlier, IPP results from the competition between spin torque, applied-field torque and damping torque. The spin torque tends to reverse the magnetisation while the applied-field torque is roughly directed along $\mathbf{u}_\theta$. Therefore one expects the magnetisation trajectory to become "less elliptical" when the field is increased at a fixed current. This trend is indeed observed in the figure 2.13: the in-plane incursion angle decreases with applied field. On the other hand, the out-of-plane angle is limited by the large demagnetising field.

Within each branch, the trajectories at different fields seem perfectly parallel. This is particularly striking in the YZ-plane plots. Thus, each branch has its own characteristic trajectory, with an amplitude depending on the field. The shapes are more complex than in macrospin, as shown on the plot of branch 5: some parts of the trajectories are almost flat, whereas others have a very large curvature. These complicated shapes originate from a complex underlying dynamics with large spatial variations that will be discussed in the next section.

On can notice that, for each branch, the trajectory with the smallest amplitude is the one at the lowest field; then the amplitude increases until the "end of the branch" (i.e.

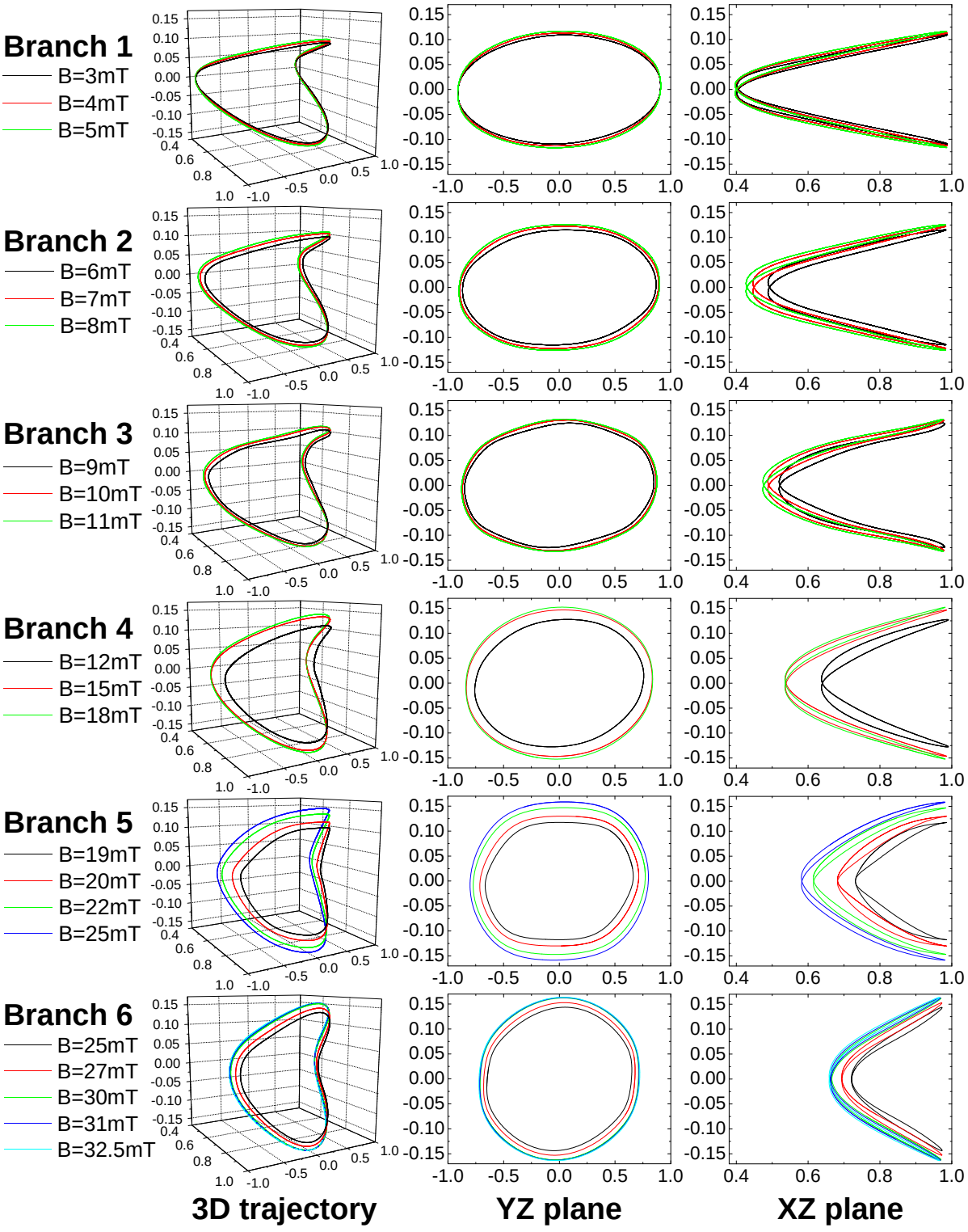

Figure 2.13: Trajectories of the mean magnetisation at $J = -5 \times 10^{11}\mathrm{A/m}^2$. "3D trajectory": $\langle m_z \rangle$ as a function of $\langle m_x \rangle$ and $\langle m_y \rangle$. "YZ plane": $\langle m_z \rangle$ as a function of $\langle m_y \rangle$. "XZ plane": $\langle m_z \rangle$ as a function of $\langle m_x \rangle$.

until the largest field value of the branch). The amplitude increase is slower towards the

end of the branch, like if the trajectory were being stabilised.

Maximum incursion angles

The frequency discontinuities observed in the micromagnetic simulations coincide with a change in the shape of the mean magnetisation trajectory. However, describing dynamics with the trajectories cannot be done comprehensively for all the fields and all the currents. Therefore, one needs physical quantities to characterise the oscillations. Maximum incursion angles are one of these.

In order to quantify the amplitude of the mean magnetisation trajectory, let us define the maximum in-plane incursion angle

$$\varphi_{max} = \max\left(\arctan\frac{\langle m_y\rangle}{\langle m_x\rangle}\right), \tag{2.2}$$

and the maximum out-of-plane angle

$$\theta_{max} = \max\left(\arctan\frac{\langle m_z\rangle}{\sqrt{\langle m_x\rangle^2 + \langle m_y\rangle^2}}\right). \tag{2.3}$$

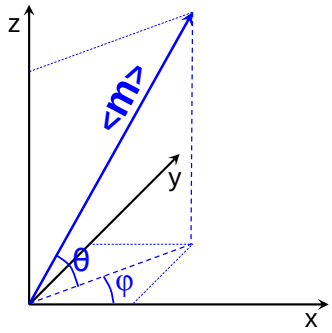

Figure 2.14: φ in-plane angle and θ out-of-plane angle characterising the amplitude of the mean magnetisation trajectory.

Note that $\theta_{\max}$ is not the usual angle defined in the spherical coordinate system (figure 2.14).

$\theta_{\max}$ and $\varphi_{\max}$ are plotted in figure 2.15. Interestingly, discontinuities are observed at $J = -3.4 \times 10^{11}\mathrm{A/m}^2$, just above the critical current (see the zooms), whereas no obvious frequency jumps were seen in fig. 2.8. Discontinuities are therefore inherent to self-sustained oscillations and exist for any current greater than J_c.

In the figure 2.15a, one can see that $\varphi_{\max}$ generally increases within each branch and decreases abruptly at the discontinuities, which confirms the trend observed in the figure 2.13. However, at large field, $\varphi_{\max}$ tends to decrease slightly with field.

Similarly, in the figure 2.15b, the general trend for $\theta_{\max}$ is an increase within each branch and an abrupt decrease at the discontinuity. These conclusions are in agreement with the plots of figure 2.13. At large current and field, the behaviour is more complex.

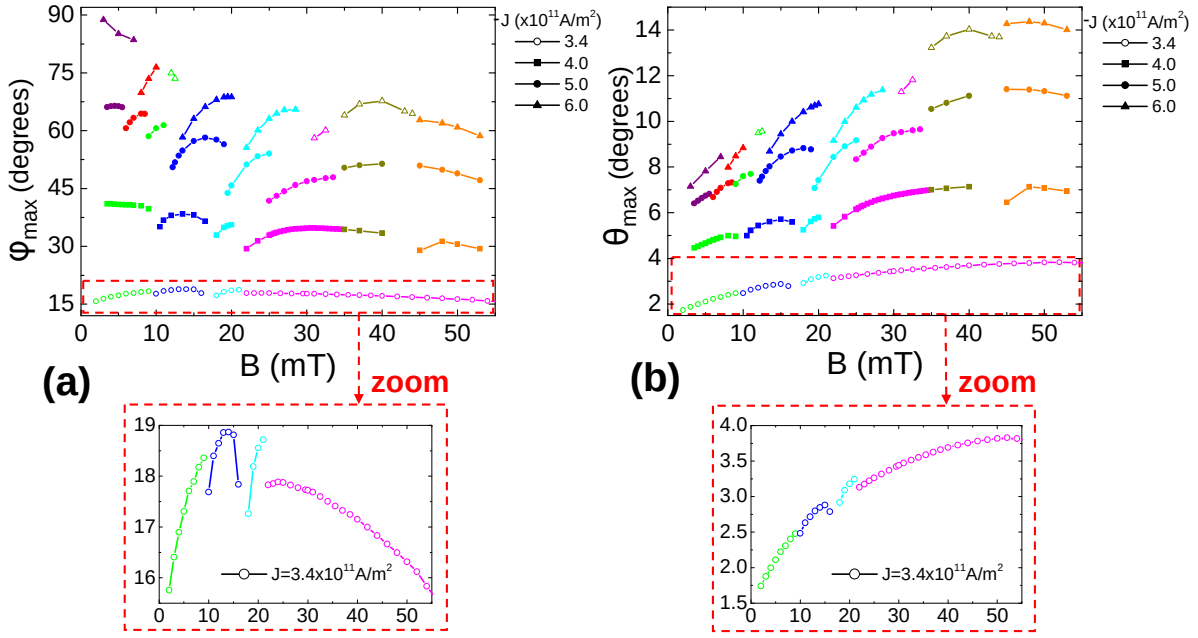

Figure 2.15: Maximum incursion angles of the mean magnetisation as a function of the applied field. (a) φ_{max} vs B_{app} (b) θ_{max} vs B_{app}. Each colour represents a particular branch following the same colour code as in the figure 2.8. Each symbol is associated with a certain current value. The zooms show the evolutions of the angles for the smallest current value, $J = -3.4 \times 10^{11}\mathrm{A/m}^2$, that was simulated with the order 1 time scheme in feeLLGood.

Like in the curves of f vs B, one notice large jumps at high current, while they seem to tend to zero when $J \to J_c$.

IPP are sometimes considered as "small oscillations" around an energy minimum. Here, the simulations show that this hypothesis clearly does not hold: at $J/J_c = 1.06$ (i.e. $J = -3.4 \times 10^{11}\mathrm{A/m}^2$), the mean magnetisation deviates by 18° from the precession axis, while at $J/J_c = 1.25$ (i.e. $J = -4 \times 10^{11}\mathrm{A/m}^2$), $\varphi_{\max}$ is already $\approx 40°$.

2.6.2 Micromagnetic configurations

The mean magnetisation trajectory is an In-Plane Precession about the x-axis. However, unlike macrospin, the magnetisation is not uniform. A large precession angle induced by the strong spin torque leads to a complex dynamics with spatial variations mainly due to the competition between exchange and dipolar interactions. Thus, the trajectories of local magnetic moments can be very different from the averaged precessional trajectory.

Evolution of micromagnetic configuration is very informative and gives a first insight of the differences between the branches. Figures 2.16 and 2.17 show the micromagnetic configurations along more than a quarter of a period for the branches 4 and 5 at $J = -5 \times 10^{11}\mathrm{A/m}^2$. The next quarter-period can be obtained by simply drawing the symmetric snapshots with respect to the x-axis. The colour code represents the exchange energy

density, indicating in red the regions of large spatial variation of magnetisation.

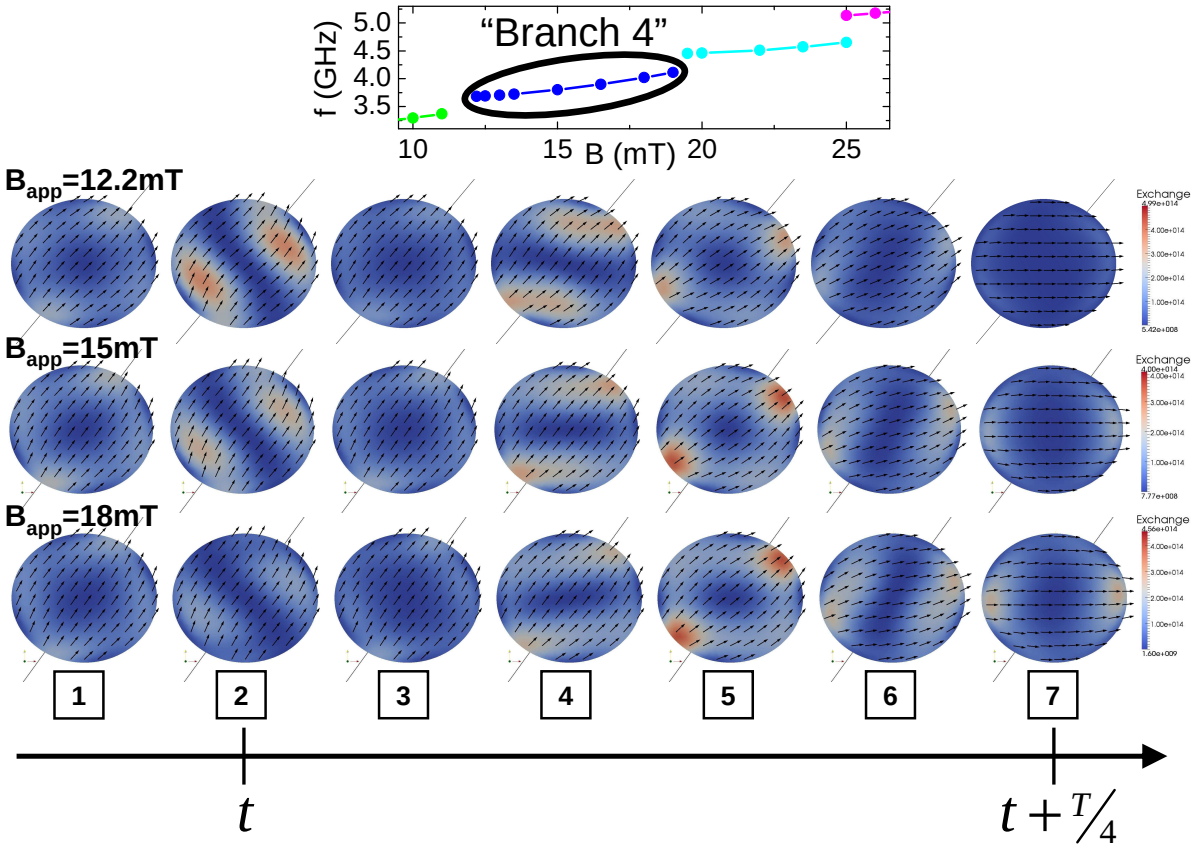

Figure 2.16: Micromagnetic configurations of branch 4 at $J = -5 \times 10^{11}\mathrm{A/m}^2$, along more than a quarter period. The colour shows exchange energy density (reduced units).

It is interesting to note that, for each figure, the snapshots in a same column are very similar, which means that a branch is characterised by the evolution in time of its micromagnetic configuration. In the figure 2.16 corresponding to branch 4, a grey axis shows the maximum in-plane angle. In columns 2-3-4, a small oscillation can be seen about this axis. In fact, some local moments on the edge continue to rotate, influenced by surface magnetic charges, while the magnetisation in the centre stays almost still for these three configurations. In contrast, for the branch 5, this kind of small oscillation occurs twice in one quarter period: in fig 2.17, the configurations with large magnetisation variations are in columns 2 and 6. The two grey axes show the mean directions of these distorted magnetisation configurations. Like in branch 4, these spatial variations are induced by the distribution of magnetic surface charges on the edge.

Interestingly, the large magnetisation distortions (columns 2 and 4 in fig. 2.16, and columns 2 and 6 in fig. 2.17) are very large at the beginning of the branch (12.2 mT for branch 4, and 19.5 mT for branch 5), but are attenuated when the field is increased. This behaviour is consistent with insets of figure 2.8 showing that micromagnetism and macrospin are close only "at the end" of the branches. Thus, it seems that after a frequency jump, a new oscillation mode is excited, generating large spatial variations of

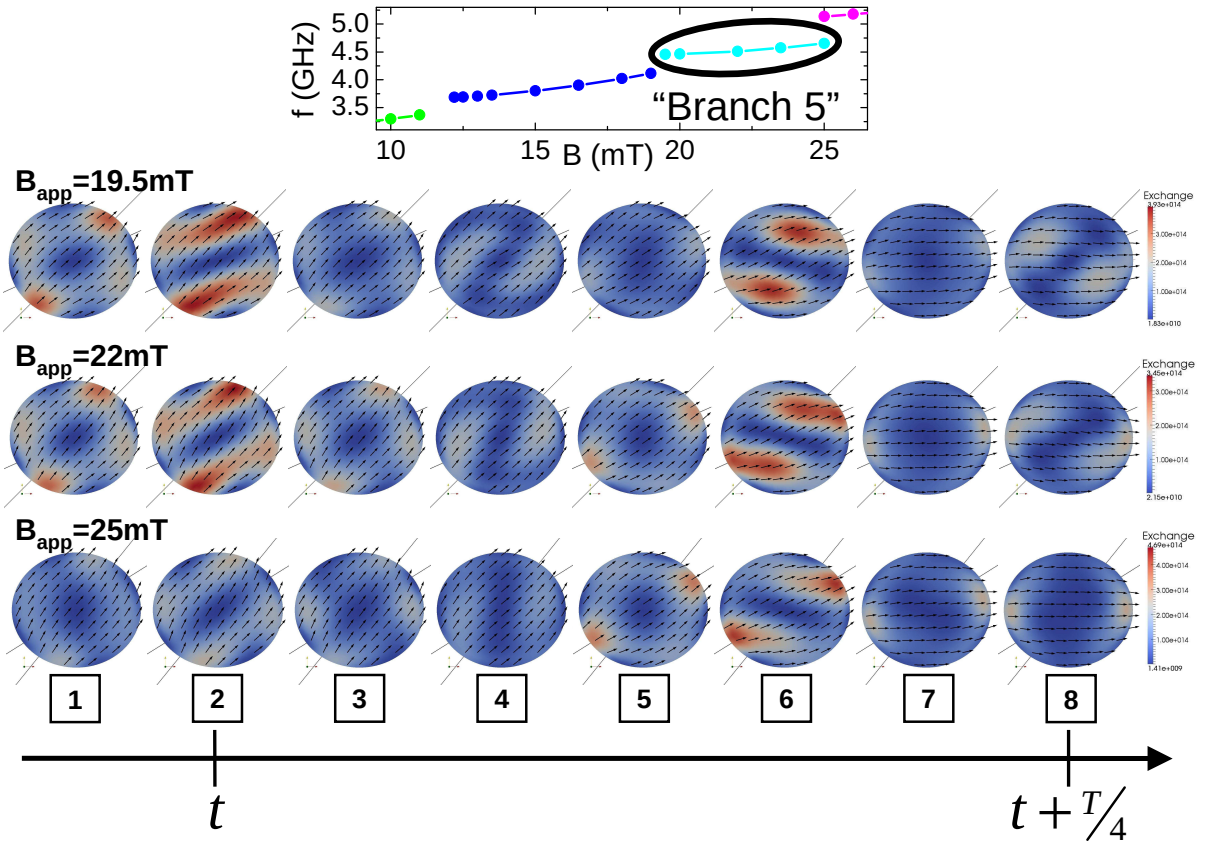

Figure 2.17: Micromagnetic configurations of branch 5 at $J = -5 \times 10^{11}\mathrm{A/m}^2$, along more than a quarter period. The colour shows exchange energy density (arbitrary units).

magnetisation. The deviation from uniform precession is maximum just after the jump, and then decreases until the micromagnetic branch joins the macrospin frequency curve.

2.6.3 Energy analysis

Similarly to mean magnetisation trajectories that are a qualitative tool to analyse the simulations, micromagnetic configurations allow to visualise the differences between the branches but cannot describe dynamics do not provide quantitative information. However, micromagnetic energies, such as dipolar, exchange, and Zeeman energies, reveal a lot of details about the underlying physics governing magnetisation oscillations. In this section, an analysis of the energies of the system will be conducted for a better understanding of IPP discontinuities.

Since all the energies vary in time, we extracted the energies averaged over one period of stabilised oscillation for each simulation. Dipolar, exchange, and total energies are plotted in figure 2.18. The overall decrease of the total energy is due to the Zeeman energy (not shown) which takes large negative values at high field.

The variation of dipolar energy is very similar to the variation of θ_{max} plotted in figure 2.15b. Indeed, in thin layers, the dipolar interaction is dominated by magnetostatic

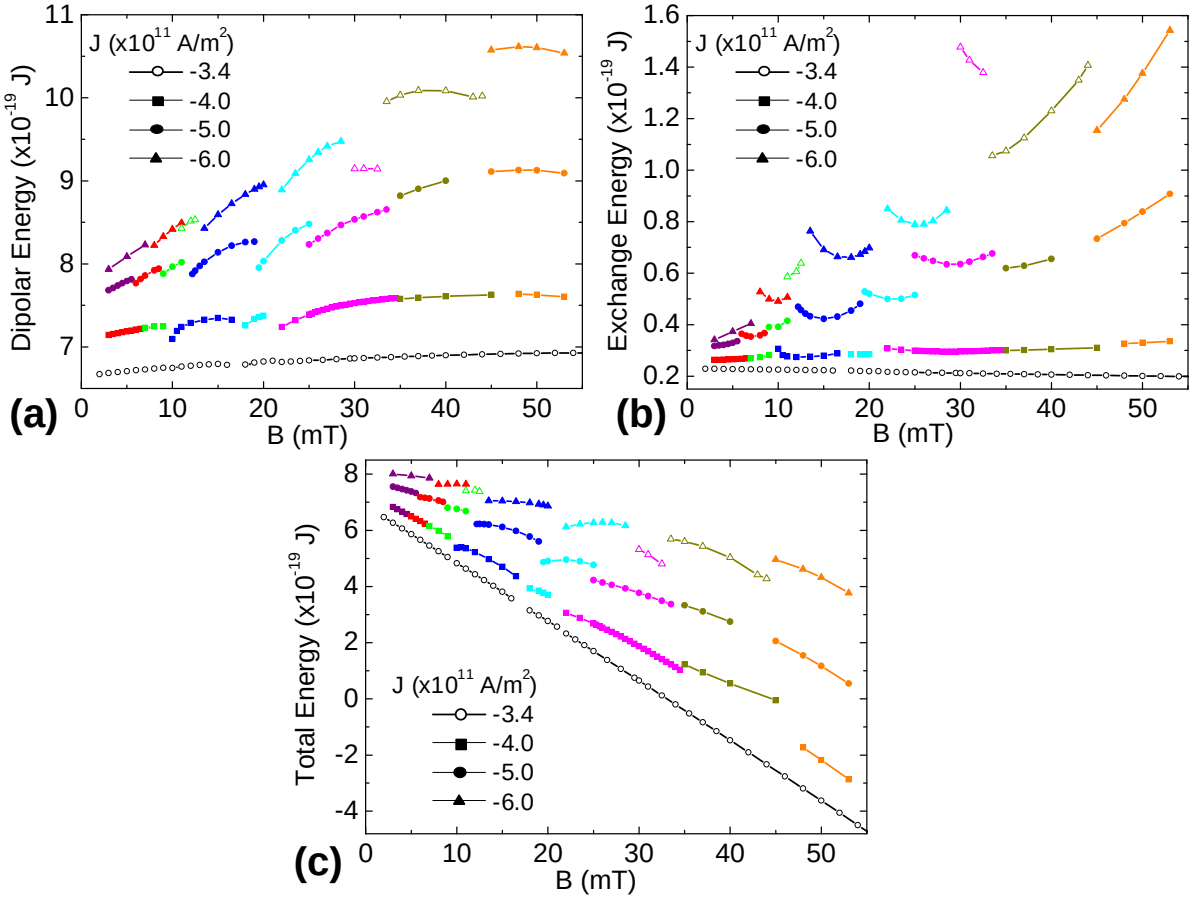

Figure 2.18: (a) Dipolar energy vs applied field. (b) Exchange energy vs applied field. (c) Total energy vs applied field. All the energies are averaged over time for a stabilised oscillation. Each colour represents a particular branch following the same colour code as in the figures 2.8 and 2.15.

surface charges that create a strong out-of-plane demagnetising field when the magnetisation is not exactly in plane. Thus, all the comments made in section 2.6.1 about $\theta_{\max}$ are also true for the demagnetising energy.

According to the previous section, one may expect the exchange energy to monotonically decrease inside each branch, because large spatial variations are attenuated with increasing field. However, fig. 2.15b shows parabolic curves for most branches. The negative slope at the beginning is well explained by the attenuation of spatial variations. However, to understand the decrease of exchange energy towards the end of the branches, one has to be aware that in the micromagnetic configurations of figures 2.16 and 2.17, the exchange energy density was rescaled at each field. In fact, these snapshots already showed that the exchange energy was increasing at the end. One possible explanation is that the variation at the end of the branch is simply linked to the overall variation between 3 mT and 50 mT. The region of uniform magnetisation in the centre is larger, due to increased external field, but the small domains induced by surface charges on the border still exist. Therefore, the "domain walls" between centre and edge have to be

thinner, hence an increased exchange energy.

Discontinuities of exchange energy consist in abrupt increases, except at large field where the exchange energy exhibits a few "downward jumps".

2.6.4 Micromagnetic Spectral Mapping Technique

Method

The Micromagnetic Spectral Mapping Technique (MSMT) is a method to analyse the dynamic modes of a nanomagnet from micromagnetic simulations. It was first used by McMichael and Stiles [102] to study the FMR modes of an elliptical permalloy layer. Starting from a minimum energy state, they sent a strong field pulse. During the relaxation process, several FMR modes (or *normal modes*) are excited, depending on the symmetry of the pulse. The Fourier spectrum is then the superposition of all the frequencies of the excited modes. During the simulation, the micromagnetic configuration $\mathbf{m}(\mathbf{r}_i, t_j)$ is saved at constant time intervals. Then the local power spectrum $S_x(\mathbf{r}_i, t_j)$ is calculated for a given coordinate (here, x). $S_x(\mathbf{r}_i, t_j)$ is equal to the modulus squared of the discrete Fourier transform

$$S_x(\mathbf{r}_i, f) = \left| \sum_j m_x(\mathbf{r}_i, t_j) e^{i2\pi f t_j} \right|^2 \tag{2.4}$$

Then, the total power spectrum is computed by summing over all the nodes

$$\bar{S}_x(f) = \sum_i S_x(\mathbf{r}_i, f) \tag{2.5}$$

It is worth noting that the average of the local powers $\frac{1}{N}\bar{S}_x(f)$ is different from the power of the averaged magnetisation $\left|\sum_j \bar{m}_x(t_j) e^{i2\pi f t_j}\right|^2$. Indeed, if a normal mode consists in two parts of the sample oscillating in anti-phase, then m_x may be positive in one part while it is negative in the other part. Therefore, $\bar{m}_x$ will be always zero, and the frequency of this normal mode will not appear in the spectrum of the mean magnetisation. In contrast, all the frequencies are included in $\bar{S}_x(f)$. In FMR simulations, the spectrum is computed for a spatial coordinate transverse to the precession axis, longitudinal variations being neglected because of second-order.

When a spectrum is computed, one can select a normal frequency f_n and plot a map $S_x(\mathbf{r}_i, f_n)$ of the local contribution to this frequency. Generally, the greater the number of node lines on the map, the greater the frequency.

The MSMT has been used by other groups [97, 99, 100, 103] to study spin-transfer-driven precession. These analyses have been useful to show the complexity of large-amplitude oscillations.

However, MSMT of large-amplitude oscillations has to be treated with particular care because the longitudinal component is no longer negligible. As shown in section 2.6.1,

the excursion angle can be larger than 50° or even 90°. Therefore, to perform MSMT analysis, one should also consider the component along the precession axis.

Analysis of feeLLGood results

A typical spectrum is shown on figure 2.19. It was computed as explained above for a stabilised IPP oscillation at $B = 26\,\mathrm{mT}$ and $J = -5 \times 10^{11}\mathrm{A/m}^2$. It clearly shows a series of peaks of frequency nf_0. These harmonics are the sign of an perfectly periodic signal, as we will see later. The highest peak of the spectrum is at $2f_0$ because the longitudinal component m_x has been analysed. Indeed the transverse oscillation at f_0 generates an oscillation of the longitudinal component at $2f_0$ by conservation of the norm of the magnetisation. Since f_0 is the highest peak in the "transverse spectrum", $2f_0$ has to be prevailing in the spectrum of the longitudinal component.

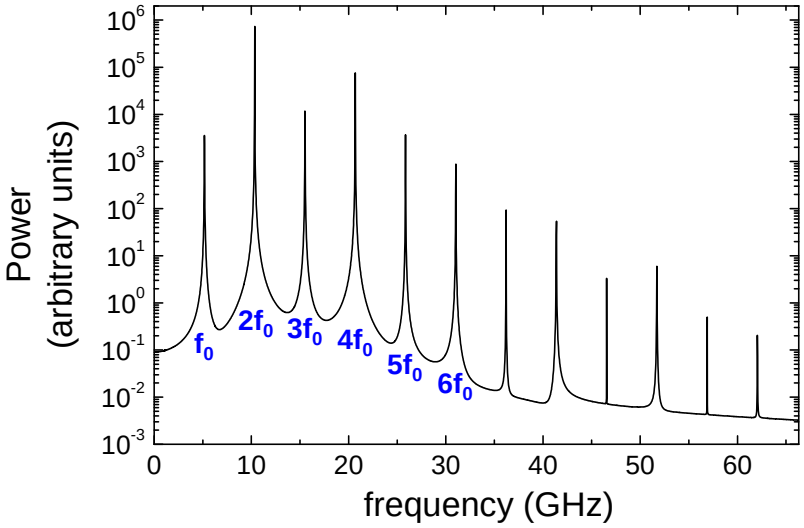

Figure 2.19: $\bar{S}_x(f)$: power along the longitudinal component as a function of the frequency, at $B = 26\,\mathrm{mT}$, $J = -5 \times 10^{11}\mathrm{A/m}^2$.

The amplitude of the local power $S(\mathbf{r}_i, nf_0)$ has been computed for the first 6 harmonics for along the x-axis and along the y-axis. The maps of branch 4 and branch 5 are presented in figure 2.20. The regions giving the largest contribution to the corresponding peak are represented in white. The maps obtained analysing the z component are not shown but it ought to be mentioned that they are very similar to the y-component maps. In fact, they have to be considered as the maps of the transverse component.

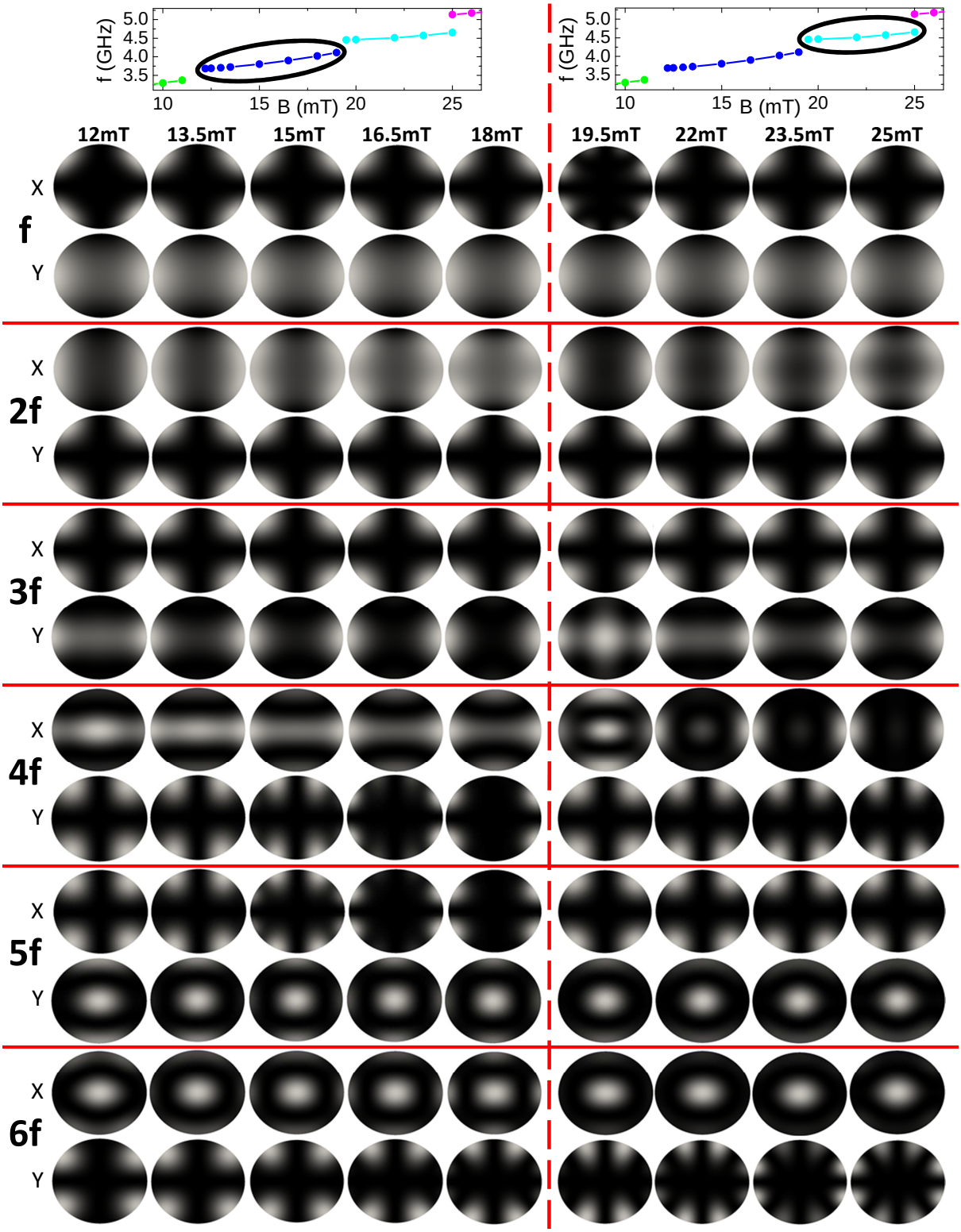

Figure 2.20: Spectral maps at $J = -5 \times 10^{11}\mathrm{A/m}^2$ for the branch 4 (left-hand side) and the branch 5 (right-hand side). For each harmonic, the first line contains the maps obtained for m_x (longitudinal component) and the second line for m_y (transverse component). The regions in white give the largest contribution to the power of the corresponding peak.

The maps of (nf, Y) (transverse component) are very similar to the maps of $((n+1)f, X)$ (upper harmonic, longitudinal component). This can be understood writing that the transverse components are

$$m_{y,z} = \sum_{n=1}^{N} [a_n^{y,z}(\mathbf{r})\cos(n\omega t) + b_n^{y,z}(\mathbf{r})\sin(n\omega t)] \tag{2.6}$$

and the subsequent longitudinal component, deduced by conservation of the norm, is

$$|m_x| = \sqrt{1 - (|m_y|^2 + |m_z|^2)} \tag{2.7}$$

Considering the norm of the transverse component as small compared to 1, a Taylor expansion leads to

$$\begin{aligned} |m_x| \approx 1 &- \frac{1}{2}\sum_{n=1}^{N} |a_n^y(\mathbf{r})\cos(n\omega t) + b_n^y(\mathbf{r})\sin(n\omega t)|^2 \\ &- \frac{1}{2}\sum_{n=1}^{N} |a_n^z(\mathbf{r})\cos(n\omega t) + b_n^z(\mathbf{r})\sin(n\omega t)|^2 \end{aligned} \tag{2.8}$$

With $N = 1$, it is shown that the transverse oscillation at f_0 leads to an oscillation of m_x at $2f_0$. The most excited regions are the ones with the largest coefficients $(a_1^y)^2 + (b_1^y)^2$ and $(a_1^z)^2 + (b_1^z)^2$. Therefore, the maps of the transverse component at f should be similar to the maps of the longitudinal component at $2f$. Similarly, it is shown by recursion on N that the maps of the transverse component at nf are similar to the maps of the longitudinal component at $(n+1)f$.

In figure 2.20, the same pattern is often repeated on the same line, except at $(3f, Y)$ and $(4f, X)$. These two lines show that a mode is excited at the frequency $3f$ (for the transverse component) with a maximal amplitude at the beginning of the branch. This observation agrees with the plots of micromagnetic configurations in section 2.6.2. Remarkably, the other harmonics are not affected. Thus, it seems that frequency jumps occur when a new mode is excited. The frequency of this mode is not the oscillation frequency f, but rather the harmonic $3f$. Its amplitude decreases when the field increases.

2.6.5 Comparison with the FMR normal modes

In a system where oscillations are small deviations from the equilibrium state, it is possible to decompose the magnetisation motion on a basis of eigen-modes (or *normal modes*). These eigen-modes are derived in the limit of small oscillations [104]. Several techniques exist to compute the micromagnetic normal modes of a ferromagnetic sample. For this, we have used the software Spinflow [59].

The eigen-modes are shown on figure 2.21 with the eigen-frequencies plotted as a function of applied field. On the same figure, the frequencies of IPP harmonics are plotted for $J = -5 \times 10^{11}\mathrm{A/m}^2$. One would expect the eigen-modes to be the "perturbation

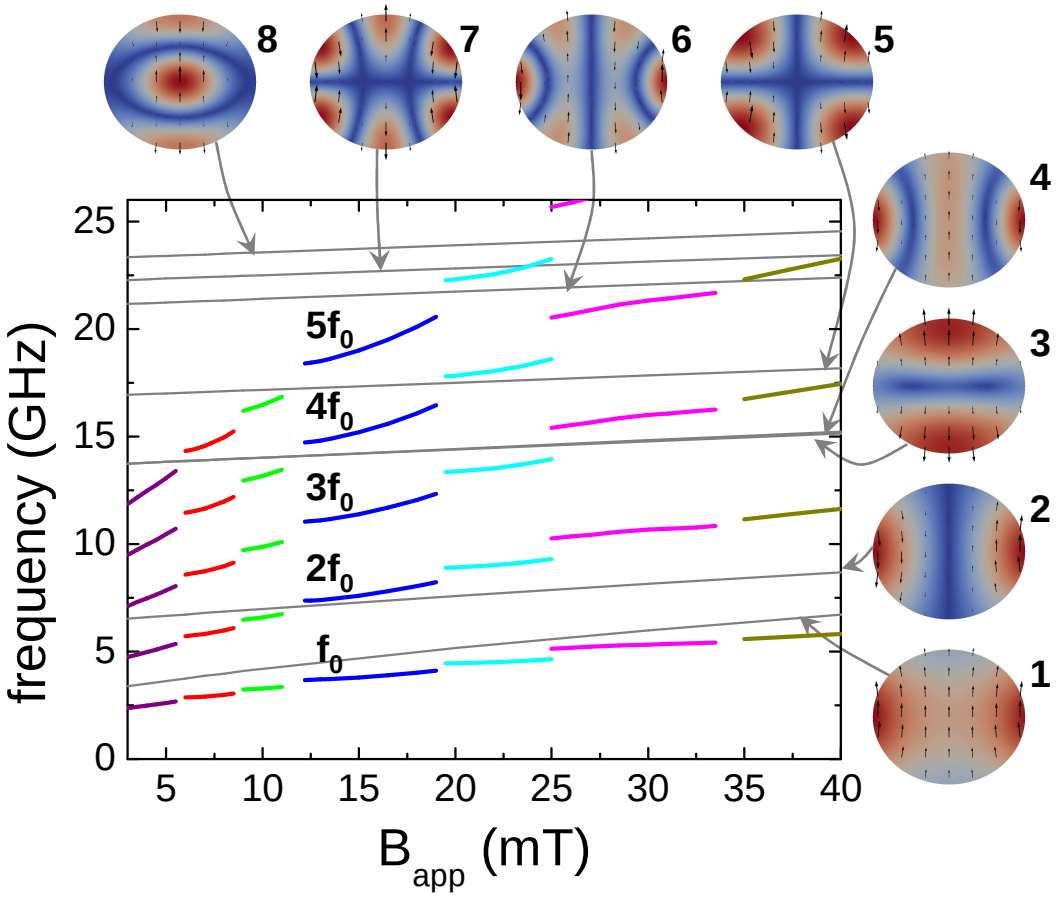

Figure 2.21: Configurations: free layer eigen-modes. f vs B_{app}: eigen-frequencies (in grey) and harmonic frequencies at $J = -5 \times 10^{11}\mathrm{A/m}^2$ (same colours as in previous figures).

modes" excited at the beginning of each branch. Thus, the curve of $3f$ (or another harmonic frequency) would cross an eigen-frequency at the beginning of each branch. The reality is more complex. First, the excited modes at ($3f$, Y) in fig 2.20 cannot be clearly identified to eigen-modes, even though the eigen-mode 4 in figure 2.21 resembles the mode ($3f$, Y, 19.5 mT). Second, it seems that the modes excited at the beginning of each branch have a strong variation of their longitudinal component, as shown by the maps ($4f$, X). Therefore, these perturbation modes are not normal modes but non-linear modes. Currently, no theory is available allowing to check the frequency of these non-linear modes. It is expected that their frequencies at the beginning of the branches is given by $3f$.

To summarise, when the field (or the current) is varied, the oscillation frequency is also varied. If a harmonic is close enough to the frequency of a non-linear mode, this mode can be excited. The sudden excitation is accompanied by a jump in the IPP oscillation frequency. Continuing to increase the field (or the current), the frequency varies smoothly, but the excitation of the non-linear mode decreases because the harmonic frequency moves away from resonance frequency of the mode.

2.6.6 Decomposition in Fourier series: "Time-Dependent Micromagnetic Spectral Mapping Technique"

The Fourier spectrum in figure 2.19 exhibits only harmonic frequencies, showing that IPP oscillations cannot be decomposed on a basis of FMR modes. Otherwise, only eigenfrequencies would exist in the spectrum. It proves again that IPP is a large-amplitude oscillation behaving differently from small oscillations around equilibrium state.

In fact, a perfectly periodic signal is always a sum of harmonics. As stated by the Dirichlet's theorem, if $f(t)$ is a periodic function, it can be decomposed onto the basis of $(\cos(n\omega t))_n and (\sin(n\omega t))_n$ functions. Magnetisations at each node of the system seem periodic. To check that it is the case, the decomposition in Fourier series was performed at each node for each component of $\mathbf{m}$. The coefficients of the Fourier series of the first 6 harmonics are computed:

$$a_n^{x,y,z}(\mathbf{r}_i) = \frac{2}{T}\int_t^{t+T} m_{x,y,z}(\mathbf{r}_i, t)\cos(n\omega t)dt \tag{2.9}$$

$$b_n^{x,y,z}(\mathbf{r}_i) = \frac{2}{T}\int_t^{t+T} m_{x,y,z}(\mathbf{r}_i, t)\sin(n\omega t)dt \tag{2.10}$$

where $T = 1/f$ is the period, and $\mathbf{r}_i$ is the position of the node. Summing the first 6 harmonics and the dc component, the original magnetisation is reconstructed:

$$\begin{aligned}\mathbf{m}(\mathbf{r}_i, t) \approx &\left[\frac{a_0^x(\mathbf{r}_i)}{2} + \sum_{n=1}^{6}\left(a_n^x(\mathbf{r}_i)\cos(n\omega t) + b_n^x(\mathbf{r}_i)\sin(n\omega t)\right)\right]\hat{\mathbf{x}} \\ &+ \left[\frac{a_0^y(\mathbf{r}_i)}{2} + \sum_{n=1}^{6}\left(a_n^y(\mathbf{r}_i)\cos(n\omega t) + b_n^y(\mathbf{r}_i)\sin(n\omega t)\right)\right]\hat{\mathbf{y}} \\ &+ \left[\frac{a_0^z(\mathbf{r}_i)}{2} + \sum_{n=1}^{6}\left(a_n^z(\mathbf{r}_i)\cos(n\omega t) + b_n^z(\mathbf{r}_i)\sin(n\omega t)\right)\right]\hat{\mathbf{z}}\,,\end{aligned} \tag{2.11}$$

As illustrated on figure 2.22, the first 6 harmonics are sufficient to render rapid variations of the magnetisation. We have therefore verified that the magnetisation is indeed composed of a series of harmonics.

In the maps of figure 2.20, the local power represented in black and white is equal to $(a_n(\mathbf{r}_i))^2 + (b_n(\mathbf{r}_i))^2$. Information on the phase, and in particular on the phase difference between m_z and m_x or between m_z and m_y is missing. Consequently, a time-varying description of the modes has been developed, allowing to visualise the evolution of the micromagnetic configuration as the sum of each harmonic configuration. A video can then be made, as shown in figure 2.23.

On the video, each configuration is a pure harmonic oscillation. It is worth noting that the norm is not constant for the harmonic configurations.

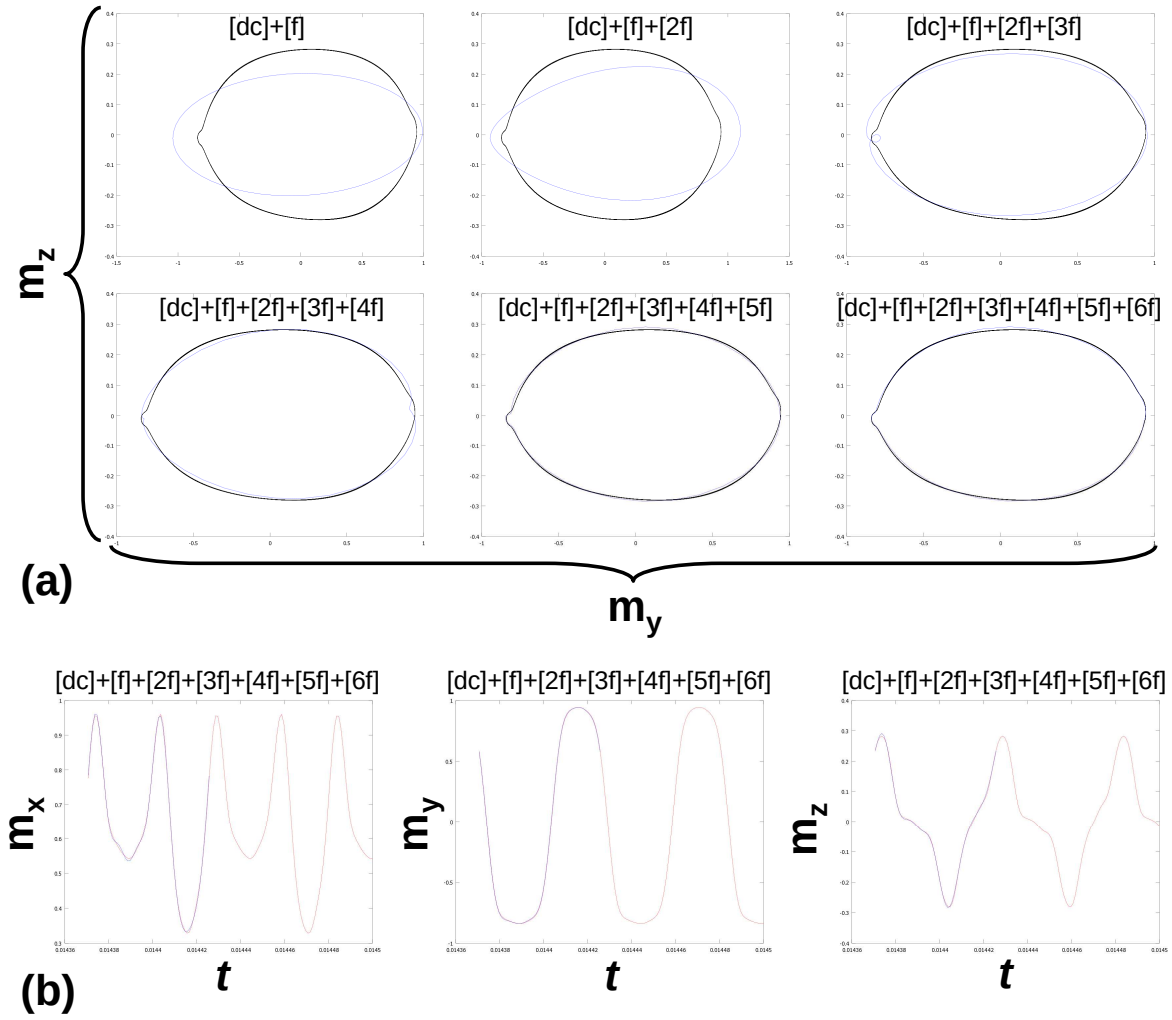

Figure 2.22: (a) Magnetisation trajectory in the YZ plane at a node of the mesh; in black: simulated magnetisation, in blue: reconstructed signal. (b) Time traces at a node of the mesh; in red: simulated magnetisation, in blue: first period of the reconstructed signal.

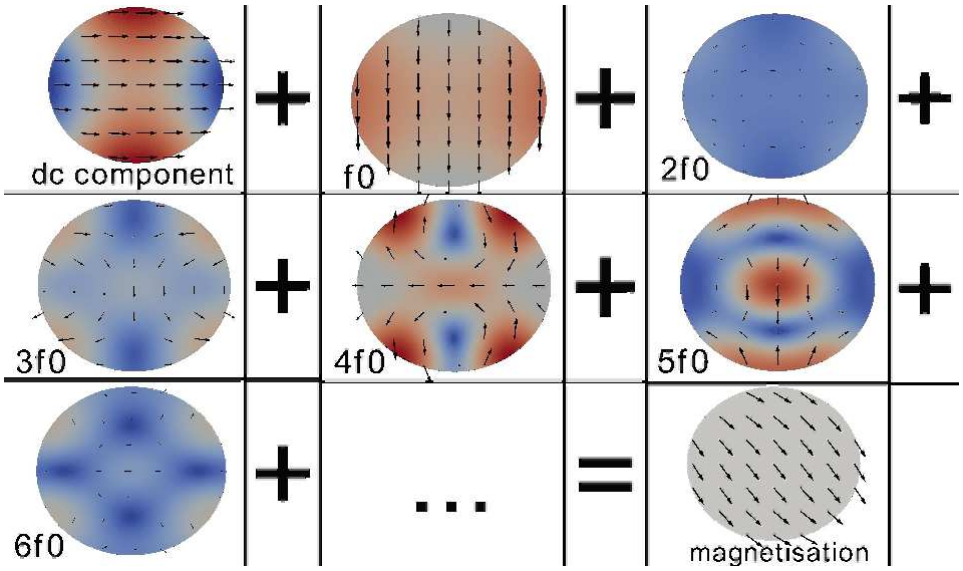

Figure 2.23: Snapshot of a video showing the decomposition of the magnetisation configuration as a series of harmonic configurations.

2.7 Conclusions of the chapter

The conclusions of this chapter are interesting for both the numerics and applications.

Numerical aspects

Simulations with the 2846-node mesh and the 4930-node mesh have exhibited very similar results. However, at large current, chaos is "favoured" by a refined mesh.

At large fields, the jumps in frequency do not show clear patterns. Therefore, above 40 mT, a smaller du_{max} should probably be chosen.

Moreover, computation of the critical current has shown that there is a problem with feeLLGood order 2 when the oscillation amplitude is small. It may be explained by a du_{max} too large when $\mathbf{m}$ is very close to $\mathbf{H_{eff}}$.

Applications

Jumps in frequency have been observed with feeLLGood. They are accompanied by discontinuities in incursion angles, micromagnetic configurations and energies for any current larger than the critical current. Using the Micromagnetic Spectral Mapping Technique, the origin of the jumps has been clarified. After each discontinuity, at the beginning of a branch, a mode is strongly excited at the frequency $3f$. This mode is non-linear as the variation of its longitudinal component is large, and therefore its pattern does not clearly match the configuration of any of the linear eigen-modes computed with Spinflow.

It is thought that a frequency jump appears when the curve $3f$ crosses the natural frequency of the excited non-linear mode. Thus, the series of "band gaps" observed in the figure 2.8 would give an indication about the frequency of the non-linear modes as a function of applied field.

In Houssameddine's experiment [1], the frequency jumps are correlated with linewidth maxima. This study is therefore also interesting if one wants to reduce the linewidth. However, a theory of non-linear modes is still missing.

Chapter 3

Spin-Torque Oscillator with perpendicular polariser and planar free layer

Contents

In this chapter, a Spin-Torque Oscillator (STO) with perpendicular polariser and planar free layer is studied. This type of STO was first fabricated and measured in Spintec, in collaboration with Leti [10]. The first part of this chapter will summarise theoretical results on magnetisation dynamics driven by an out-of-plane polarised current. In the second section, micromagnetic simulations will help to understand experimental measurements. Moreover, discrepancy between different numerical models will be discussed. Finally, new oscillating modes will be found starting from initial out-of-plane saturated state.

This system is the first one simulated with the version of feeLLGood including spin torque. Even though they were initially performed for benchmarking, they turned out to be also interesting for application purpose, in particular some of the modes computed from initial out-of-plane state.

3.1 Macrospin model

3.1.1 Description of the model

First studies of STO were performed in all-planar structures [52] where the action of an in-plane polarised current and an external field causes a precession of the free layer magnetisation. Another configuration has been explored where the in-plane free layer (FL) is associated with an out-of-plane polariser (PL) [10]. The main advantage of this structure is that no external magnetic field is required. When a current is applied, the spin torque pushes the magnetisation out of plane either along $-z$ if the current is positive, or along $+z$ if $J < 0$ (figure 3.1b). A strong demagnetising field opposite to m_z is created that drives the magnetisation in an out-of plane precession (OPP), as shown on Figure 3.1. Unlike the in-plane STO, a third layer is necessary to obtain a magnetoresistive signal generated by the oscillation. This in-plane magnetised layer is pinned by an anti-ferromagnet. By analogy with optics, it is called *analyser*. The OPP gives rise to large magnetoresistance variations, in contrast with IPP. It is of great interest for rf applications.

Even though the role of the analyser is to generate an output signal, it also induces spin-torque on the FL. Therefore, the influence of the spin-torques from both fixed layers should be considered in the simulations. However, since the STT from the analyser is not necessary to understand the basic physics of this type of STO, only the STT from the out-of-plane polariser will be taken into account.

Ref [105] presents a very comprehensive study of STO with perpendicular polariser and in-plane free layer. The macrospin model that is used allows to derive analytical equations which are very useful for a first insight. Most of the results presented in the following sections can be found in this reference.

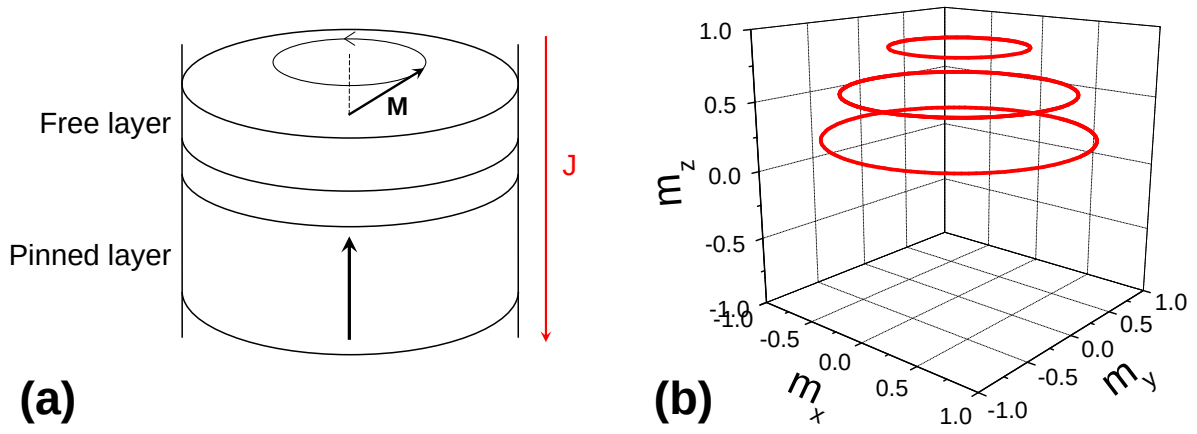

Figure 3.1: (a) Simulated system. (b) OPP trajectories at several current values; the one with the highest m_z value corresponds to the largest current amplitude.

3.1.2 Linearisation of the LLG equation

The OPP is an oscillation around the energy maximum, whereas IPP is an oscillation around the energy minimum. Therefore, one cannot draw an analogy between IPP and OPP.

The equation of motion, in the Gilbert form is written as

$$\dot{\mathbf{m}} = \mathbf{F}(\mathbf{m}) \tag{3.1}$$

$$\dot{\mathbf{m}} = \mathbf{F}(\mathbf{m}_0) + \left.\frac{\delta \mathbf{F}}{\delta \mathbf{m}}\right|_{\mathbf{m}_0} \delta\mathbf{m} + \mathcal{O}(\delta\mathbf{m}^2) \tag{3.2}$$

Denoting $\delta\dot{\mathbf{m}}$ the time derivative of $\delta\mathbf{m}$ (with $\delta\dot{\mathbf{m}} = \dot{\mathbf{m}} - \mathbf{F}(\mathbf{m}_0)$), one gets

$$\delta\dot{\mathbf{m}} \approx \left.\frac{\delta \mathbf{F}}{\delta \mathbf{m}}\right|_{\mathbf{m}_0} \delta\mathbf{m} \tag{3.3}$$

The term $\left.\frac{\delta \mathbf{F}}{\delta \mathbf{m}}\right|_{\mathbf{m}_0}$ is a 3×3 matrix in Cartesian coordinates or a 2×2 matrix in the spherical coordinate system. To solve equation 3.3, the complex eigenvalues of the matrix have to be calculated. In the case of a 2×2 matrix, the eigenvalues are two complex conjugates. The expression of the frequency $\omega = \omega' \pm i\omega''$ is given in ref [105] (another convention is used in this reference, the pulsation given has to be multiplied by i to obtain the ω that we have defined). ω depends on the field and the current density, therefore by tuning them, one can change the signs of ω' and ω''. The stability of the state $\mathbf{m}_0$ is given by the sign of the real part of ω. Three cases can be distinguished:

- $\omega' < 0$: $\mathbf{m}_0$ is a stable static state. The magnetisation returns to equilibrium after any "small" perturbation.
- $\omega' > 0$: $\mathbf{m}_0$ is unstable. Any perturbation leads to a divergence of the amplitude.

- $\omega' = 0$: $\mathbf{m}_0$ is on the critical line that mark the transition between a static stable state and a dynamic or another static state.

3.1.3 Static solutions

The static states can be determined by equating $\partial\mathbf{m}/\partial t$ to zero in the LLGS equation 1.106:

$$\mathbf{0} = -\gamma_0 \left(\mathbf{m} \times \mathbf{H_{eff}}\right) + \gamma_0 a_J \mathbf{m} \times \left(\mathbf{m} \times \mathbf{p}\right) \tag{3.4}$$

There are two solutions to equation 3.4: the in-plane stable state (IPS) and the out-of-plane stable state (OPS).

In the following, the z-axis is defined as the out-of-plane axis, while the x-axis is the easy axis of the free layer. The uniaxial anisotropy field is defined as $H_K = 2K_u/\mu_0 M_s$. An external field H_{app} is applied along the easy axis.

IPS state

The solution of the IPS state is

$$m_z = 0 \quad \text{and} \quad H_K m_x m_y + H_{app} m_y = a_J \tag{3.5}$$

which is, in spherical coordinates,

$$\theta_0 = 90° \quad \text{and} \quad H_K \sin\phi_0 \cos\phi_0 + H_{app} \sin\phi_0 = a_J \tag{3.6}$$

In absence of current ($a_J = 0$), the two equilibrium states are $\phi_0 = 0°$ and $\phi_0 = 180°$ which are the two energy minima. If $a_J \neq 0$, there is an in-plane rotation with respect to the easy axis. The stable state corresponds to compensated precession torque and spin torque. Solving equation 3.3 for a real part of the frequency equal to zero, the maximum in-plane angle and the associated critical current J_{c1} are deduced:

$$\cos\phi_c = -\frac{H_{app}}{2H_K} \pm \sqrt{\left(\frac{H_{app}}{2H_K}\right)^2 + \frac{1}{2}} \tag{3.7}$$

$$J_{c1} = \pm\frac{2e}{\hbar}\frac{\mu_0 M_s t}{g(\eta,\theta)}\left(H_K \sin\phi_c \cos\phi_c + H_{app}\sin\phi_c\right) \tag{3.8}$$

In the case when the applied field is zero, the critical in-plane angle ϕ_c is at 45° from the easy-axis, and the critical current is

$$J_{c1} = \pm\frac{2e}{\hbar}\frac{\mu_0 M_s t}{g(\eta,\theta)}\frac{H_K}{2} \tag{3.9}$$

The critical current is the maximum current at which the static IPS state is still possible. Above this threshold, the spin torque is larger than the precession torque and the magnetisation starts to precess out-of-plane. Numerical simulations show that

the maximum angle ϕ_c is reached if the current is increased very slowly, such that the magnetisation motion can be considered as quasi-static (at any time, the system is in a steady state). If the current is put on suddenly with an amplitude slightly smaller than J_{c1}, the in-plane angle increases rapidly, goes above ϕ_c, and the out-of-plane precession begins.

OPS state

The solution of the OPS state is given by

$$\begin{aligned} m_x &= -\frac{H_{app}}{M_s + H_K + \frac{a_J^2}{M_s}} \\ m_y &= -\frac{a_J}{M_s} m_x \\ m_z &= \pm\sqrt{1 - m_x^2 - m_y^2} \end{aligned} \tag{3.10}$$

In particular, if the applied field is zero, the magnetisation is out of plane ($m_z = \pm 1$). The OPS state is a local energy maximum in the energy landscape. This energy maximum is reached when enough power is injected into the system, that is when the current is above a threshold J_{c2}.

The stability is studied with the variational approach expressed by equation 3.3. The condition $\omega' = 0$ is equivalent to

$$J_{c2} = \pm\frac{2e}{\hbar}\frac{M_s t}{g(\eta,\theta)}\frac{\alpha}{2}\frac{H_{app}^2 - (H_K + M_s)(H_K + 2M_s)}{\sqrt{(H_K + M_s)^2 - H_{app}}} \tag{3.11}$$

Considering $H_{app} \ll M_s$, the onset of the OPS state is

$$J_{c2} \approx \pm\frac{2e}{\hbar}\frac{\mu_0 M_s t}{g(\eta,\theta)}\alpha\left(M_s + \frac{H_K}{2}\right) \tag{3.12}$$

J_{c2} is then almost independent of the applied field.

3.1.4 Bistability and state diagram

As already mentioned, the OPP is an oscillation around the energy maximum. When the current increases, the magnetisation trajectory goes up in the energy landscape, the amplitude is smaller and smaller and the system gets closer to the OPS state. If the current decreases, the spin torque becomes smaller, and the mean m_z value decreases while the amplitude increases. Then, the lower limit of OPP is no longer set by the current density $|J_{c1}|$, but rather by another value, $|J_{c4}|$ which can be smaller than $|J_{c1}|$, hence a bistability region between $|J_{c4}|$ and $|J_{c1}|$.

To summarise, in the most common case of $|J_{c1}| < |J_{c2}|$, if the current is slowly increased, the system goes into the following states:

1. $0 \leq |J| < |J_{c1}|$: IPS state
2. $|J_{c1}| < |J| < |J_{c2}|$: OPP
3. $|J_{c2}| < |J|$: OPS state

In contrast, if the current is decreased,

1. $|J_{c2}| < |J|$: OPS state
2. $|J_{c4}| < |J| < |J_{c2}|$: OPP
3. $0 \leq |J| < |J_{c4}|$: IPS state

In some peculiar cases, when the applied field is strong or when the uniaxial anisotropy is large, the current density J_{c2} can be smaller than J_{c1}. In such a case, if the current is slowly increased, the states reached by the system are:

1. $0 \leq |J| < |J_{c2}|$: IPS state
2. $|J_{c2}| < |J|$: OPS state

In contrast, if the current is decreased,

1. $|J_{c2}| < |J|$: OPS state
2. $|J_{c4}| < |J| < |J_{c2}|$: OPP ($|J_{c4}|$ is always less than $|J_{c2}|$)
3. $0 \leq |J| < |J_{c4}|$: IPS state

The state diagrams 3.2 shows the different IPS, IPP and OPS regions as a function of the applied field and the current density. The figure (a) corresponds to a constant spin efficiency $g(\eta, \theta)$, with $\eta = 0.3$ and $\theta = 90°$ (see formula 1.104). The regions $J < 0$ and $J > 0$ are therefore symmetric. In contrast, the diagram (b) was obtained taking into account the angular dependence of $g(\eta, \theta)$ (with $\eta = 0.3$). The OPS thresholds are modified, which results in an OPP region larger for negative current and smaller for positive current. In some cases (e.g. large anisotropy), the OPP region for $J > 0$ can even disappear whereas OPPs still exist for $J < 0$.

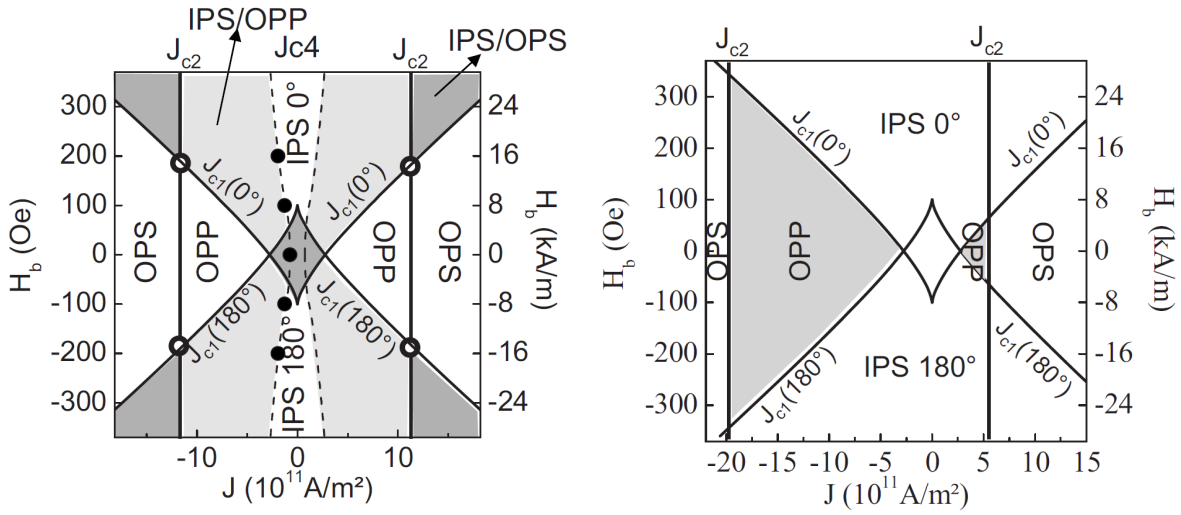

Figure 3.2: *Figures extracted from ref [105].* State diagrams of an STO with perpendicular polariser and planar free layer. (a) The spin efficiency $g(\eta, \theta)$ is assumed independent of the angle θ ($g(\eta, \theta) = g(0.3, \frac{\pi}{2}) = 0.17$). (b) State diagram with an angular dependant spin efficiency ($\eta = 0.3$ and θ variable).

3.1.5 Out-of-plane precession (OPP)

When an OPP trajectory is stabilised, the average of its total energy over one period is constant. Since the precession torque is a conservative torque, it does not contribute to any change in the energy. A magnetisation driven only by this torque would follow a trajectory of constant energy. However, in the LLGS equation, the damping torque and the Slonczewski torque are non-conservative. Therefore, in a stable trajectory, the loss of energy due to damping is compensated by the energy increase due to spin torque. The two torques do not need to be compensated at any time, but only over one precession cycle. Assuming that the applied field is small, the condition $\langle \mathcal{T}_{\text{damping}} \rangle + \langle \mathcal{T}_{\text{STT}} \rangle = 0$ leads to

$$\langle m_z \rangle = \cos\theta = -\frac{a_J}{\alpha \left(M_s + \frac{H_K}{2} \right)} \approx \frac{a_J}{\alpha M_s} \tag{3.13}$$

Using similar arguments, the lower boundary of OPP, J_{c4}, can be derived by numerical integration (see ref. [105]). J_{c4} is equal to zero only in the case of no applied field and zero uniaxial anisotropy. Moreover, in the same article, the frequency is also derived by integration over one precession cycle. The relation between the frequency and the out-of-plane component of the magnetisation is

$$f = \frac{\gamma_0}{2\pi} M_s \langle m_z \rangle \tag{3.14}$$

Substituting equation 3.13 in 3.14 yields

$$f \approx \frac{\gamma_0}{2\pi} \frac{a_J}{\alpha} = \frac{\gamma}{2\pi} \frac{\hbar}{2e} \frac{g(\eta, \theta)}{\mu_0 M_s t} \frac{J}{\alpha} \tag{3.15}$$

In the common approximation of a constant $g(\eta, \theta)$, the frequency is proportional to the current density. The figure 3.3b shows the frequency as a function of the current density in the case of $g(\eta, \theta) = g(0.3, \frac{\pi}{2}) = 0.17$ and in the case of an angular-dependent $g(\eta, \theta)$. The later situation leads to an asymmetry of f vs J. When m_z is negative (positive current), $g(\eta, \theta)$ decreases, whereas a positive m_z (negative current) leads to a rapid increase of $g(\eta, \theta)$ (see figure 1.4 for the plot of $g(\theta)$). Therefore, the frequency does not increase linearly with the current. For $J < 0$, the curvature of f vs J is negative and for $J > 0$ the curvature is positive. Taking into account the angular dependence of the spin efficiency is thus equivalent to rescaling the current density axis.

The maximum frequency, reached at $J = J_{c2}$, is

$$f_{\max} = \frac{\gamma_0}{2\pi} M_s \tag{3.16}$$

$f_{\max}$ is the FMR frequency of a magnetisation precessing about an effective field $H_{eff} = M_s$, because when $m_z \to 1$ the contribution of the demagnetising field becomes maximal, while other contributing fields vanish. For a spin-torque oscillator with no shape or magnetocrystalline anisotropy and no applied field, the macrospin model predicts a frequency ranging from 0 to $\gamma M_s / 2\pi$. Therefore, STOs with perpendicular polariser are of great interest for applications, due to their very large tuneability. Moreover, the frequency is varied by tuning only the current, since no external field is required.

3.1.6 Comparison with experiment

OPP were observed [10] in STO comprising a perpendicular polariser, a planar free layer and a planar analyser. An external magnetic field was applied in order to cancel the stray field coming from the analyser. Macrospin simulations neglecting the effect of the analyser are compared to the experimental results (Figure 3.3). The material parameters are given in table 3.1

$\mu_0 M_s$	1.113 T
K_u	664.5 J/m^3
p	[0 0 1]
α	0.01
η	0.3
N_{xx}	0
N_{yy}	0
N_{zz}	1

Table 3.1: Input parameters of the macrospin simulations.

The frequency increase at low current predicted by macrospin simulations is observed in experiments. However, a lot of differences can be noticed. In the experiment, the curvature of the frequency at positive and negative currents is opposite to what is expected. Moreover, the critical currents and frequency values are also different. Finally,

the frequency measured in experiments reaches a maximum and then decreases, this is not explained by the macrospin model, but can be understood with micromagnetic simulations, as shown in the next section. The macrospin approximation is no longer valid at large current despite the very small size of the free layer (60 nm diameter).

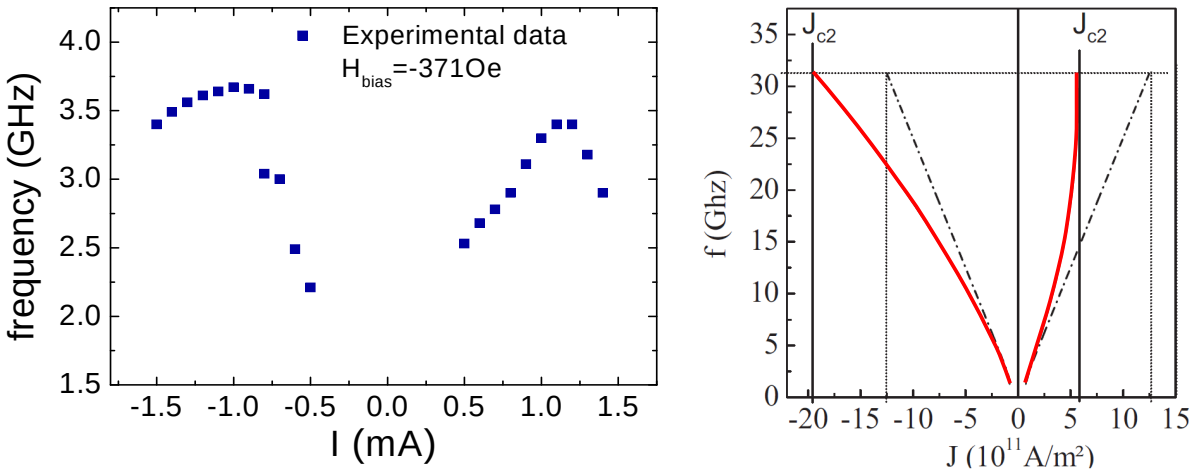

Figure 3.3: (a) Experimental results of frequency vs current (see ref [10]). (b) Macrospin simulations: frequency versus current density for a constant spin efficiency (dashed line) and an angular dependant spin efficiency (red line) (the polarisation value is $\eta = 0.3$). *Extracted from ref [105].*

Magnetisation dynamics inside a free layer of a diameter as small as 60 nm was expected to be macrospin. However, there is a very poor agreement between experiment and macrospin simulations. Micromagnetic simulations were therefore necessary to simulate the complex dynamics driven by Spin Transfer Torque.

3.2 Micromagnetic simulations: initial in-plane state

3.2.1 Finite Difference simulations

The first micromagnetic simulations of this system were performed with ST_GL-FFT by Ioana Firastrau [9]. In this section, we briefly remind the results in the case when the Oersted field is neglected as well as the stray field generated by the perpendicular polariser. The effect of the in-plane analyser is also neglected, like in the macrospin model previously presented. The free layer is divided in cells of $2 \times 2 \times 3.5\,\mathrm{nm}^3$. The input parameters of the simulations are given in table 3.2. The initial state was an in-plane uniform magnetisation along the easy axis.

The frequency f versus current density J is plotted in figure 3.4. At low current density ($-1.6 \times 10^{11} < J < 1.3 \times 10^{11}$), the frequency matches the one predicted by

A_{ex}	2×10^{-11} J/m
$\mu_0 M_s$	1.113 T
K_u	664.5 J/m^3
p	[0 0 1]
α	0.01
η	0.3
cell size	$2 \times 2 \times 3.5$ nm^3
thickness	3.5 nm
diameter	60 nm

Table 3.2: Input parameters of the FD simulations.

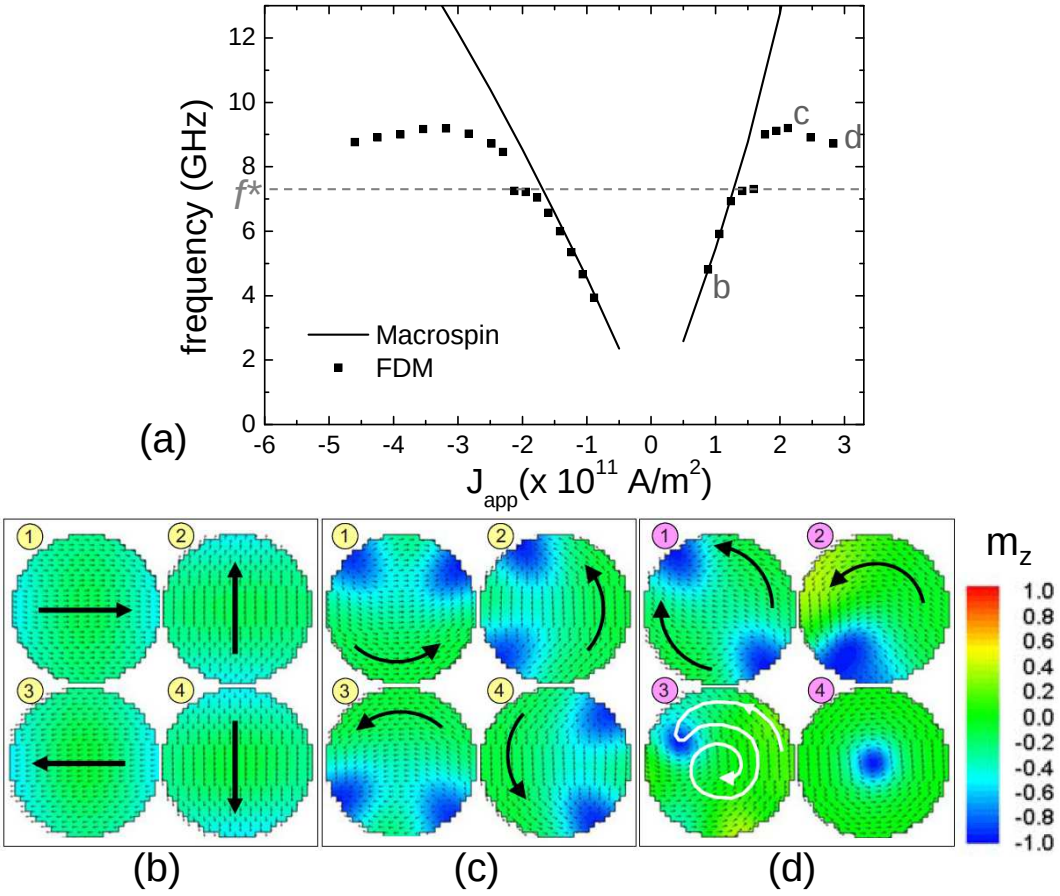

Figure 3.4: Finite Difference simulations of OPP. (a) frequency vs current density. (b) Micromagnetic configurations at low current. (b) Configurations around 2×10^{11}A/m^2. (c) Evolution when the current is increased even further: transition to a static vortex state.

macrospin whereas at higher currents ($-4.5 \times 10^{11} < J < -1.6 \times 10^{11}$ and $1.3 \times 10^{11} < J < 3 \times 10^{11}$), the frequency reaches a maximum, similarly to experiments. The micromagnetic configuration is almost uniform at very small current, which explains the good agreement with macrospin approximation. The magnetisation tends to be slightly aligned along the edge due to magnetostatic surface charges. Moreover the out-of-plane

component is larger in the two regions where the in-plane component is perpendicular to the edge. These two out-of-plane regions grow when the current amplitude is increased. A frequency discontinuity occurs at $f = f^*$, just before the plateau. The frequency jump observed was first attributed to a change to a change in the micromagnetic configuration (from (b) to (c) in the figure 3.4). This explanation is contradicted by later FEM-based simulations (section 3.2.3). At large current values, the micromagnetic configuration changes from an onion-like state to a state where the two out-of-plane domains are closer to each other. This configuration is favoured by the magnetostatic field that prevents the formation of surface charges on the edges. When the current amplitude is even larger, the two out-of-plane domains meet to form a vortex. Once the vortex is formed, it starts to move on a spiral trajectory from the edge to the centre of the free layer where it stabilises. The static vortex state is troublesome for applications because it limits the range of current and then the range of frequency.

3.2.2 Finite Element simulations

Are the frequency jumps physical or induced by the edge roughness? To answer this question, micromagnetic simulations have to be performed with a much better description of the circular boarder. Therefore, the Finite Element Method is more appropriate than the Finite Difference method for this kind of study. Micromagnetic simulations have been performed with feeLLGood. It was the first time that the STT version of the solver was tested. Therefore, the goal was also to confirm the validity of the code. In addition to being a numerical test, a complex dynamics has been studied with the discovery of new oscillation modes.

Simulations were run using the time scheme of order 1 with $du_{\max} = 0.001$. The mesh describing the circular free layer has 2083 nodes (10323 elements). It is shown on the figure 3.5. The demagnetising field is computed with the FMM method.

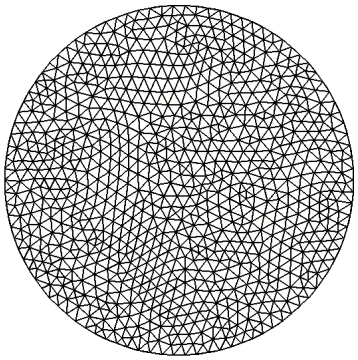

Figure 3.5: Top view of the Finite Element mesh of the simulated free layer.

The simulations were either started from an initial in-plane state or from an oscillation state already stabilised. In the latter case, the current is slightly increased (or decreased) making thus the stabilisation process much faster. The mean time of a simulation was about three weeks. To extract the frequency, the transient regime was removed and

the Fast Fourier Transform was performed on more than 60 periods of the stabilised oscillation.

The two oscillation modes observed in the Finite-Difference simulations are also observed in the Finite Element simulations, as illustrated on figures 3.6(b)(c) and 3.6(d). The "asymmetric" mode is indeed found at large current amplitude ($2 \times 10^{11}\mathrm{A/m}^2 \leq J \leq 3 \times 10^{11}\mathrm{A/m}^2$ and $-6 \times 10^{11}\mathrm{A/m}^2 < J < -3.5 \times 10^{11}\mathrm{A/m}^2$), while the symmetric mode is found at lower current. Above $3 \times 10^{11}\mathrm{A/m}^2$ and below $-6 \times 10^{11}\mathrm{A/m}^2$, the static vortex is found. In a small range of current, each mode is possible depending on the initial state. If a simulation is run at $J = 2 \times 10^{11}\mathrm{A/m}^2$ starting from the asymmetric mode, then it remains asymmetric. If a simulation is run at $J = 2.2 \times 10^{11}\mathrm{A/m}^2$ starting from the symmetric mode, then it remains in the symmetric mode.

Once the vortex is at equilibrium, it remains stable even if the current is decreased. The static vortex can then be observed in the simulations over a wide range of currents. In fact, in practice, a vortex should not be stable in such a thin layer. It is very likely that if the thermal fluctuations were taken into account, the vortex would become unstable.

The overall agreement between feeLLGood and ST_GL-FFT is very good, especially at small current values. The limit oscillation/vortex occurs at a slightly larger current amplitude with the FEM than with the FDM, and the frequency of the asymmetric mode is also greater in FEM than in FDM. In fact, the main discrepancy is at $f = f^*$: the frequency discontinuity observed in the FD simulations is not observed with feeLLGood. Thus, the two numerical methods give very similar results except in a very small range of current. The fact that the results of both solvers are in very good agreement almost everywhere was the first confirmation that feeLLGood gives consistent results in presence of spin torque. However, a major difference exists around $f = f^*$. It seems clear that this difference is due to the choice of numerical method. Numerical solvers give approximate solutions and one has to be always cautious and critical when interpreting numerical results. Artefacts have been observed in previous studies with FDM micromagnetic solvers [6], in particular due to the staircase-like edge that replaces the rounded shape of the real sample. In reality, both methods simulate two different systems with two different shapes. A series of simulations performed with feeLLGood has explained the origin of the frequency jumps. These simulations will be presented in the section 3.2.3.

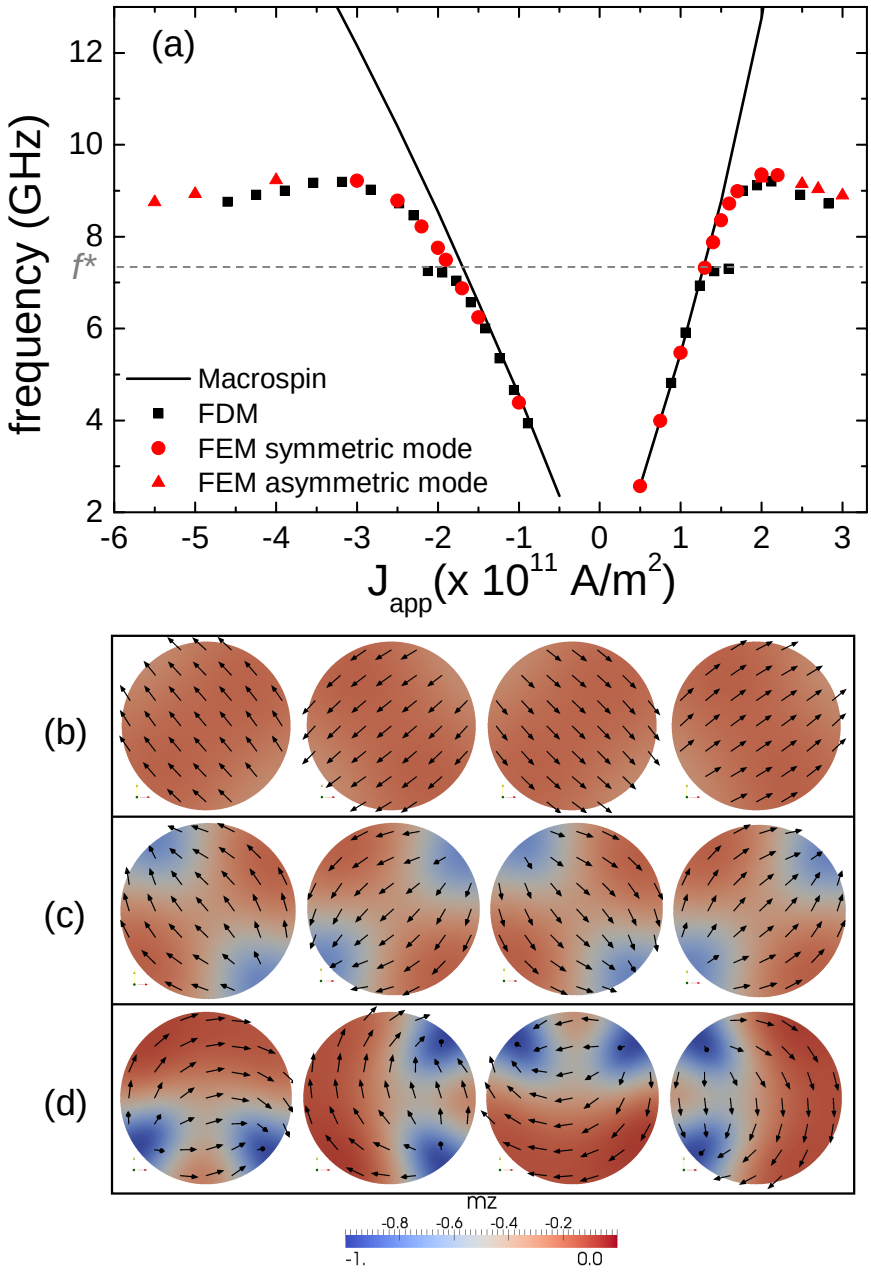

Figure 3.6: (a) Frequency versus current density of OPP. Black squares: FDM simulations. Red symbols: feeLLGood simulations; red circles: symmetric mode; red triangles: asymmetric mode. The oscillation modes are coherent rotations of a micromagnetic configuration. (b) Symmetric mode at 1×10^{11}A/m^2. (b) Symmetric mode at 2×10^{11}A/m^2. (c) Asymmetric mode at 3×10^{11}A/m^2.

3.2.3 FEM study of the frequency jump in the staircase geometry

The FDM is widely used to simulate magnetisation dynamics of circular or elliptical nanomagnets. However, very few studies [6] have been led to determine the real influence of the staircase-like edge. The discrepancy between the FDM and the FEM on the same

physical system raises this question. To solve this problem, micromagnetic simulations were run with feeLLGood with another mesh having the same edge as the staircase-like geometry in the FD simulations. This unstructured mesh is composed of 10748 nodes (57430 elements) (see figure 3.7). For a better accuracy, the elements are smaller at the edge. The protocol remains the same: the initial configuration is the uniform in-plane state and the frequency is evaluated over more than 60 stabilised oscillations. Due to the duration of the simulations, only the points close to the frequency jump are simulated.

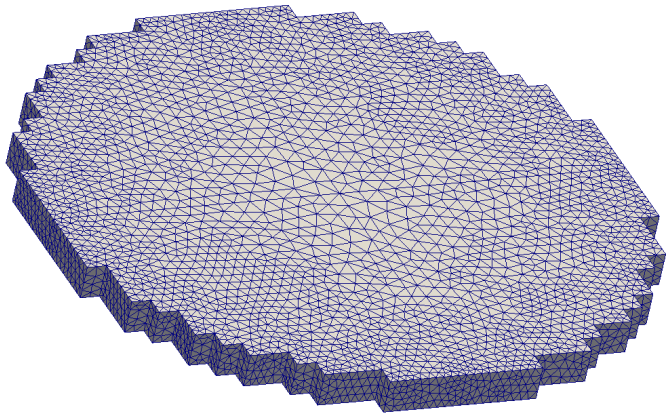

Figure 3.7: Finite Element mesh of the free layer with the staircase-like edge. This geometry is identical to the one simulated in the Finite Difference simulations.

Like in the Finite Difference simulations, a frequency jump is found, occurring at the same frequency f^* (Figure 3.8), with a very good agreement. It is interesting to take a closer look at the micromagnetic configurations. At large and small current, the micromagnetic states for the staircase geometry and the round system are the same. However, in the range of $J \in (1.3 \times 10^{11}; 1.5 \times 10^{11})\,\mathrm{A/m^2}$, one can notice, in the configurations of figure 3.8, a strong variation of the out-of-plane component. In fact, this out-of-plane oscillation, that resembles the oscillation of a membrane, was already observed in the same range of current in the FD simulations performed by Ioana Firastrau [9]. The oscillation of this "membrane mode" is exactly four times as fast as the main oscillation, as shown on the micromagnetic configurations.

Therefore, it is now confirmed that the jump in frequency is due to the staircase edge. In literature, it is sometimes affirmed that staircase-like roughness mimics the real roughness of the sample. This kind of affirmation is wrong. By replacing the circular border with a staircase-like edge, the axial symmetry is broken and replaced with a four-fold symmetry. Thus, the roughness acts as a periodic perturbation with a frequency $4f$. This perturbation creates a deviation from the ideal OPP trajectory of a circular free layer. We think that the resonance frequency of the "membrane mode" is $4f^*$. Consequently, it is excited when the main oscillation frequency is close to f^*, corresponding to the plateau observed in figure 3.8.

In conclusion, Finite Difference simulations must be interpreted with a lot of caution when dealing with circular or elliptical geometries. Using a Finite Element solver is

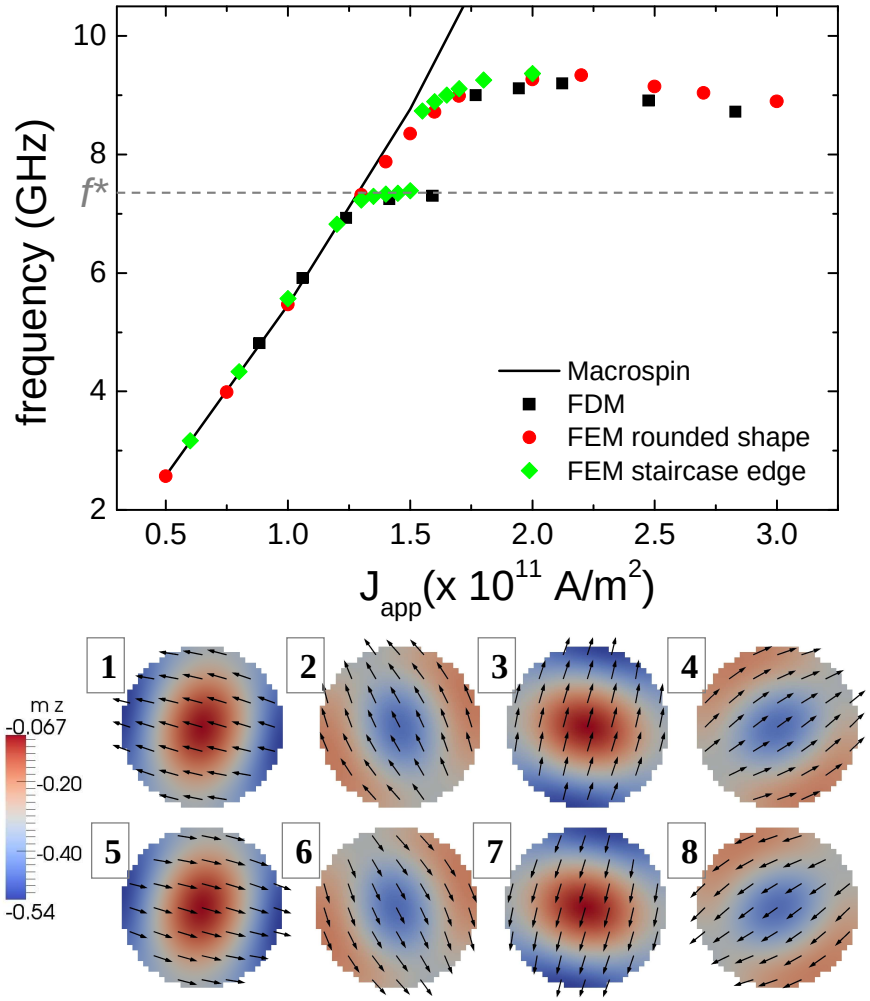

Figure 3.8: Top: frequency versus current density; the FEM simulations of the staircase geometry are in light green. Bottom: micromagnetic simulations at $J = 1.5 \times 10^{11}\mathrm{A/m}^2$ (just below the frequency jump) over one period.

therefore justified for the type of systems studied in this thesis.

So far, all the simulations had an initial in-plane state. The computed dynamics starting from these in-plane states led to two oscillation modes ("symmetric" and "asymmetric"). But are they the only modes possible in the system? Can other modes be measured in such a spin valve? To answer this question, new simulations have to be performed, starting from another state. For simplicity, the initial out-of-plane state is chosen.

3.3 Micromagnetic simulations: Initial out-of-plane state

3.3.1 Description of the modes

In this section, the new state diagram is explored in the case of an initial out-plane saturated magnetisation. Experimentally, such an initial condition could be obtained by applying a strong out-of-plane field.

With an initial uniform out-of-plane state, the evolution of the magnetisation seems to be non-deterministic: for two very close current values, the system can either evolve towards a vortex state or go into a steady oscillation mode. New oscillation modes are found, different from the "symmetric" and "asymmetric" configurations. They are shown by the blue symbols in the figure 3.9. Some of these points are obtained starting from a stabilised oscillation and modifying slightly the value of the current.

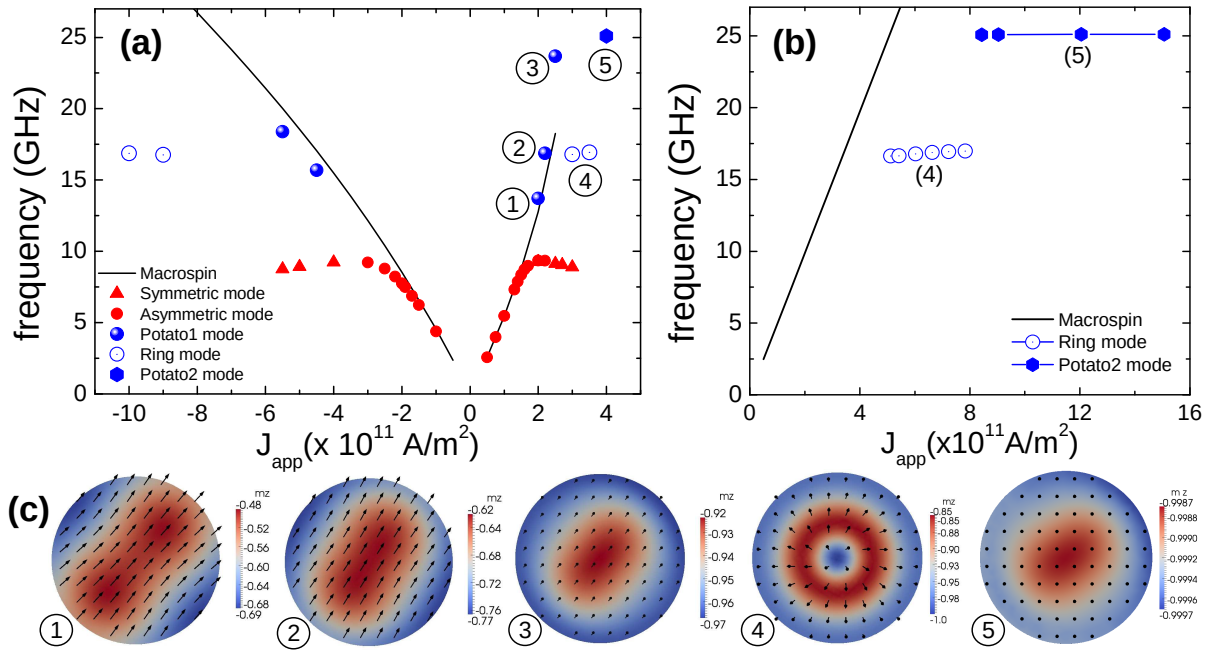

Figure 3.9: (a) Frequency versus current density of the micromagnetic simulations (symbols) and macrospin simulations (black line). Simulations performed with an angle-dependent $g(\theta, \eta)$ function. (b) Simulations performed with a constant $g(\theta)$ function. Only some simulations starting from out-of-plane state are presented. The obtained states correspond to the "ring mode" and "potato 2 mode". (c) Micromagnetic configurations of potato 1 mode (1,2,3), ring mode (4), and potato 2 mode (5).

The points "1", "2" and "3" in the figure 3.9 are remarkably situated close to the macrospin line. This is of great interest for applications, since it proves that the frequency range can be as large as in the macrospin model. It means that an oscillator combining a small size, a very large frequency tuneability, and requiring no applied field is possible.

The small deviation from the macrospin line can be explained by the non-uniformity of

the magnetisation as well as the slight inaccuracy of the demagnetisation factors. These steady oscillations are coherent rotations of the micromagnetic configurations "1", "2" and "3" presented in the figure3.9c. Like in macrospin, when the current increases, the out-of-plane component and the frequency increase. These configurations could be compared to the FMR mode (0,0) in the figure 6 of reference [106] obtained for a saturated out-of-plane state. This FMR mode is shown to have axial symmetry for a circular free layer with no magnetocrystalline anisotropy. The third micromagnetic configuration of figure 3.9c is the closest to the FMR mode since it is strongly out-of-plane. Unlike the FMR mode, the zone of maximum deviation (in red) is not circular but elliptical. For the configurations "1" and "2" of the same branch, this zone has more complicated shapes. In fact, the zone of maximum deviation is circular only for infinitesimal deviations around the out-of-plane axis. The complex micromagnetic configurations (in particular "1" and "2") arise from non-linearities and can be obtained only through numerical simulations. The mode of configurations "1", "2" and "3" was called "potato1" mode, because of the profile of m_z.

It is worth noting that the micromagnetic configuration "1" is very different from the "symmetric" mode obtained from an initial in-plane state. In fact, it is not possible to go continuously from the former to the latter by decreasing the current: there exists a small range between the two configurations where the macrospin line cannot be followed. Consequently, the frequency cannot be tuned continuously from 2GHz to 26GHz, but rather from 2GHz to 10 GHz and from 12GHz to 26GHz.

Two other modes were found, shown by the configurations "4" and "5": the "ring" mode and the "potato2" mode. They were both named after the profile of m_z in the micromagnetic configurations. The evolution of the ring mode micromagnetic configuration is shown in figure 3.10b over one period. Given the relative orientations of the magnetic moments at the edge, the ring mode seems to be the one labelled $(m = 0, \ell = 1)$ in references [106] and [104]. However, it differs by a certain "helicity": a variation of the magnetisation along the radius. The ring mode is therefore not a pure $(0, 1)$ normal mode. Furthermore, a complete analogy cannot be drawn between these simulations and the computation of eigen-modes in ref. [104] because Brown's boundary condition is implemented in feeLLGood, whereas a total pinning condition is applied in ref. [104] (see section 1.1.4).

Even though there is a large variation of the local moments with time, this mode is unlikely to be detected. Indeed, $\langle m_x \rangle$ is constant (not shown), and the amplitude of $\langle m_z \rangle$ is very small (≈ 0.015). The GMR signal due to the presence of the planar analyser and the perpendicular polariser should be therefore too weak for any possible measurement.

The last mode found in this study, called "potato2", is, according to simulations, a coherent rotation of the configuration "5" in figure 3.9. The value of $|m_z|$ is remarkably high: above 0.998 in the whole free layer. Therefore, potato 2 turns out to be a saturated out-of-plane mode, similar to the macrospin OPS state. In reality, care has to be taken when interpreting such small amplitude oscillations. The apparent precession is only generated by extremely small numerical errors. As a consequence, the potato 2 mode is

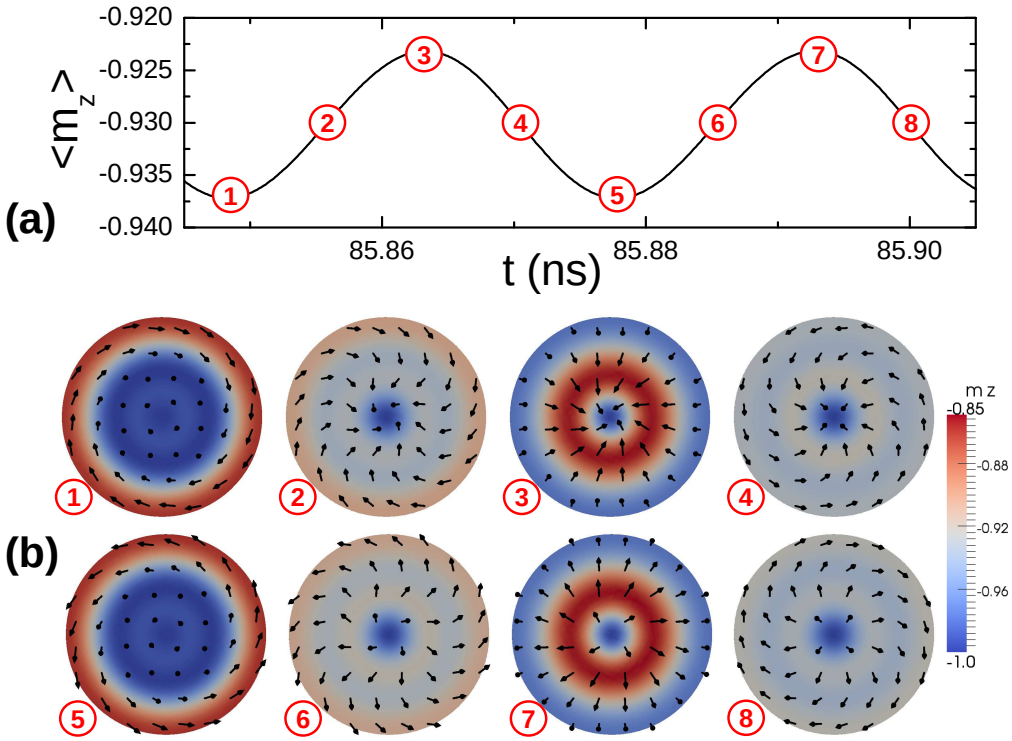

Figure 3.10: Evolution of the ring mode over one period. (b) Time trace of the out-of-plane component. (b) Micromagnetic configurations with m_z represented by the colour code.

indeed an out-of-plane stable state, identical to the one found in macrospin simulations.

3.3.2 Transitions between the modes

It was mentioned earlier that there is no smooth transition from the "potato1" mode to the "symmetric" mode. One may then wonder how the transition occurs between the potato1 mode and the ring mode. The answer is given in the figure 3.11.

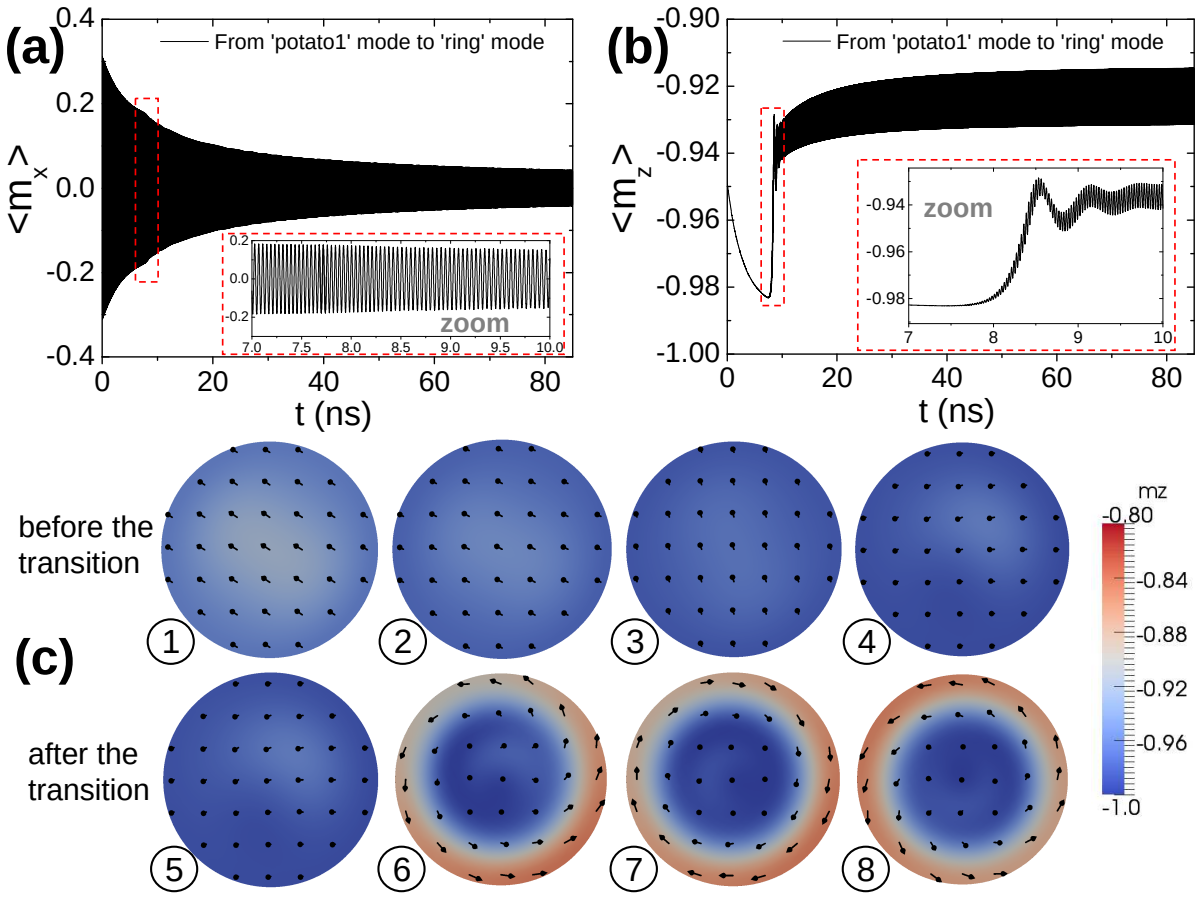

Figure 3.11: Transition from potato 1 mode to ring mode. (a) Time trace of $\langle m_x \rangle$. (b) Time trace of the out-of-plane component $\langle m_z \rangle$. (c) Micromagnetic configurations before the transition (1,2,3,4) and after the transition (5,6,7,8).

For this simulation, the current was increased from $2.5 \times 10^{11}\mathrm{A/m}^2$ to $2.7 \times 10^{11}\mathrm{A/m}^2$ starting from the stabilised potato1 oscillation. First, an increase of the out-of-plane component $|\langle m_z \rangle|$ is observed (fig3.11b), accompanied by a decrease of the m_x amplitude. Up to 8 ns, the potato1 mode continues to exist. At 8 ns, the transition from potato1 to ring mode starts. The mean out-of-plane component $|\langle m_z \rangle|$ decreases suddenly ($\langle m_z \rangle$ increases) and the frequency of the m_x oscillation decreases. Stabilisation of the ring mode is a very long process. The simulation was stopped after 85 ns and the amplitude of m_x had not yet reached zero (hence a non symmetric micromagnetic configuration in figure 3.11.b."8".

It is also interesting to look at the simulation of $J = 2.2 \times 10^{11}\mathrm{A/m}^2$ (figure 3.12) that leads to the potato 1 mode. In particular the plot of $|\langle m_z \rangle|$ exhibits three plateaus,

each of them being characteristic of one of the modes discussed previously (potato 1, ring, potato 2). The simulations starts from a uniform out-of-plane magnetisation. Until 3 ns, the system is in the potato 2 mode which has the largest out-of-plane component. Then, a transition occurs, leading to the ring mode with a typical oscillation around $\langle m_z \rangle \approx -0.93$. The corresponding micromagnetic configuration does not show clearly the ring pattern because the mode is not sufficiently stabilised. At about 7 ns, another transition occurs with an abrupt change of $\langle m_z \rangle$ followed by a sort of chaotic oscillation. Finally, the system stabilises in the potato1 mode.

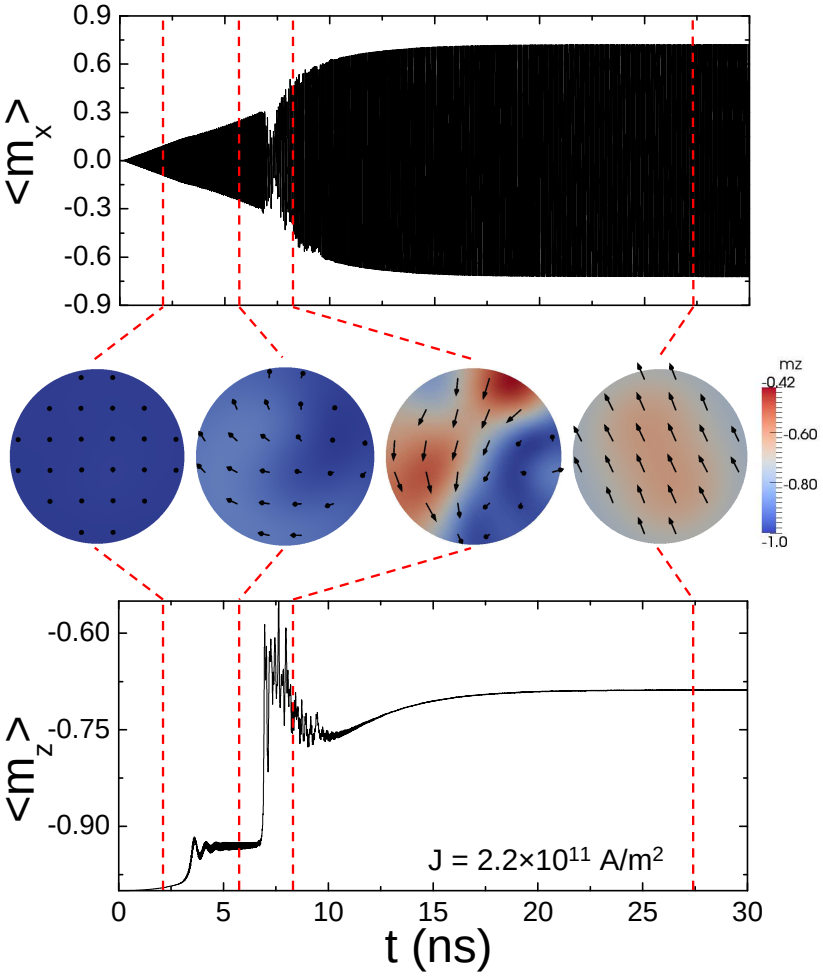

Figure 3.12: Micromagnetic simulation at $J = 2.2 \times 10^{11}\mathrm{A/m}^2$ starting from a uniform out-of-plane state.

The figure 3.13 also shows the stabilisation of magnetisation starting from a uniform out-of-plane magnetisation. The time trace of $J = 2.5 \times 10^{11}\mathrm{A/m}^2$ (in black) shows the transition to the potato 1 mode, whereas the two other curves ($J = 3 \times 10^{11}\mathrm{A/m}^2$ in green and $J = 3.5 \times 10^{11}\mathrm{A/m}^2$ in blue) lead to the ring mode. Final micromagnetic configurations are shown on the right-hand side. Interestingly, at $J = 3.5 \times 10^{11}\mathrm{A/m}^2$, the transition to ring mode occurs after 75 ns. The duration of the stabilisation process shows the necessity of running some simulations for a very long time.

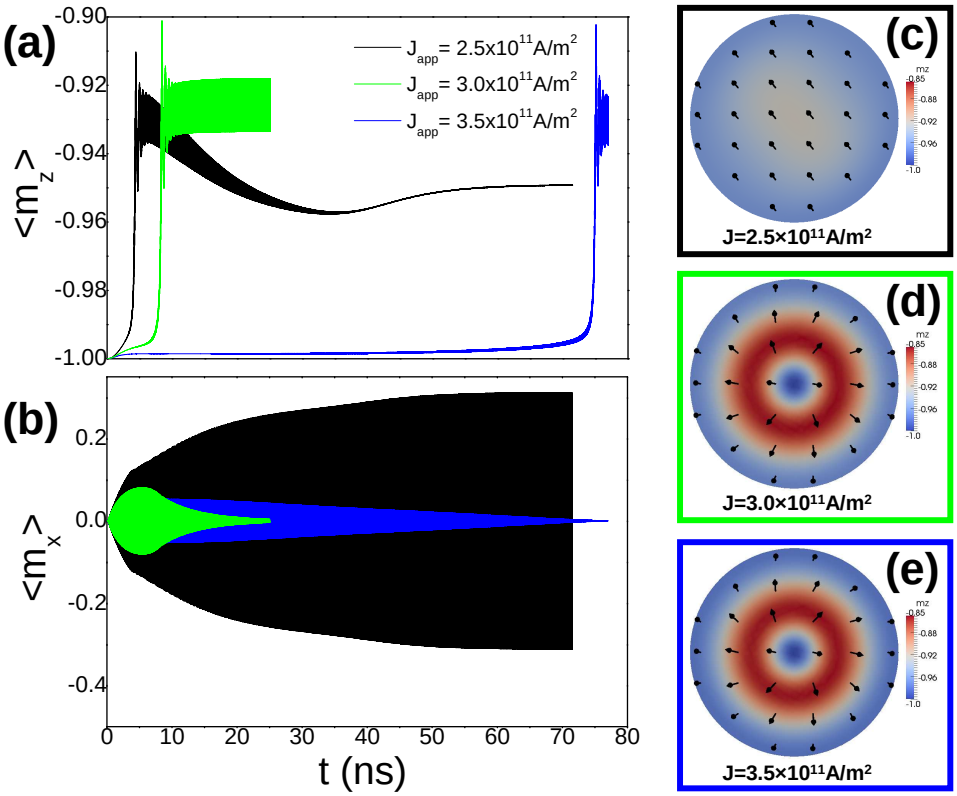

Figure 3.13: Three simulations starting from a uniform out-of-plane state: $J = 2.5 \times 10^{11}\text{A/m}^2$ (black), $J = 3.0 \times 10^{11}\text{A/m}^2$ (green) and $J = 3.5 \times 10^{11}\text{A/m}^2$ (blue). (a) $\langle m_z \rangle$ vs time. (b) $\langle m_x \rangle$ vs time. (c) Configuration of the potato 1 mode. (d,e) Configuration of the ring mode.

3.3.3 $\langle m_z \rangle$ vs J

In macrospin, frequency and $\langle m_z \rangle$ are proportional. In micromagnetism, the relationship is more complicated. The mean values of m_z (over the magnetic volume and over time) are plotted in figure 3.14 for an angular dependent $g(\eta, \theta)$ function (fig 3.14a) and for a constant $g(\eta)$ (fig 3.14b). On the red branch (initial in-plane state), at low current, $|\langle m_z \rangle|$ increases with the current, following macrospin. The curvature is only due to the variation of $g(\eta, \theta)$. At larger current, one can see that the asymmetric mode is clearly linked to a limit of $\langle m_z \rangle$. The ring mode has an averaged m_z of about -0.93 as seen previously, and the potato2 mode is almost saturated with $|\langle m_z \rangle| > 0.99$. For the static vortex state, $\langle m_z \rangle = 0.13$. The potato 1 mode exhibits an increasing out-of-plane component when the current is increased. It is clear, from fig 3.14, that the potato 1 branch stops when $|\langle m_z \rangle|$ reaches 1. Moreover, the large out-of-plane component of potato 1, ring and potato 2 modes accounts for the large frequency observed in figure 3.9.

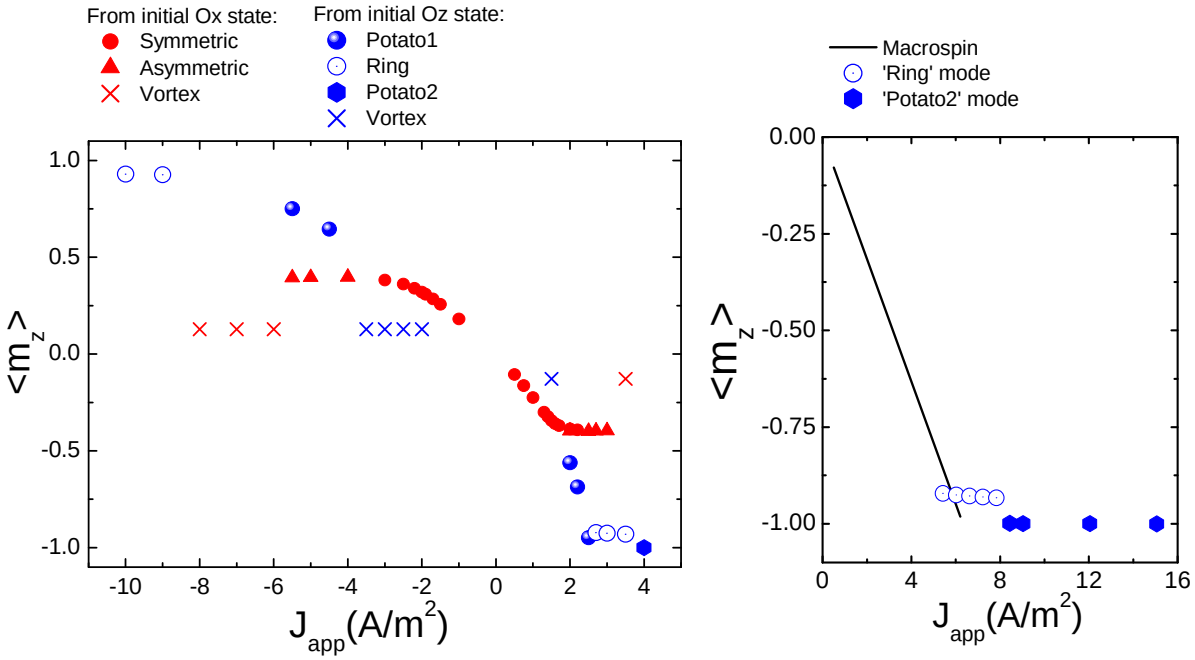

Figure 3.14: $\langle m_z \rangle$ vs current density for angular-dependent $g(\theta, \eta)$ function (left-hand side) and for constant $g(\theta)$ function.

3.3.4 Energies

The averages of exchange, demagnetising and total energies are plotted in figure 3.15.

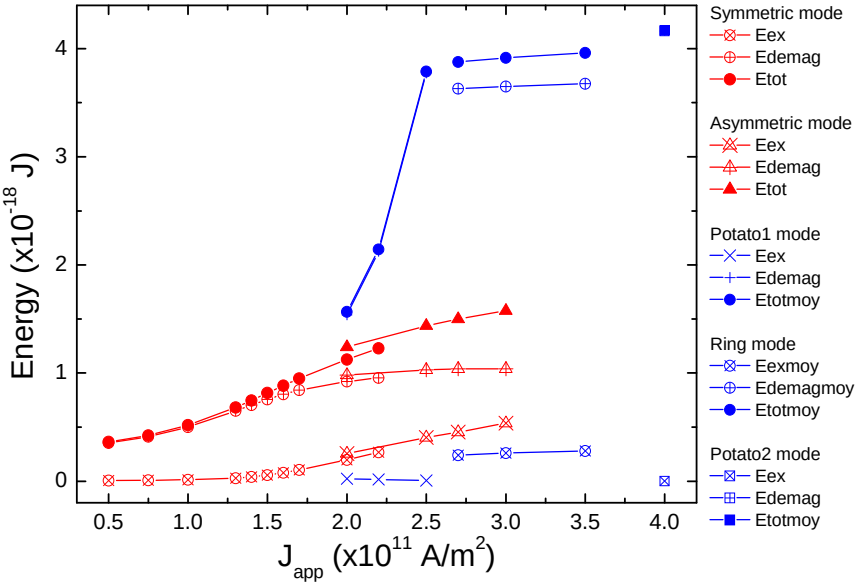

Figure 3.15: Exchange, demagnetising, and total energies of the oscillation modes for an angular-dependent $g(\theta, \eta)$ function.

For the modes obtained from an initial in-plane state, the figure shows that, at small

current, the exchange energy is almost zero, the dipolar energy being almost equal to the total energy. This observation is in agreement with the macrospin-like behaviour at small current. Indeed, from $J = 1.4 \times 10^{11}\mathrm{A/m}^2$, the exchange energy starts to increase, corresponding to a micromagnetic frequency starting to separate from the macrospin frequency (fig. 3.9). At the transition between symmetric and asymmetric mode, all the energies are almost continuous, explaining the smooth transition on the frequency curve.

Concerning the oscillations obtained from an initial out-of-plane state, the exchange energy of the potato 1 mode is almost zero, the total energy arising solely from the dipolar interaction. Similarly to the observations on the symmetric mode energies, the variations of potato 1 energies are in agreement with the macrospin-like behaviour previously reported on the $\langle m_z \rangle$ plot (figure 3.15) and the frequency plot (figure 3.9). For the ring mode, the main contribution to the total energy come from the magnetostatic interaction, due to the large out-of-plane component; the exchange energy from the spatial variations shown in figure 3.10. The total energy of the "numeric mode" potato 2 is only due to the dipolar energy coming from the saturated out-of-plane component.

3.4 Conclusions of the chapter

The conclusions of this chapter are of interest for both numerics and applications.

Numerical aspects

feeLLGood order 1 has been tested and has proved to be very reliable. Simulations are slow (about three weeks per simulation) but accurate. A significant difference has been found between Finite Difference simulations and feeLLGood simulations: the existence (or not) of a frequency jump. Performing the simulations of the staircase geometry mesh with a tetrahedral FE mesh, the jump has appeared again, demonstrating thus that it was induced by the staircase-like edge.

Applications

Two new modes have been found, the potato 1 and ring modes (potato 2 being due only to a numerical artefact). The ring mode is unlikely to be detected experimentally, but the potato 1 mode is of major interest for applications. Indeed, it follows the macrospin curve, allowing thus a very large frequency tuneability. The absence of external magnetic field makes the applicative interest even more important.

Chapter 4

STT precessional switching

Contents

In this chapter, the concept of precessional switching will be first introduced. This type of switching requires the application of a pulse (of current in the case of STT). It may enable future MRAM generation to be extremely fast (switching in less than 1 ns). Two experiments demonstrating STT precessional switching will be presented. Switching probability has been improved at the second experiment. To verify if the enhanced reliability of the device is due to the absence of polariser stray field, simulations have been performed with ST_GL-FFT. They are then compared to feeLLGood simulations

in order to check the accuracy of both solvers. In all the simulations, influence of the analyser has been neglected because it needs to be small for precessional switching. In the last part, its effect is taken into account in a macrospin approach. Thus, a more reliable switching (called *deterministic switching*) may be possible, with switching times only slightly larger than in the precessional case.

4.1 State of the art

4.1.1 Field-induced precessional switching

In first MRAM generations, the switching field is applied along the easy-axis; the aim is to have only one energy minimum, which is a global minimum. The trajectory of the magnetisation in such a device can be considered as quasi-static, i.e. it follows a trajectory of minimum energy states. This description holds within macrospin approximation, considering the damping torque as prevailing. In contrast, micromagnetic simulations show that the switching is accomplished via domain-wall motion (see NIST standard problem No. 4, section 1.3.3).

However, this method is not the most efficient in terms of energy consumption, speed and selectivity. Switching without ringing, sometimes called *ballistic switching* can be achieved using a pulsed transverse field, as illustrated by figure 4.1. The magnetisation, initially lying along the easy axis, is pushed out of the plane by the applied field. A strong demagnetising field is created, approximately equal to $-M_z$, inducing a precession about the z axis. Once the magnetisation has passed the hard axis, the pulse is stopped, and the relaxation occurs in the direction opposite to the initial state. An additional field along the easy axis can be applied at the end of the pulse to avoid ringing and terminate the motion.

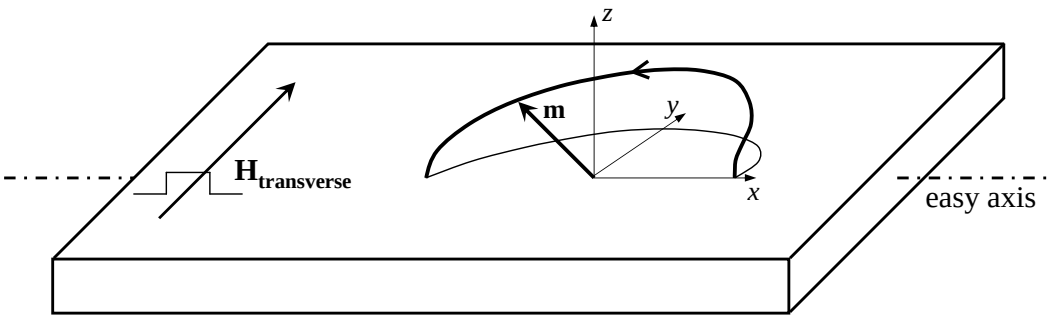

Figure 4.1: Schematic representation of field-induced precessional switching. A pulsed transverse field $\mathbf{H}_{\mathbf{transverse}}$ pushes the magnetisation out of plane, creating a demagnetising field about which $\mathbf{m}$ precesses. When the pulse has the right duration, half a precession cycle is achieved, reaching thus the physical limit of ultrafast switching. Ringing around the final direction can be avoided if an additional field is applied for example.

First experiments of field-induced precessional switching were reported in 2002 [107, 108, 109, 110]. Gerrits et al. [107] measured the reversal in 200 ps utilizing Magnetisation-induced Second Harmonic Generation (MSHG) and Magneto-Optical Kerr Effect (MOKE). They observed a "high degree of coherence" and used a quenching field to suppress ringing at the end of the pulse. Kaka et al. [108] varied the pulse length from 325 ps to 230 ps. They observed a high switching probability at 230 ps, suggesting it is the right duration to achieve half a precession cycle. Schumacher et al. [109] demonstrated quasi-ballistic reversal in 165 ps by time-resolved magnetotransport. The required energy was 27 pJ. Similar experiments [110] showed precessional switching with 140 ps pulses, at an amplitude below the in-plane hard-axis anisotropy field, i.e. below the quasi-static switching threshold. An energy as low as 15 pJ was needed to reverse the magnetisation.

Analytical equations of field-induced precessional motion were derived by Serpico et al. [111] within macrospin approximation. Even though this reversal mechanism is undoubtedly more coherent than quasi-static switching, Hiebert et al. [112] showed by time-resolved magneto-optical Kerr microscopy that it cannot be considered as macrospin and still requires micromagnetic simulations.

4.1.2 Spin-torque-induced switching in all-planar structures

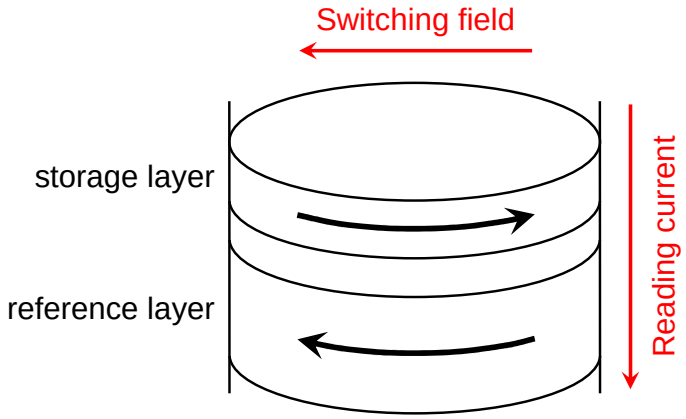

Figure 4.2: All-planar MRAM. An in-plane easy-axis field is applied to reverse the magnetisation. A current is sent to generate a magnetoresistance signal for reading.

First demonstrations [45, 4, 46, 47, 48, 49, 50] of spin-transfer switching were achieved with in-plane magnetised layers (Fig. 4.2). However, the switching process was shown [49, 113] to be stochastic and very dependent on thermal fluctuations. A random ns-scale incubation time was observed before the reversal. Indeed, the STT is zero as long as the magnetisation in the storage layer and the reference layer remain exactly parallel or antiparallel. Macrospin calculations [88] demonstrated, that the switching speed is proportional to $|I - I_c| \ln(\theta/\theta_0)$, where I_c is the critical current, θ is a constant and θ_0 is the initial misalignment between the spin polarisation and the free layer magnetisation. In the case of parallel (or antiparallel) layers, the misalignment is initiated by thermal

fluctuations, hence the stochasticity. To obtain a switching probability of 100%, a pulse of several nanoseconds is therefore needed, although the switching process in itself lasts less than 1ns. Li and Zhang [114] confirmed this explanation by micromagnetic simulations including temperature. They showed that a precession with increasing amplitude occurs prior to the reversal. Experimental results [94, 115, 116, 117] agreed with this prediction.

Several solutions were proposed to decrease or suppress the incubation delay. They all consist in giving an initial deviation θ_0 in order to make the reversal easier. In ref. [118], Devolder et al. suggested to prepare the storage layer in a precessional state by sending a dc current prior to the pulse. In ref. [119], Cui et al. showed how the combination of a microwave-frequency current and square current pulse can reduce the switching time. Using a double-pulse was also proposed to achieve a more reliable switching on the sub-nanosecond time scale [120]. Setting a non-zero equilibrium angle between the free and the pinned layer is another solution [94, 121, 122, 119], as well as applying a small in-plane hard-axis field [123, 115, 117]. However, this last method is less interesting on the technological point of view because current lines are still required.

4.1.3 Precessional switching induced by an out-of-plane polarised current

Another strategy to avoid the stochastic effects consists in adding to the planar structure a perpendicular polariser [124, 125] (Fig 4.3).

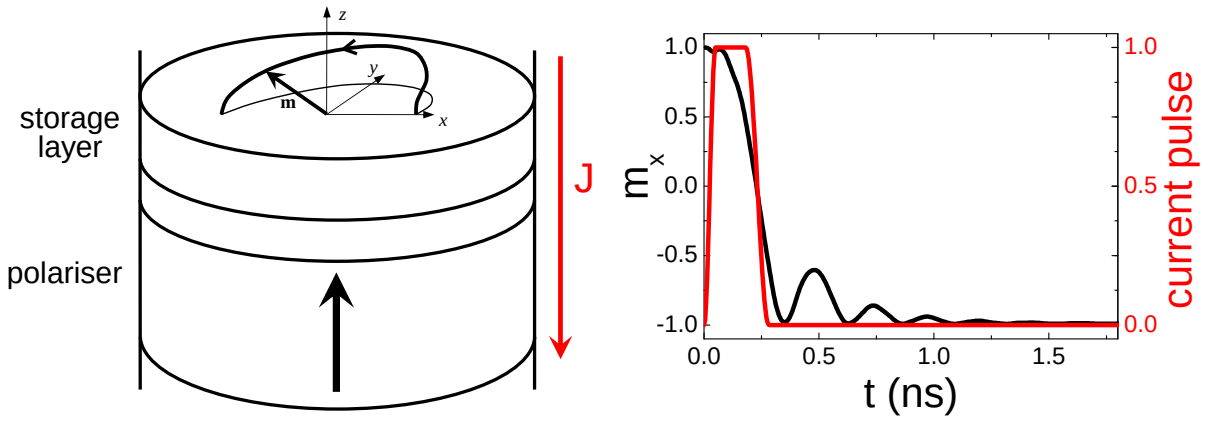

Figure 4.3: STT precessional switching. An out-of-plane precession is induced by the spin torque. The current pulse duration is adjusted such that only a half precession cycle is accomplished by the magnetisation.

In ref. [125], Kent et al. presented the concept of precessionnal switching that utilizes an in-plane and an out-of-plane polariser. The in-plane polariser ($Pol_{\parallel}$) plays a role of "analyser" by reading the magnetisation state of the FL. The out-of-plane polariser ($Pol_{\perp}$) polarises electrons that induce a precession of the FL magnetisation about the z-axis. This type of precession is called "out-of-plane precession" (OPP). The spin transfer torque from the perpendicular polariser pushes the magnetisation out of the plane,

thus creating a strong demagnetising field proportional to $-M_z$. The effective field being dominated by the demagnetising field, the magnetisation rotates about the out-of-plane axis. It relaxes along the easy axis after the end of the current pulse. Neglecting the spin-torque of the analyser, an expression of the critical current is given in Kent's article for the onset of out-of plane precession (OPP) (Equation 4.2). The reversal is very fast, since there is no incubation delay. Moreover, the switching time should depend very little on the Gilbert damping. Kent et al. suggest to apply an alternating pulse; the first half of the pulse drives the magnetisation out of the plane, and the second half returns it into the plane, thus limiting the ringing. A simple pulse is also proposed with the advantage of requiring about half of the energy and the disadvantage of a longer time to settle the magnetisation in its final state. The switching time is roughly the time to achieve half a precession cycle. For large currents, the frequency limit is $f = \frac{\gamma_0 M_s}{2\pi}$; the maximum switching time is then given by $T = \frac{1}{2f} = \frac{\pi}{\gamma_0 M_s}$. The reversal can thus occur in less than 50ps, which is two orders of magnitude faster than the switching in all-planar structures.

In ref. [126], analytical calculations and macrospin simulations are performed for dynamics with both out-of-plane and in-plane polarisers. The results of this study are of interest for spin-torque oscillators, but precessional switching in less than 50ps is confirmed. An interesting point of this article is the expression of the critical currents. In a structure with a planar polariser (Chapter 2), the onset of in-plane precession (IPP) is given by

$$J_{C\parallel} = \pm\alpha \frac{2e}{\hbar} \frac{\mu_0 M_s t}{g(0 \text{ or } \pi, \eta_{\parallel})} \left(H_K + \frac{M_s}{2} \right), \tag{4.1}$$

(given earlier in equation 2.1), while the onset of OPP induced by a $\text{Pol}_\perp$ is

$$J_{C\perp} = \pm \frac{2e}{\hbar} \frac{\mu_0 M_s t}{g(\frac{\pi}{2}, \eta_\perp)} \frac{H_K}{2} \tag{4.2}$$

(given earlier in equation 3.9).

We see that in an all-planar structure, the intrinsic damping α has to be as small as possible to induce oscillations (or switching). By contrast, OPP does not require a small α, but depends mainly on the total anisotropy (shape and magnetocrystalline). In both cases, the FL needs a low saturation magnetisation M_s. For this reason, permalloy $Ni_{80}Fe_{20}$ is commonly used. Moreover, the smaller the thickness, the smaller the critical currents. In most STT-switching devices, the thickness t is about 3nm. Note that the anisotropy field H_k and the thickness t are directly connected to the thermal stability, since the condition $KV/k_BT > 40$ is equivalent to

$$H_k t > \frac{80 k_B T}{\mu_0 M_s A}, \tag{4.3}$$

where A is the cross-sectional area. For precessional switching, one wants to lower $J_{C\perp}$ by decreasing H_k and t, but this will affect thermal stability. For applications, a trade-off is to be found between a large thermal stability and a small critical current. Finally,

the only parameter left, which allows a smaller critical current without affecting thermal stability, is the spin polarisation $\eta_\perp$. A large spin polarisation is always beneficial.

A comprehensive numerical study, carried out by Nikonov et al.[127] compared switching in four different structures, all including an in-plane free layer, but differing in the polariser angle. Out-of-plane polariser, 0° in-plane polariser, 90° in-plane polariser and 135° in-plane polariser were considered in the micromagnetic and macrospin simulations. The out-of-plane polariser turned out to be the best option in terms of speed and energy. A Gilbert damping of 0.03 gave a wider switching stripe than $\alpha = 0.01$ without affecting the critical current. The field-like torque was added, but had no particular effect on the switching diagram of the perpendicular structure.

The first experimental demonstrations of the precessional switching were achieved in 2009 [128, 129]. Lee et al.[128] observed the switching in spin-valves of $\sim 70 \times 180\text{nm}^2$ with pulses <200ps. Papusoi et al.[129] measured the switching probability $\mathcal{P}_{switch}$ as a function of the pulse duration for several current values. Sub-100ps ST precessional switching is reported. The structure of the sample was $\text{Pol}_\perp$/Cu/FL/Cu/$\text{Pol}_\parallel$, where $\text{Pol}_\perp$ is the perpendicular polariser consisting of Pt 20/(Co 0.55/ Pt 0.25)$_{\times 5}$/Co 0.8/Cu 0.3/Co 0.8, FL is the free layer comprising $Ni_{80}Fe_{20}$ 3/Co 0.5, and $\text{Pol}_\parallel$ is the planar polariser made up of Co 3/$Ir_{20}Mn_{80}$ 5 (all the thicknesses are in nm). An in-plane field is applied to cancel the stray field from the planar polariser. The switching probability curves show that the reversal is favoured for $P \rightarrow AP$, certainly due to the asymmetric ST from $\text{Pol}_\parallel$. Assuming a perfectly coherent and deterministic precessional motion, one should expect a switching probability $\mathcal{P}_{switch}$ oscillating between 1 (final state opposite to initial state) and 0 (final state identical to initial state) when the pulse length is varied. However, this is not the case (Figure 4.4), the oscillation is very damped, and barely two precession cycles are observed before $\mathcal{P}_{switch}$ vanishes to 1/2. This loss of coherence can be ascribed to thermal fluctuations and Oersted field responsible for incoherent dynamic motion. Results of macrospin simulations were also presented in this reference. They confirm analytical predictions [125, 126] that the switching speed increases with the current, but they also show the influence of the $\text{Pol}_\perp$ spin torque, in good agreement with experimental data.

More recently, switching was observed [130] with 500ps pulses in a nanopillar comprising $\text{Pol}_\perp$/Cu/FL/MgO/$\text{Pol}_\parallel$. However, in these experiments, a field was applied close to the coercive field in order to make the reversal easier.

An all-planar MgO tunnel junction and a double MgO tunnel junction were compared for switching in ref.[131]. Precessional reversal was achieved with write times of 120ps and write energies of 0.4pJ. The perpendicular structure allows 8-fold write time reduction and 3-fold write energy reduction in comparison to the all-planar junction. However, if Cu were replacing MgO between the perpendicular polariser and the free layer, the write energy could be as low as 0.1pJ according to the author.

Lee et al.[132] also observed precessional switching in very elliptical $50 \times 170\text{nm}^2$ samples with a high probability for pulses of 50ps and 100ps.

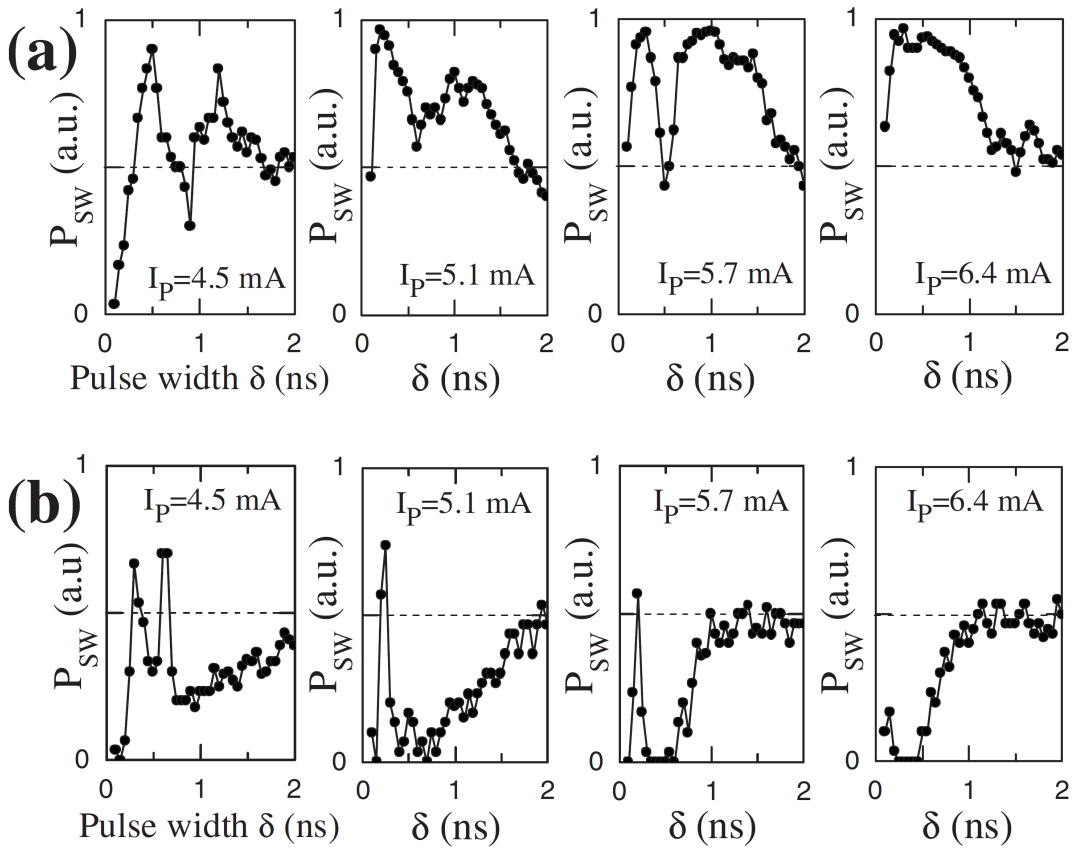

Figure 4.4: *Extracted from ref.[129].* Switching probability versus pulse length for several current values. $\mathcal{P}_{switch} = 1$ means switching was observed in 100% of the measurements. $\mathcal{P}_{switch} = 0$ means final state was always identical to initial state. (a) $\mathcal{P}_{switch}(P \rightarrow AP)$. (b) $AP \rightarrow P$

In the following, we will present results of an other experiment performed in Spintec showing more oscillations of the switching probability as a function of pulse duration. Simulations are then performed to understand the effect of the dipolar field generated by the polariser on the dynamics.

4.2 Comparison between experiment and simulation

STT precessional switching turns out to be one of the fastest and most energy-efficient process to reverse magnetisation. STT-MRAM utilising both in-plane and out-of-plane polarisers along with a planar free layer may then replace present SRAM and DRAM memories. Nevertheless, a major issue remains: the lack of reproducibility. Indeed, as shown on Figure 4.4, the switching probability does not reach 100% at short current pulses. It means that the time to complete half a precession cycle slightly varies. As it was said before, a perfectly deterministic dynamic motion would end up in a switching probability taking alternatively the value 1 or 0. Randomness is obviously due to thermal fluctuations, but it can be enhanced by a complex non-uniform magnetisation dynamics

for instance. A possible explanation for the lack of reproducibility, which is invoked in ref.[129], is the Oersted field. One would like to reduce this field for technological applications. It is possible by decreasing the current or the lateral size of the nanopillar, but this is not always feasible since a minimum current is required for OPP, and the lateral size is limited by photolithography techniques. Another possible reason for the lack of reproducibility is the influence of stray fields from the polarisers. In ref.[129], an in-plane field was applied to cancel the dipolar field from $\text{Pol}_{\parallel}$. In reality, it is not exactly compensated everywhere in the FL, since it is non-uniform. In fact, a much stronger external field was remaining: the $\text{Pol}_{\perp}$ stray field. In order to check its effect on the switching probability, a new device was fabricated by Cristian Papusoi in Spintec. Macrospin and micromagnetic simulations were then performed to understand these results. Ref.[11] summarises this study.

4.2.1 Experiment

The stack grown in Spintec is $\text{Pol}_{\perp}$/Cu 4/FL/Cu 4/$\text{Pol}_{\parallel}$, where $\text{Pol}_{\perp}$ is [Pt 15/(Co 0.5/Pt 0.4)$_{\times 7}$/Co 1/Ru 0.9/(Co 0.5/ Pt 0.4)$_{\times 5}$/Co 1/Cu 0.3/Co 1], FL is [Co 0.5/$\text{Ni}_{80}\text{Fe}_{20}$ 1.5/Co 0.5], and $\text{Pol}_{\parallel}$ is [Co 0.5/CoFeB 1.5/Ru 0.9/Co 2/IrMn 7] (all thicknesses are expressed in nanometers). The multilayers [(Co 0.5/Pt 0.4)$_{\times 7}$] and [(Co 0.5/Pt 0.4)$_{\times 5}$] have a strong perpendicular magnetic anisotropy because of interfacial coupling. However, the spin polarisation is small since spin scattering is large in Pt. Therefore, a "polarisation enhancement layer" [10] is included at the top of $\text{Pol}_{\perp}$. It comprises two thicker Co layers separated by Cu. The total thickness of Co and the large spin diffusion length in Cu provide a good spin polarisation. In $\text{Pol}_{\parallel}$, the magnetic layer is coupled to IrMn antiferromagnet to pin its magnetisation direction.

The main difference between this device and the one tested in ref.[129] is the structure of the two polarisers. In ref.[129], they were composed of a single layer, inducing a certain stray field experienced by the FL. In the new structure, the two polarisers are replaced with synthetic antiferromagnets (SAF), consisting of two magnetic layers antiferromagnetically coupled by RKKY interaction. The RKKY (Ruderman-Kittel-Kasuya-Yosida) interaction couples two ferromagnetic layers separated by a non-magnetic layer. This far-field interaction forces the two coupled layers to be either parallel or antiparallel depending on the thickness of the intermediate layer. Ruthenium has been widely used as a spacer because it induces a strong RKKY interaction [133]. In the SAF polarisers ($\text{Pol}_{\perp}$ and $\text{Pol}_{\parallel}$) of the investigated samples, the Ru layer is 0.9nm thick, which results in an antiparallel alignment at zero field. Furthermore, the SAFs are compensated, which means the coupled ferromagnetic layers have the same magnetic moment ($\sim M_s At$). Thus, the stray field on the free layer is very small, almost minimised, but not exactly zero since one of the magnetic layer in the SAF is closer. As a result, the hysteresis loop of the free layer is approximately centred at zero for both out-of-plane and easy-axis fields. Since in ref.[129], the $\text{Pol}_{\parallel}$ stray field was compensated by an external field, a comparison with the new structure will help to understand the effect of $\text{Pol}_{\perp}$ stray field. The aim

is to see whether the suppression of this field increases the coherence and the switching probability.

The sample has an almost circular cross-section of 100 nm diameter. The magnetoresistance is 0.3% due to the large serial resistance of the buffer and capping layers. All measurements are performed at room temperature.

During the experiment, an external field first sets the free layer magnetisation parallel or antiparallel to $\mathrm{Pol}_{\parallel}$ direction. The field was then completely switched off, and a pulse of current was sent. The rise time of the pulse was 50 ps and the fall time was 100 ps. The static resistance was measured immediately after the end of the pulse. It was always close to either the parallel or the antiparallel resistance, indicating that, at the end of the pulse, the FL magnetisation is uniform and aligned along the easy axis. The switching probability $\mathcal{P}_{switch}$ is plotted in Figure 4.5 as a function of the pulse duration. Each point is an average over 120 measurements. This plot must be compared to Figure 4.4 that was obtained for single-layer polarisers [129]. With the SAF-$\mathrm{Pol}_{\perp}$, more than five oscillations in $\mathcal{P}_{switch}$ are observed before settling at 50% probability corresponding to equal probability of ending up in P or AP configuration. In contrast, when a single-layer $\mathrm{Pol}_{\perp}$ was used, barely two oscillation periods could be observed. Furthermore, the first "peak" almost reaches unity here, indicating an improved reproducibility in the switching.

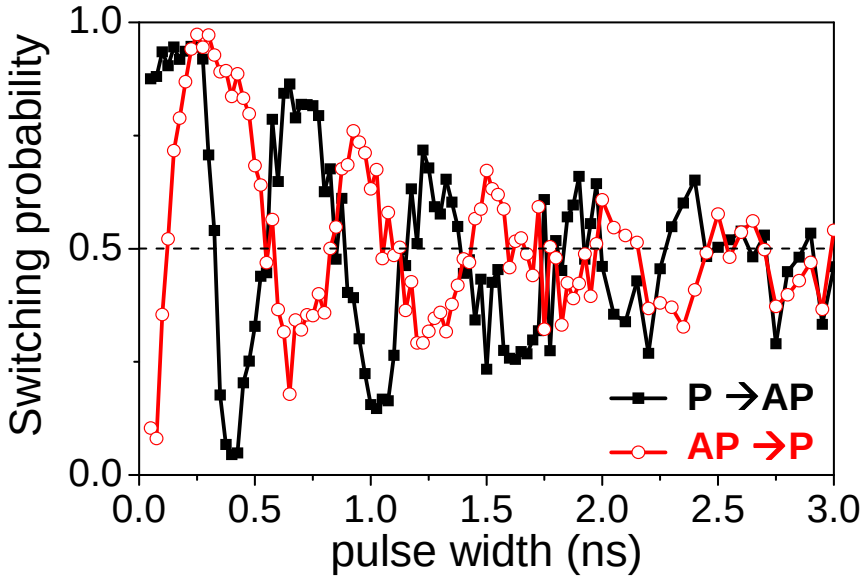

Figure 4.5: Switching probability as a function of pulse width. Squares: the initial state is parallel. Open circles: the initial state is antiparallel. The current density is $8.3 \times 10^{11} \mathrm{A/m}^2$.

The symmetry of the oscillations about $\mathcal{P}_{switch}$ shows that the magnetisation dynamics is dominated by the spin transfer from $\mathrm{Pol}_{\perp}$, and that $\mathrm{Pol}_{\parallel}$ has a negligible influence on the switching dynamics, likely due to a higher current polarisation from $\mathrm{Pol}_{\perp}$.

The coherence has been enhanced compared to the previous device. In order to check whether the suppression (or at least the dramatic decrease) of $\mathrm{Pol}_{\perp}$ stray field is the rea-

son of the enhanced reliability, micromagnetic simulations were performed. Macrospin simulations were first carried out, in order to determine a plausible set of material parameters.

4.2.2 Macrospin simulations

In macrospin simulations, the magnetisation dynamics of the FL is simulated. The Landau-Lifshitz-Gilbert equation is solved numerically with the additional Slonczewski torque. The pulse length Δt is swept between 50ps and 3ns, and the current density J is also varied. At initial state, the FL magnetisation is aligned along the easy axis; a pulse is applied with 50ps rise time, Δt duration and 100ps fall time. After the end of the pulse, the simulation keeps on running for 2ns to let the system relax. The last value of m_x (easy-axis component) is stored, providing information on the final state.

Since the influence of the $\text{Pol}_{\parallel}$ spin torque was negligible in the experiment, only the spin torque from the $\text{Pol}_{\perp}$ is implemented. The materials constituting the FL are Co 0.5/$Ni_{80}Fe_{20}$ 1.5/Co 0.5. This trilayer, in the macrospin approach, has to be modelled as one single material. A reasonable value for the saturation magnetisation is $M_s = 1040$ kA/m. The out-of-plane spin polarisation is set to $\eta_{\perp} = 0.3$, which is also a reasonable value. The other parameters of the simulation are the damping α, the magnetocrystalline anisotropy K_u, and the demagnetisation coefficients N_{xx}, N_{yy}, N_{zz}. The experimental values of these parameters are not known precisely, and therefore, can be adjusted within a reasonable range for simulation.

The first macrospin simulations were run with the parameters of table 4.1

M_s	1040 kA/m
K_u	12000 J/m^3
p	[0 0 1]
α	0.02
$\eta_{\perp}$	0.3
N_{xx}	0
N_{yy}	0
N_{zz}	1

Table 4.1: Input parameters of the first set of macrospin simulations.

This set of parameters gave a frequency much higher than the one observed in experiment, even for a current close to the critical current (we get more than 30 periods in 3ns, instead of 6 oscillations measured experimentally). Therefore, these parameters have to be adjusted to obtain a better agreement. However, looking for a perfect agreement would not make sense, because a lot of "ingredients" are not included in the model. These ingredients would likely be responsible for a substantial change in the quantitative results. Describing the whole nanopillar with a very accurate transport model could help obtaining a good agreement, but it would require even more parameters, often hard to determine. It would also lead to very lengthy simulations.

The expression of the OPP frequency [126, 105] (equation 3.15)

$$f = \frac{\gamma_0}{2\pi}\frac{\hbar}{2e}\frac{g(\theta,\eta)}{\mu_0 M_s t}\frac{J}{\alpha} \tag{4.4}$$

tells us that α could be increased to obtain a better agreement with the experiment, but $\alpha > 0.02$ would not be realistic. In fact, it also tells us that the minimum frequency is proportional to $J_{C\perp}$, therefore the expression of the critical current (equation 4.2) also indicates how to obtain a smaller frequency. Reducing the anisotropy H_k allows smaller currents to induce OPP, hence smaller frequencies. After trying several sets of parameters, the magnetocrystalline anisotropy K_u was finally set to zero, while a small in-plane shape anisotropy was given by the demagnetisation coefficients given in table 4.2 that correspond to an ellipse of 100nm×90nm×2.5nm. The other parameters remain unchanged.

M_s	1040 kA/m
K_u	0 J/m^3
p	[0 0 1]
α	0.02
$\eta_\perp$	0.3
N_{xx}	0.034702
N_{yy}	0.038709
N_{zz}	0.926589

Table 4.2: Input parameters of the final set of macrospin simulations.

Figure 4.6 shows the results of the simulations. In the black areas, the final state was identical to the initial state. On the other hand, white stripes indicate a switching. The critical current is found to be $J_{C\perp} = 1.1 \times 10^{11}$ A/m^2. The minimum switching time is given by the first white stripe on the left-hand side. It varies as the inverse of the overdrive current $|J - J_c|$, as predicted by Sun [88]. 100ps switching can be achieved at twice the critical current, while a current just above $J_{C\perp}$ requires a 500ps pulse.

The successive white and black stripes correspond to different numbers of half precession cycles achieved by the magnetisation. In the first white stripe, the magnetisation has just completed half a round; in the next black stripe, it is one precession cycle, thus returning to its initial state; in the following white stripe, there are 3/2 precession cycles, and so on. Thus, the FL magnetisation achieves an odd number of half precession cycles in a white stripe, and an even number in a black stripe.

Thermal fluctuations are not included here. The simulations are deterministic, which means running several times will always give the same result. If we wanted to compare directly these macrospin simulations with the plot of the switching probability (Figure 4.5), then we should add the temperature via a randomly fluctuating field.

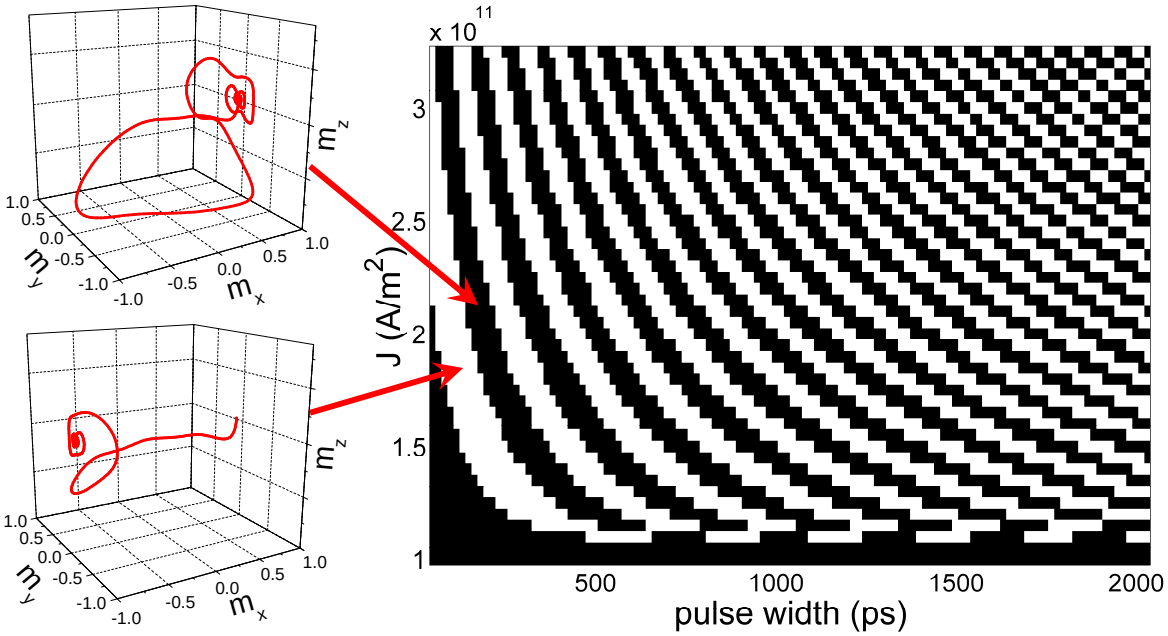

Figure 4.6: Switching probability as a function of the current density J and the pulse width Δt. White: switching. Black: no switching. On the 3D plots: magnetisation trajectories. First white stripe: half a precession cycle. First black stripe: complete precession cycle.

4.2.3 Finite-Difference simulations

Our finite difference simulations are run with the micromagnetic solver ST_GL-FFT [9]. The goal is to compare the dynamics in the cases of a single-layer $\text{Pol}_\perp$ and a SAF $\text{Pol}_\perp$. The FL is discretised in a mesh with cells of $1.6 \times 1.4 \times 2.5\text{nm}^3$. Other layers are supposed to be fixed. Like in the macrospin simulations, the $\text{Pol}_\parallel$ is ignored and the out-of-plane polarised current is modelled by the Slonczewski torque. The non-uniform $\text{Pol}_\perp$ stray field is added in the case of single-layer $\text{Pol}_\perp$, whereas no additional field is experienced by the FL with a SAF-$\text{Pol}_\perp$. Moreover, the model does not take account of thermal fluctuations.

The stray field of the single-layer $\text{Pol}_\perp$ is computed in the cells of the FL. Its intensity and its out-of-plane component are shown in figure 4.7. The stray field ranges from 61 kA/m to 130 kA/m inside the free layer. In comparison, the Oersted field (Figure 4.8) goes up to 5.8 kA/m and its average is about 4 kA/m for a typical value of the current density $J = 2.3 \times 10^{11}\text{A/m}^2$. For this reason, it will be neglected in our simulations, though its inclusion could be interesting for a further study.

Current density and pulse length are swept, like in macrospin simulations. A switching diagram (Figure 4.9), similar to figure 4.6, is plotted for the two current polarities and the two device structures. Due to a non-constant $g(\theta, \eta)$ factor in the expression of the spin torque, the diagrams for two opposite polarities are not symmetric; in particular, the value of the critical current $J_{C\perp}$ is slightly different.

Figure 4.9a should be compared with figure 4.6. In the latter, obtained for macrospin,

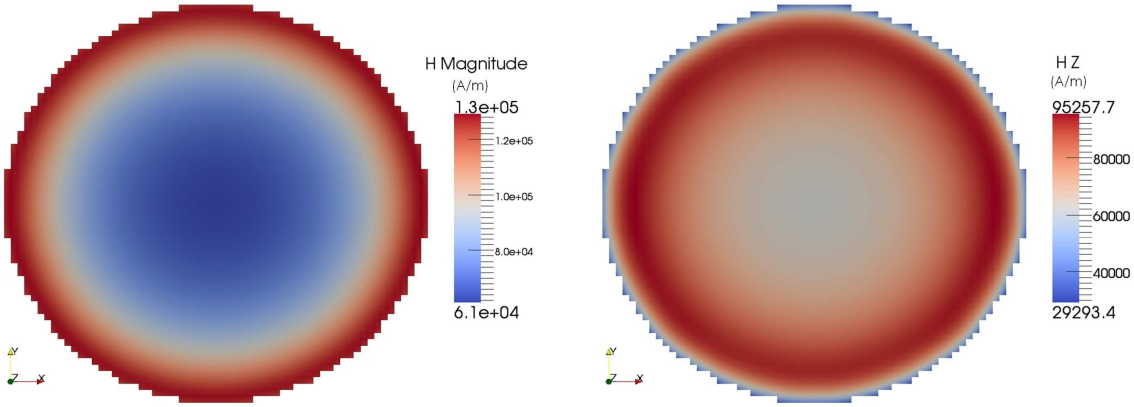

Figure 4.7: $\text{Pol}_\perp$ stray field computed inside the FL. Left-hand side: magnitude of the stray field. Right-hand side: out-of-plane component of the stray field.

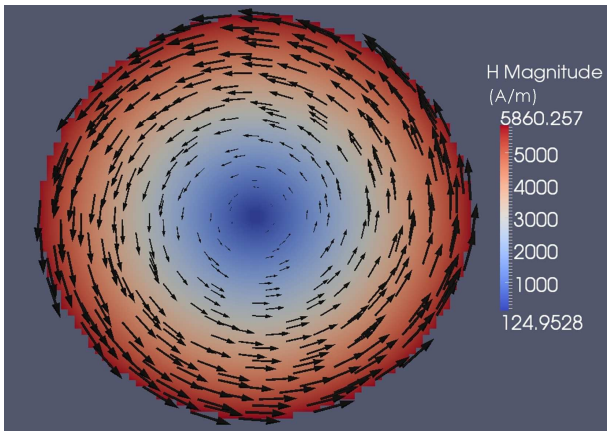

Figure 4.8: Oersted field calculated for a uniform distribution of current along $\hat{\mathbf{z}}$ of amplitude $J = 2.3 \times 10^{11}\text{A/m}^2$.

the stripes are closer to each other when the current is increased, exhibiting a monotonic increase of the frequency (equation 4.4). In contrast, figure 4.9a shows a certain frequency decrease at high current, especially after several precession cycles. This behaviour is explained by a change in the micromagnetic configuration, as shown in chapter 3 and ref.[9].

Let us now compare the diagrams 4.9cd obtained with a single-layer $\text{Pol}_\perp$ to the plots 4.9ab of the SAF-$\text{Pol}_\perp$ structure. The addition of the stray field leads to a slightly smaller critical current. At moderate current density (below $2 \times 10^{11}\text{A/m}^2$), the magnetisation is still sufficiently uniform such that the final state is a single domain aligned along the easy axis. However, at higher currents a vortex is formed, favoured by the $\text{Pol}_\perp$ stray field. The region where the final state is a vortex is shown in grey in figure 4.9.

Figure 4.10 illustrates the evolution of the system under a pulse of 1210 ps and $2.5 \times 10^{11}\text{A/m}^2$. Without $\text{Pol}_\perp$ stray field, two symmetrical canted domains move along the edge of the FL (Figure 4.10a) during the precession. When the current is switched off, the magnetisation continues to rotate, achieving a whole turn before relaxing along the

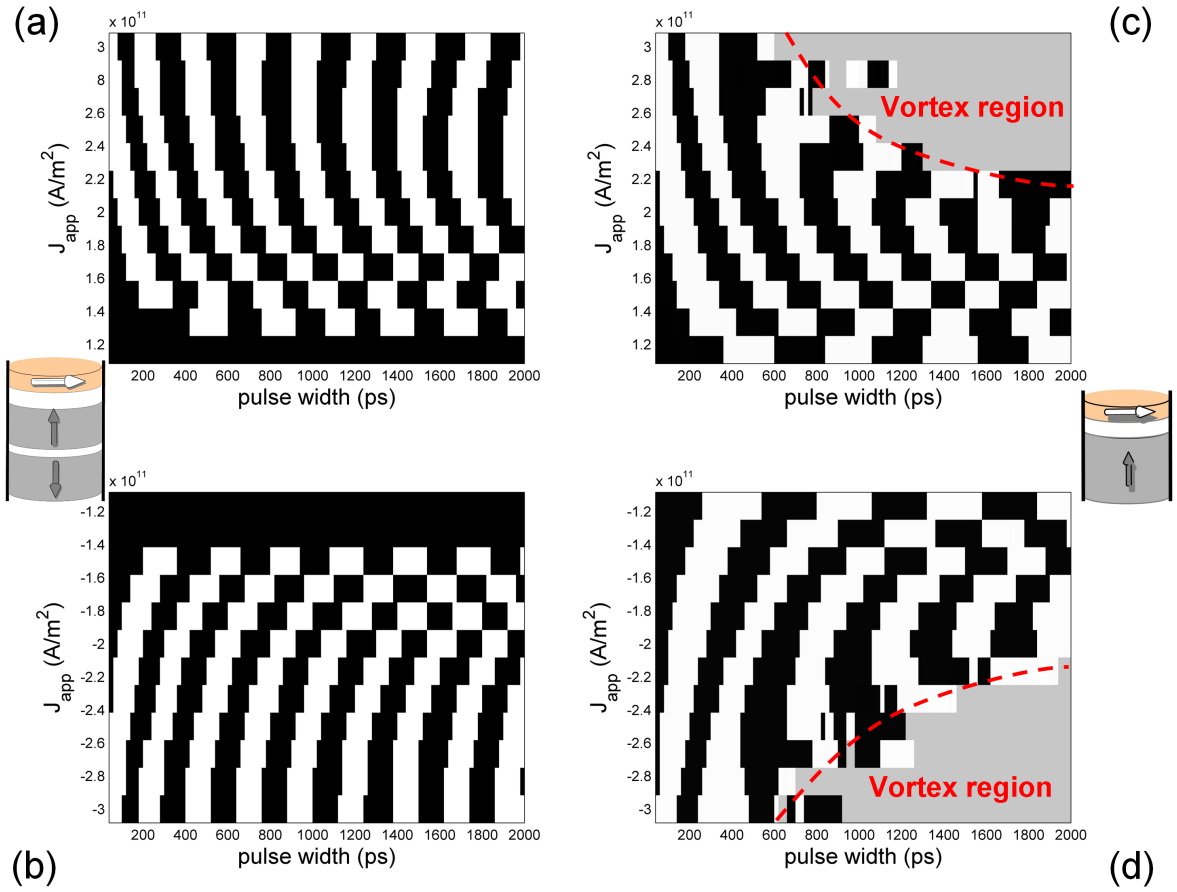

Figure 4.9: Switching diagrams obtained with FD micromagnetic simulations. Black: no switching. White: switching. Grey: the final state is a vortex. (a) J>0, no $Pol_{\perp}$ stray field. (b) J<0, no $Pol_{\perp}$ stray field. (c) J>0, stray field applied. (d) J<0, stray field applied.

easy axis. With a $Pol_{\perp}$ stray field (Figure 4.10b), the equilibrium state at the beginning is not exactly the same. When the current is on, an out-of-plane domain is formed; it is pointing downward, since the spin torque is along -z when $J > 0$. During the precession, this domain moves away from the edge, giving rise to a vortex. At the end of the pulse, if the vortex is sufficiently far from the border, it remains stable and spirals around the centre of the FL at a much slower frequency with a trajectory of gradually decreasing radius. Its direction of rotation is determined by the surrounding in-plane spins which "drags" it. The vortex is then static when it reaches the centre.

Thus, the vortex state is induced by the $Pol_{\perp}$ stray field. Since this field is directed upward, one may think that the vortex is favoured only for the current polarity making it to point up. This is wrong, as shown in the example of the figure 4.10. A vortex can be observed for both polarities of current, with a vortex pointing up for $J < 0$ and pointing down for $J > 0$. The vortex state is initiated by a complex magnetisation configuration induced by the $Pol_{\perp}$ stray field and enhanced by the STT-driven dynamic motion.

However, experiments show that the final state is one of the two in-plane equilibrium

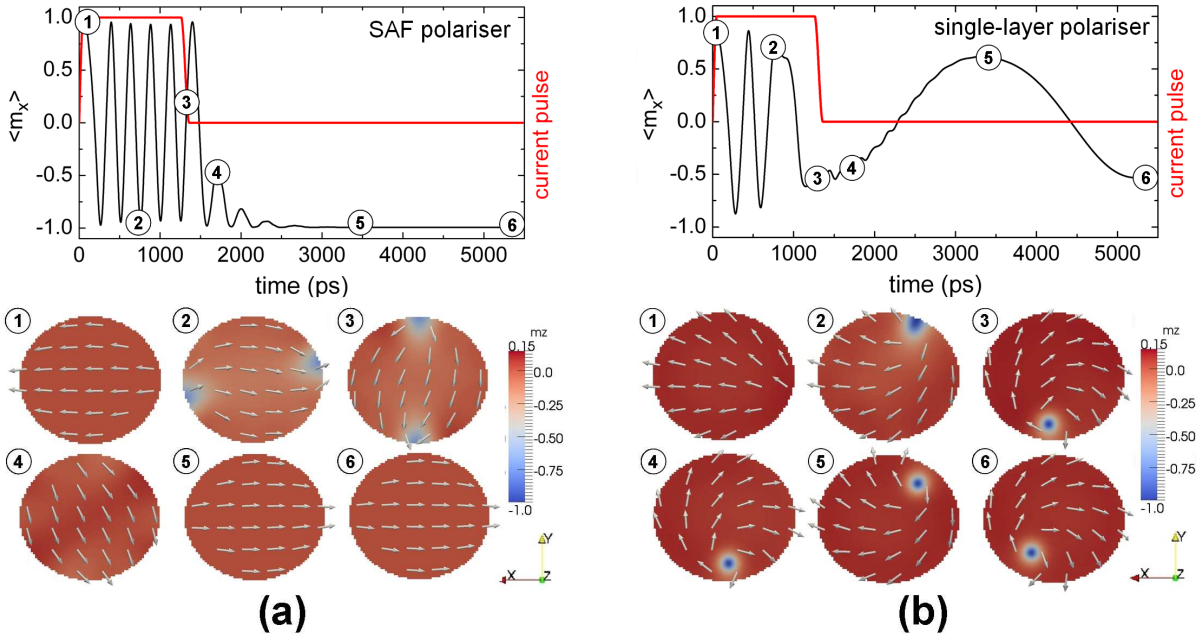

Figure 4.10: Simulations for a current density $J = 2.5 \times 10^{11}\mathrm{A/m}^2$ and pulse length $\Delta t = 1210\mathrm{ps}$ with a SAF $\mathrm{Pol}_\perp$ (a) and a single-layer $\mathrm{Pol}_\perp$ (b). The colour scale represents the out-of-plane component of the magnetisation. In (b), when the current is off, the vortex describes a spiral around the FL centre. The system is at static equilibrium when the vortex reaches the centre.

state and cannot be a vortex. In fact, the vortex is an energy minimum, but not a global minimum. Numerical computations with $\mathrm{Pol}_\perp$ stray field show that the energy differences between vortex and in-plane state are

$$E_{\text{Vortex DOWN}} - E_{\text{single-domain}} = 2.17 \times 10^4 \ \mathrm{J/m}^3$$
$$E_{\text{Vortex UP}} - E_{\text{single-domain}} = 1.81 \times 10^4 \ \mathrm{J/m}^3$$

In fact, the vortex state is stable for much thicker layers. The reported simulations are performed at 0K. At room temperature, thermal fluctuations are expected to overcome the energy barrier, such that the system would end up in one of the two in-plane equilibrium states (global minima) with equal probability. Therefore, when $J > 2J_{C\perp}$, the coherence is lost for long pulses, and the switching probability goes to 0.5, as observed experimentally.

In conclusion, the coherence of the magnetisation dynamics is affected by the $\mathrm{Pol}_\perp$ dipolar field, and leads to a rapid damping of the oscillations of switching probability as a function of pulse duration. Therefore, the use of SAF-$\mathrm{Pol}_\perp$ improves the switching reproducibility in these ultrafast switching MRAM cells. Moreover, it is interesting to note that the improved coherence of the precession likely means a correlative narrower linewidth when using this type of structure as frequency tuneable RF oscillators.

4.2.4 Switching probability and frequency noise: prospective work for experiments and simulations

Let us consider the studied device as a STO excited by a dc current. As mentioned earlier, a narrow linewidth of this STO means a better coherence. Thus, one of the reasons of the decreasing switching probability in STT-precessional switching is the frequency noise. The experimental plot 4.5 is obtained from averages over several measurements. Each measurement is the final state of an oscillation which has its own particular mean frequency, due to fluctuations. Consequently, the final state of one realisation will depend on the deviation from the true periodicity (called *jitter*) at the end of the current pulse. Therefore, the obtained probability results from the jitters of all the realisations.

Figure 4.11 illustrates this average effect. The switching probability curve of one realisation is obviously a square wave (Figure 4.11a) since there are two possible final states. For simplicity, fluctuations were not included within the realisation. Instead, to understand the effect of frequency noise, the frequency of each realisation was picked up randomly from a Gaussian distribution (Figure 4.11b) centred about $f_0 = 1.9$ GHz with a standard deviation $\sigma = 0.124$ GHz. The average of 250 realisations was then computed, giving the switching probability (Figure 4.11c).

The values of input parameters f_0 and σ were chosen to have a good agreement with experimental data of figure 4.5. Standard deviation σ is supposed to be of the same order of magnitude as $2\alpha\omega$. Given the values of σ and ω, the damping has to be around $\alpha = 0.03$, which is consistent with simulations.

No RF measurement was done on the studied STT-MRAM. An interesting experiment would be to measure the phase noise in this type of device in order to verify its effect on the coherence loss. Simulations could also be performed by varying α and temperature.

Even though frequency noise may be a good explanation for the vanishing switching probability, one can notice that the beginning of the simulated curve is much more square than in experiments. In Figure 4.11c, P_s reaches 1 in a certain range of time, which is not the case in experiments. In the model, the initial configuration was assumed to be always the same. In reality, thermal fluctuations are responsible for a certain distribution of initial states. Since the starting state is different for each realisation, one should expect different "trajectories" from the very beginning, affecting the whole curve, in particular at short time scale. Macrospin and micromagnetic configurations could be used to study the effect of an initial state distribution on the switching probability at half a precession cycle, which is particularly interesting for applications. For example, including the fluctuating field, one can let the system evolve without current, and start the pulse after 0.2ns. Performing this simulation 100 times, P_s can then be plotted. A broad distribution of initial states induced by the temperature should lead to a smaller probability at half precession cycle.

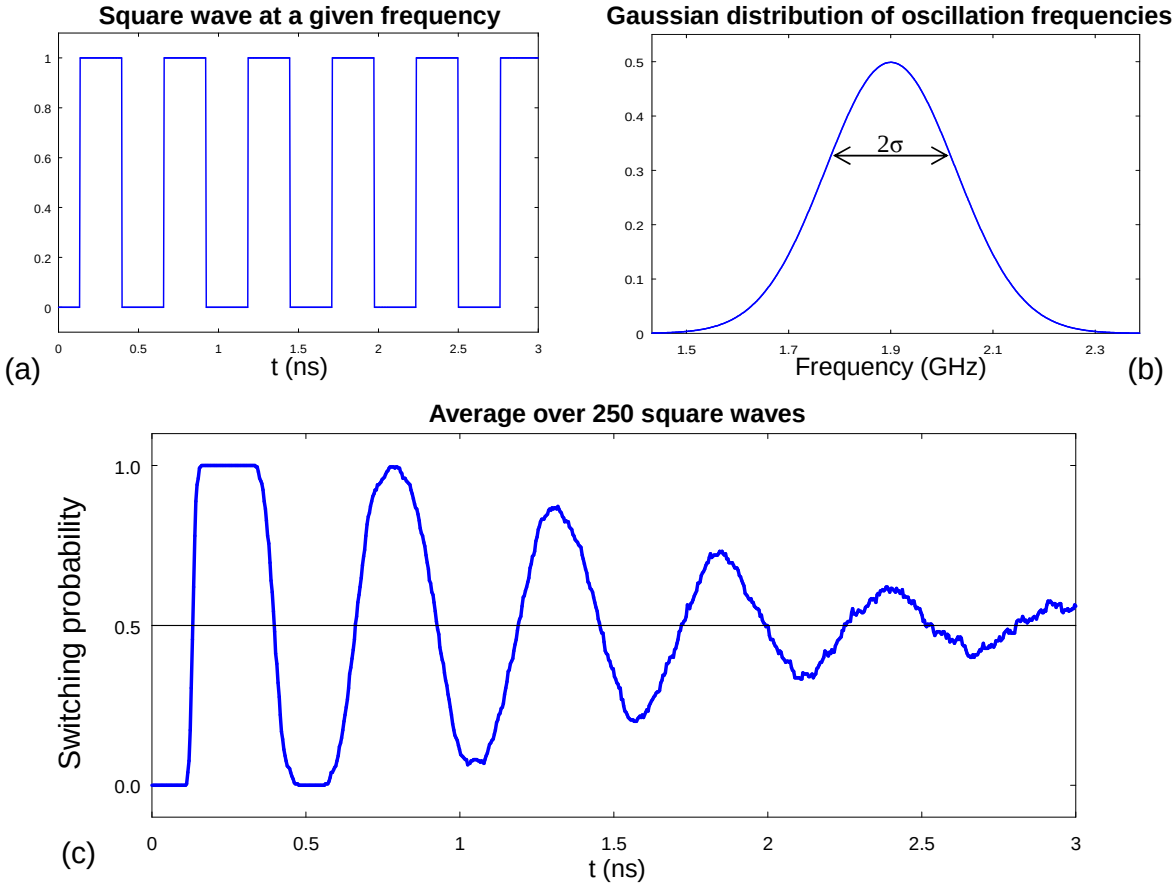

Figure 4.11: (a) Square wave representing one realisation. (b) Gaussian distribution of square waves frequencies with mean parameter $f_0 = 1.9\,\mathrm{GHz}$ and standard deviation $\sigma = 0.124\,\mathrm{GHz}$. (c) Average over 250 square waves.

4.2.5 Finite Element simulations

Comparison of switching diagrams

All the micromagnetic simulations that we have reported in ref.[11] were performed with the Finite-Difference code ST_GL-FFT. To test feeLLGood, simulations of STT precessional switching were also performed, using the order 2 version of the code and $du_{max} = 0.015$. The demagnetising field is computed with the FMM method. Each diagram required less than two weeks of simulations, thanks to the large number of CPUs used at the same time. The mesh contains 5368 nodes (27405 elements). The results are shown in figure 4.12. This figure has to be compared with the figure 4.9. Let us just remind that the simulated systems are not exactly the same, since the edge is not 'rough' in FEM simulations. This accounts for some difference in the results, as shown in the next section.

The agreement between feeLLGood and ST_GL-FFT simulations is very good. Almost identical results are obtained at low currents. In the single-layer-Pol$_\perp$ case, the vortex state is found in the same range of pulse length and current. Even the 'incursion' at

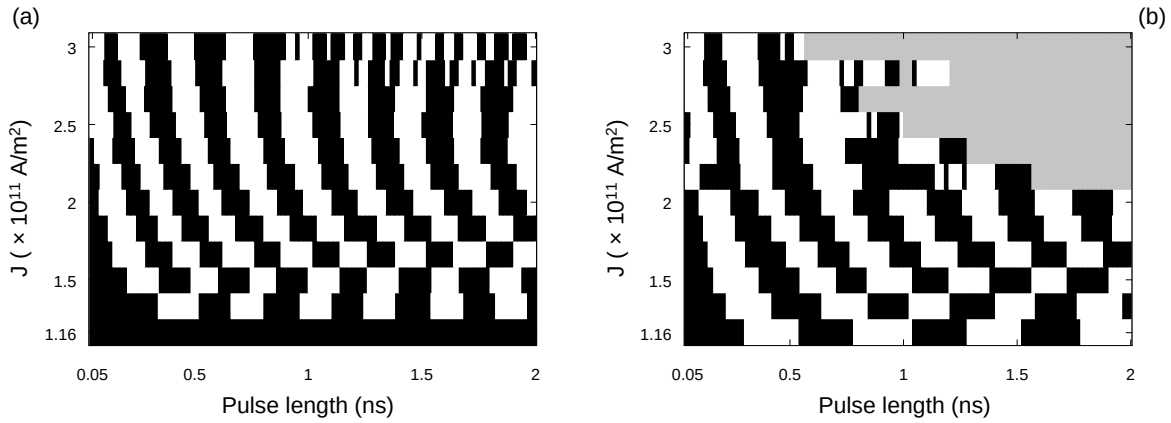

Figure 4.12: Switching diagrams. Black: no switching. White: switching. (a) No $\text{Pol}_\perp$ stray field. (b) Stray field applied.

$J = 2.83 \times 10^{11}\text{A/m}^2$ that seemed to be an anomaly in the FD simulations is also found in the FEM simulations. The critical current is also the same, still slightly lower when there is the $\text{Pol}_\perp$ stray field. However, there is a discrepancy at very high currents for the SAF-$\text{Pol}_\perp$. feeLLGood simulations exhibits a non-coherent behaviour showing that a large current may lead to instabilities, even in the absence of the dipolar field.

Time traces

Time traces of feeLLGood and ST_GL-FFT simulations are similar but do not exhibit a perfect agreement. It is clear, from figure 4.13, that the initial and final states found by the solvers are different. In between, the variation of the magnetisation appears to be very similar.

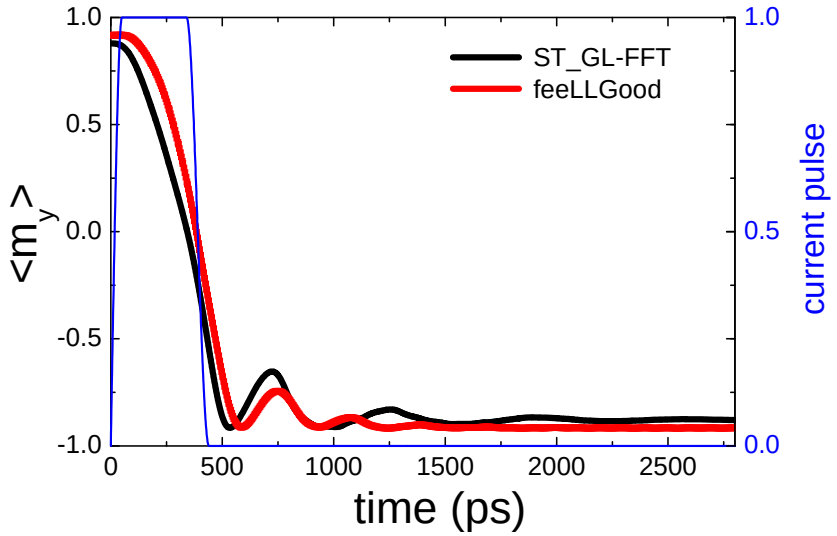

Figure 4.13: Time of traces of STT precessional switching at $J = 1.33 \times 10^{11}\text{A/m}^2$ and $\Delta t = 290\,\text{ps}$.

Since the discrepancy between feeLLGood and ST_GL-FFT seems to originate from a difference in the equilibrium states, these are presented in the next section.

Comparison of initial configurations

The simulations start from an equilibrium state aligned along the easy axis. The configuration is not uniform, since surface magnetostatic charges constrain the magnetisation to follow the edge. The so-called *onion-state* is formed, as shown on figure 4.14. This initial state is one of the two ground states, since there exists a symmetric onion-state aligned in the opposite direction.

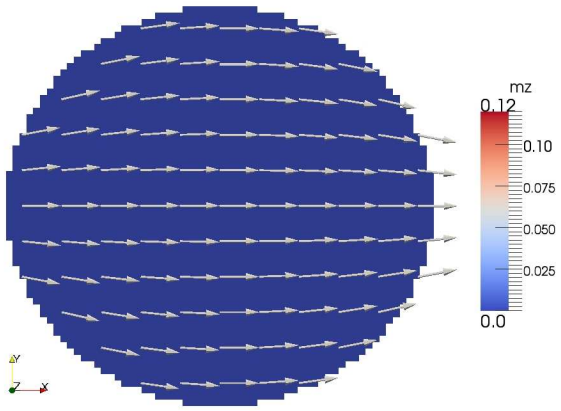

Figure 4.14: Ground state of the system in absence of $Pol_{\perp}$ stray field.

In absence of $Pol_{\perp}$ dipolar field, the two ground states along the easy-axis are found with ST_GL-FFT and feeLLGood. In contrast, when the stray field is on, feeLLGood still finds two ground states whereas ST_GL-FFT computations give four equivalent ground states. The ground states along +x are shown in figure 4.15.

The 'splitting' of the ground state observed in FD simulations is due to the staircase edge. This numerical artefact reminds us of the caution required when interpreting FD simulations. Fortunately, this difference of initial state almost does not affect the final result.

The influence of the analyser has been neglected because it is thought that, in STT precessional switching, the spin torque is mainly due to the perpendicular polariser. Therefore, for a reliable precessional switching, it is tempting to think that the polarisation of the analyser has to be as small as possible. In the next section, another point of view is explored: by increasing the polarisation of the analyser, a deterministic switching may be possible. This switching would combine the advantages of all-planar STT-MRAM and STT precessional switching.

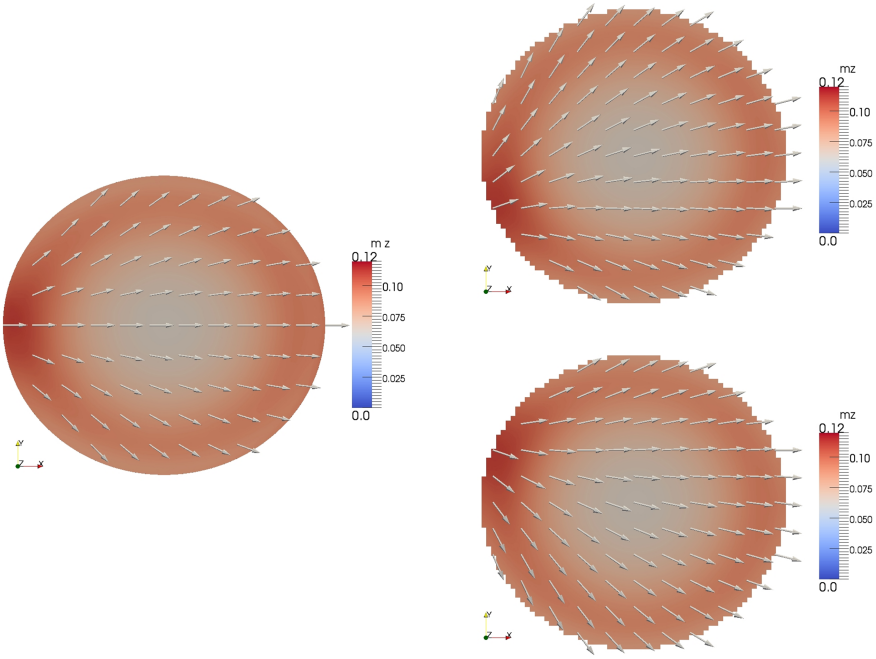

Figure 4.15: Equilibrium magnetisation states taking into account the polariser's stray field. Left-hand side: feeLLGood simulation shows a magnetisation directed along the easy axis. Right-hand: ST_GL-FFT computations exhibit a splitting of the ground state.

4.3 Deterministic switching with combined perpendicular and planar polarisers

Spin-torque-driven precessional switching is a very fast means of reversing magnetisation. Reliability problems have been discussed and we have seen that replacing polariser and analyser by SAFs can be a way to increase the switching probability. However, the exact duration of the current pulse and its amplitude have to be adjusted with a very high precision in order to obtain a reasonable switching probability. It turns out that random variations in sample characteristics always exist, even after an optimised nanofabrication process, which means that the exact parameters of the current pulse should be different for each memory cell. The problem of reliability is therefore not entirely solved. An ideal magnetic memory would combine both the speed of STT-precessional switching and the reliability of "all-planar" MRAM. In this section, we discuss a technological solution allowing to get closer to this ideal memory.

In ref [131], Rowlands *et al.* report on switching in double-MgO-barrier spin valves comprising both in-plane and out-of-plane polarisers. Switching is achieved in a time as short as 0.1 ns, which is the typical reversal time in precessional switching. However, the authors claim that they *[did] not observe oscillations of the switching probability with pulse duration.* The absence of these oscillations is *attributed to the influence of STT generated by the in-plane polariser.*

In ref [134], Hou *et al.* studies, with macrospin simulations, the response of the same system to a dc current. A state diagram is plotted varying the "strength" of each polariser. They draw the same conclusion as Rowlands *et al.*: deterministic switching can be observed if the strength of the in-plane polariser is (much) larger than the strength of the out-of-plane polariser. However, no quantitative criterion is given. In the following, we will try to determine the exact conditions in which direct switching can exist. We call *direct switching* or *deterministic switching* the magnetisation reversal under the action of STT from both in-plane and out-of-plane polarisers, such that there is no oscillation of the switching probability, and the magnetisation trajectory is similar to the one observed in precessional switching. In this type of switching, the final state depends on the current polarity. The whole analytical study will be conducted within the macrospin approximation.

4.3.1 Macrospin model

The physical principle of deterministic switching lies on the condition that the critical current to initiate IPP is smaller than the onset of OPP:

$$|J_{C\parallel}^{\pm}| < |J_{\perp}| \tag{4.5}$$

When the current is slightly larger than $|J_{C\parallel}^{\pm}|$ (onset of IPP), the magnetisation starts to oscillate. If the incursion angle of IPP is large enough, the additional torque generated by the out-of-plane polariser can be sufficient to reverse the magnetisation. Moreover, if the current is smaller than $J_{\perp}$, there is no OPP and the magnetisation relaxes around its new equilibrium position.

The expression of $J_{C\parallel}^{\pm}$ was mentioned earlier (equation 4.2) without distinction between positive and negative currents. In our convention (for positive current, electrons flow from the in-plane polariser to the free layer), the critical currents with in-plane polariser write [88, 114, 126]

$$J_{C\parallel}^{-} = -\alpha \frac{2e}{\hbar} \frac{\mu_0 M_s t}{g(\theta = 0, \eta_{\parallel})} \left(H_K + \frac{M_s}{2} \right) \tag{4.6}$$

$$J_{C\parallel}^{+} = +\alpha \frac{2e}{\hbar} \frac{\mu_0 M_s t}{g(\theta = \pi, \eta_{\parallel})} \left(H_K + \frac{M_s}{2} \right) \tag{4.7}$$

$$\tag{4.8}$$

where $J_{C\parallel}^{-}$ is the critical current for negative current, and $J_{C\parallel}^{+}$ corresponds to a positive current.

The expression of $J_{\perp}$ given in equation 4.2, as well as the expressions of $J_{C\parallel}^{\pm}$ (4.6 and 4.7) were derived considering only one polariser. Assuming that each critical current is not influenced by the addition of a second polariser, one can consider that these expressions are still valid in the case of a free layer magnetisation driven by both in-plane and out-of-plane polarisers.

Noting that the condition 4.5 is equivalent to $\frac{|J_\perp|}{|J^{\pm}_{C\parallel}|} > 1$, one can write

$$\frac{|J_\perp|}{|J^{-}_{C\parallel}|} = \frac{1}{\alpha} \times \frac{1}{2+\frac{1}{Q}} \times \frac{g(\theta=0,\eta_\parallel)}{g(\theta=\frac{\pi}{2},\eta_\perp)} > 1 \tag{4.9}$$

$$\frac{|J_\perp|}{|J^{+}_{C\parallel}|} = \frac{1}{\alpha} \times \frac{1}{2+\frac{1}{Q}} \times \frac{g(\theta=\pi,\eta_\parallel)}{g(\theta=\frac{\pi}{2},\eta_\perp)} > 1 \tag{4.10}$$

where $Q = H_K/M_s$, with H_K the anisotropy field originating from magnetocrystalline and shape anisotropies. In thin films, within macrospin approximation,

$$H_K = \frac{2K_u}{\mu_0 M_s} + (N_{yy} - N_{xx})M_s, \tag{4.11}$$

therefore,

$$Q = \frac{2K_u}{\mu_0 M_s^2} + (N_{yy} - N_{xx}). \tag{4.12}$$

In practical cases, $Q \ll 1$. Therefore, equations 4.9 and 4.10 become

$$\frac{|J_\perp|}{|J^{-}_{C\parallel}|} = \frac{Q}{\alpha} \times \frac{g(\theta=0,\eta_\parallel)}{g(\theta=\frac{\pi}{2},\eta_\perp)} > 1 \tag{4.13}$$

$$\frac{|J_\perp|}{|J^{+}_{C\parallel}|} = \frac{Q}{\alpha} \times \frac{g(\theta=\pi,\eta_\parallel)}{g(\theta=\frac{\pi}{2},\eta_\perp)} > 1 \tag{4.14}$$

Using the formula 1.104 for the spin efficiency $g(\eta,\theta)$, and setting for instance $\eta_\perp = 0.3$, one can then draw the plots of $|J_\perp|/|J^{\pm}_{C\parallel}|$ as a function of $\eta_\parallel$ and Q/α (Fig. 4.16).

The white region in the diagram 4.16 indicates that $|J_\perp|/|J^{\pm}_{C\parallel}| > 1$ and therefore that a deterministic switching should be possible. However, it does not indicate the range of current where this switching exists, it just tells that such a current exists. We only know that the current density J must fulfil the condition

$$|J^{\pm}_{C\parallel}| < |J| < |J_\perp|. \tag{4.15}$$

The figure 4.16 shows that the deterministic switching is easier for $J > 0$. Since the white region of figure 4.16a is smaller than the white region of figure 4.16b, the condition of deterministic switching for both polarities is determined only by the diagram $J < 0$: at given $\left(\eta_\parallel, \frac{Q}{\alpha}\right)$, if deterministic switching is possible for $J < 0$, then it is possible for $J > 0$. In fact, the figure tells us what have to be the aspect ratio of the free layer (directly related to Q/α) and the relative strengths of the two polarisers. Bipolar switching can be achieved in structures with a large aspect ratio (i.e. large Q) and a strong polarisation of the in-plane polariser. It is therefore not surprising that it was observed by Rowlands

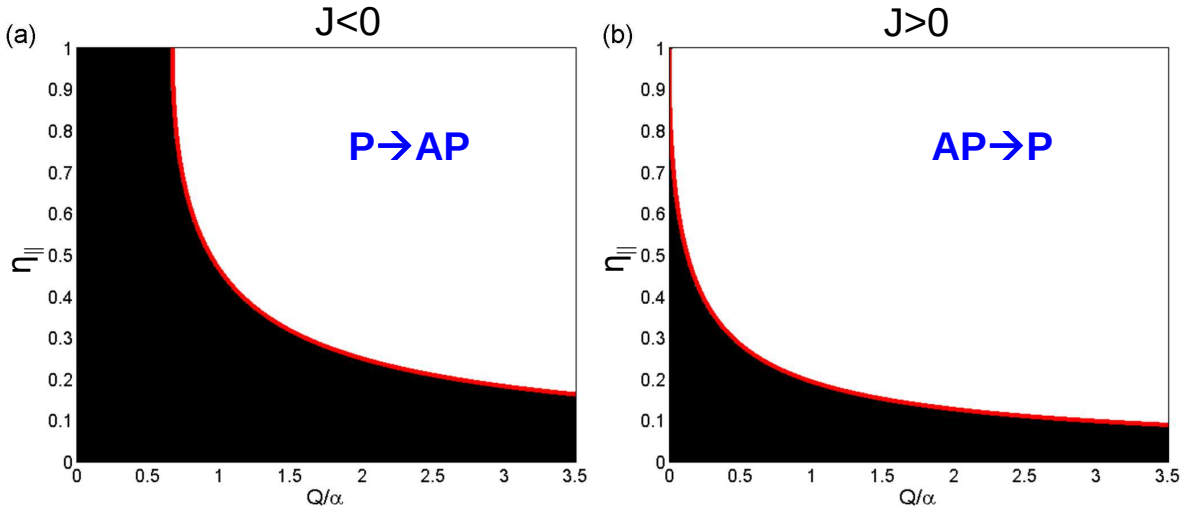

Figure 4.16: The ratio $|J_\perp|/|J_{C\parallel}^{\pm}|$ is >1 in the white area (deterministic switching is possible), and <1 in the black area (deterministic switching impossible). (a) $J < 0$; the white area corresponds to possibility of switching from Parallel to Anti-Parallel state. (b) $J > 0$; the white area corresponds to possibility of switching from Anti-Parallel to Parallel state. In the black areas, a dc current should lead to IPS state or OPP oscillation or OPS state. Here, the polarisation of the out-of-plane polariser is set to $\eta_\perp = 0.3$.

et al. [131] in double MgO tunnel junction of 180 nm×70 nm lateral size. It is worth mentioning that a low α also favours bipolar switching.

4.3.2 Macrospin simulations

Checking the diagram 4.16 by simulations would require not only to vary the aspect ratio (hence Q/α) and the polarisation $\eta_\parallel$ of the planar polariser, but also to vary J over a large range. At given Q/α and $\eta_\parallel$, if there exists a current density J such that deterministic switching is found (i.e. switching under dc current), then the values of Q/α and $\eta_\parallel$ should be found in the white region of figure 4.16.

Due to the length of such series of simulations, only a few were performed to see the effect of a large aspect ratio and a large planar polarisation. The macro-spin free layer is 200 nm × 50 nm × 2.5 nm, with $\alpha = 0.015$, resulting in a ratio $Q/\alpha = 5$ (far right in the diagrams of figure 4.16). The polarisations of the fixed layers are $\eta_\perp = 0.3$ and $\eta_\parallel = 0.7$. Starting from the parallel state in the simulations with $J < 0$ and from the anti-parallel state when $J > 0$, a dc current is applied. Switching is found for both polarities (figure 4.17), confirming that $\left(\frac{Q}{\alpha},\ \eta_\parallel\right) = (5,\ 0.7)$ is in the white areas of figure 4.16. Moreover, the amplitude of the threshold current for AP → P switching is smaller than for P → AP switching, complying thus with the previous comments on the asymmetry of the current.

On the other hand, simulations reveal a complex magnetisation dynamics. As shown on figure 4.17 a, for $J > 0$, switching does not occur at some particular currents but appears again for some larger ones. In contrast, for $J < 0$, beyond the critical current, all the simulations exhibit deterministic switching; the OPP threshold being too large

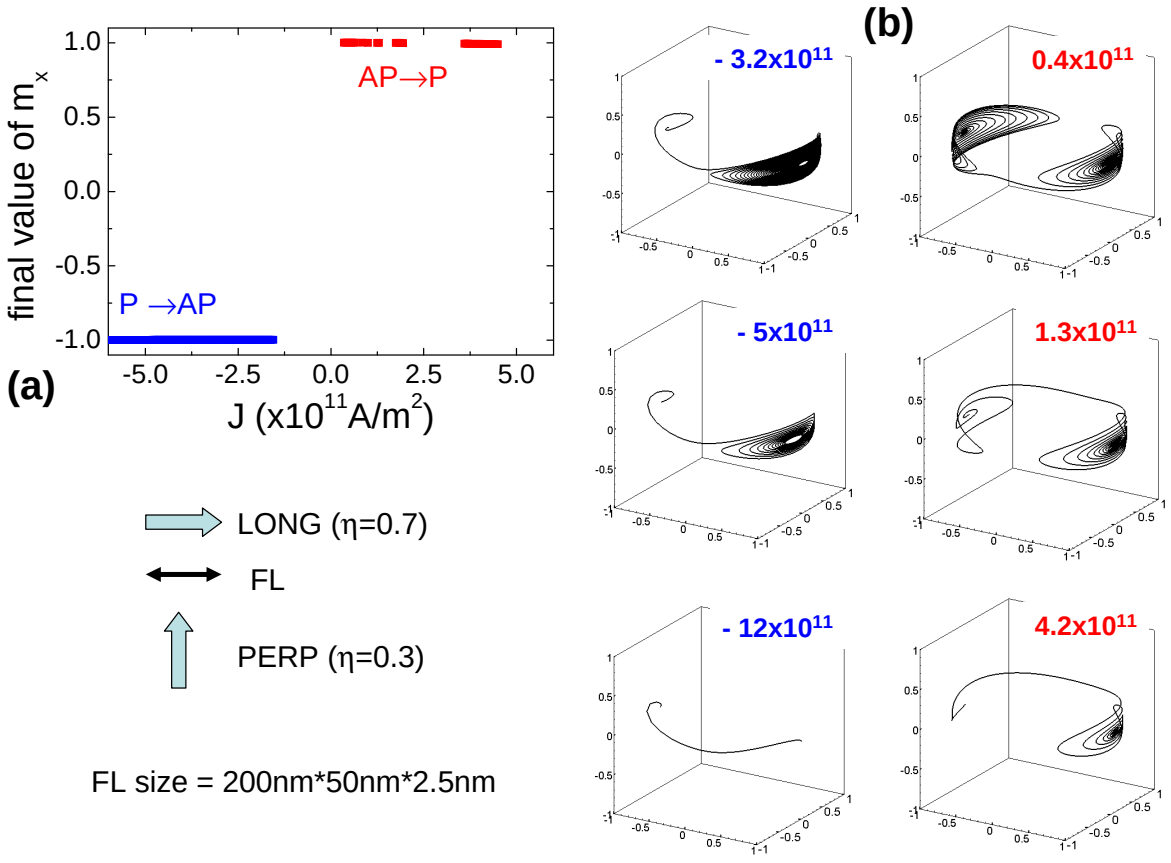

Figure 4.17: Macrospin simulations of free layer magnetisation dynamics driven by the spin torques originating from a planar polariser ($\eta_{\|} = 0.7$) and a perpendicular polariser ($\eta_{\|} = 0.3$). (a) Final values of m_x (component along the easy axis); blue (and red) points represent switching from Parallel to Anti-Parallel state (and Anti-Parallel to Parallel state). (b) Magnetisation trajectories for selected current values.

for such a large aspect ratio. Interestingly, ringing is very long at small currents (figure 4.17 b), whereas *ballistic switching* (as defined in section 4.1.1) is observed at $J = -12 \times 10^{11}\mathrm{A/m}^2$. To summarise, switching time is increased compared to the case when the influence of the planar polariser is negligible, but it can still be of the same order of magnitude at very large current amplitude. However, large current amplitude may give rise to complicated dynamics that is not deterministic anymore, especially for $AP \rightarrow P$ switching.

4.4 Conclusions of the chapter

The conclusions of this chapter are of interest for both numerics and applications.

Numerical aspects

Switching diagrams have been obtained for both feeLLGood and ST_GL-FFT. They are similar, with a slight discrepancy at large current amplitude and large pulse duration. In fact, a more obvious difference is found when computing the equilibrium states. In the case when the polariser stray field is applied, the ground state computed with ST_GL-FFT is split whereas it is not with feeLLGood. This splitting is not physical and results from the staircase-like edge. This artefact has not significantly affected the switching diagrams and the conclusions made for ST_GL-FFT remain true.

Applications

Switching in less than 1 ns has been demonstrated both experimentally and numerically. It has been shown that the coherence, hence the reliability, is improved if the polariser's stray field is suppressed. Therefore, compensated SAF should be used in this type of device.

However, for a very reliable switching, one must choose an analyser (called "in-plane polariser") with a larger polarisation. The magnetisation could then be reversed avoiding sustained OPP. The conditions favourable to this type of switching are summarised on a diagram.

Conclusion

Summary

The conclusions of this PhD thesis are of interest for both numerical micromagnetism and applications.

Conclusions on the numerical tools

A first-order version of feeLLGood with the spin torque term has been first tested on problem of perpendicular STO. It proved to be very reliable, despite its relatively slow speed. The comparison with the Finite Difference Method has shown an artefact of this method. In particular, meshing the staircase-edge geometry with tetrahedra and performing the simulations with feeLLGood (section 3.2.3), the ambiguity concerning the frequency jumps has been definitely raised. As a consequence, one can affirm that the Finite Element Method is much more reliable for round geometries.

The order 2 version of feeLLGood has been extensively used and compared to the order 1. A very good agreement has been found between the two versions, proving thus their reliability. However, one test (section 2.5.2) has shown a discrepancy between order 1 and order 2. The abnormally low IPP critical current of the order 2 version has shown that the dynamics is not computed accurately for small amplitude oscillations. The problem may simply arise from the time-stepper criterion that is not strict enough for such small precession angles. Another weak form, currently being implemented may help to solve this problem.

The two algorithms computing the demagnetising field (FMM and NFFT) have both been tested, and have exhibited similar results. In the simulations of Spin Torque Oscillators and STT-MRAM, only the FMM has been used. In fact, the meshes contain less than 10000 nodes and NFFT does not provide any advantage over FMM for such small meshes. Moreover, the memory required would have been larger.

Conclusions on applications

In the chapter 2, spin-torque-induced in-plane precessions have been studied. The frequency jumps observed in experiments have also been observed in the micromagnetic simulations. The macrospin model has been unable to explain the various frequency jumps, showing thus that they arise from the non-uniformity of the magnetisation. These

discontinuities do not only exist in the frequency curve, but also in the incursion angles of the trajectories, in the micromagnetic configurations and in the various energies. Spectral mapping techniques have been used to decompose the periodic magnetisation vector on a basis of harmonics. Doing so at each node of the mesh, the maps of local power have been plotted as well as the time-dependent decompositions. As a result, the frequency jumps have been found to be linked to the excitation of a new mode at certain harmonics (third harmonic in the transverse component, for branches 4 and 5), with a maximal amplitude just above the frequency jump. Discontinuities seem to occur when the self-frequency of the excited mode crosses one of the harmonics of the IPP oscillation. Computation of the normal modes of the system showed some similarities with the excited modes but an exact matching could not be found as the excited modes are strongly non-linear, with a large variation of their longitudinal component.

In the chapter 3, oscillations have been studied in a spin torque oscillator with perpendicular polariser and planar free layer. The first motivation of this study was to benchmark feeLLGood with the spin transfer torque. However, it turned out that the simulations were also of interest for applications. Interestingly, a branch has been found close the macrospin frequency curve, meaning that a large frequency tuneability may be possible. This is, of course, of great interest for applications since a wide range of frequency would be accessible only by tuning the current and in absence of applied field. Moreover, other oscillating modes have been found that and have been related to eigenmodes of the system.

In the chapter 5, a similar system has been simulated applying pulses of current instead of dc current. A switching has then been observed in a time as short as 100 ps. Two cases have been considered: with the polariser's stray field on the free layer, and without this field. The formation of a vortex at large current has shown that the magnetisation oscillation is much less coherent when the dipolar field of the polariser acts on the free layer. The improved switching probability observed experimentally is therefore explained and suggests improved results with a SAF-polariser.

Outlook

The PhD started with simulations of perpendicular Spin Torque Oscillator lasting at least three weeks. Moreover, only a few simulations could be run at the same time. The number of CPUs available has then grown and a much faster version of feeLLGood was implemented, resulting in an increased amount of simulation results. Developing a more accurate solver is still possible by working on a new order 2 time scheme. Moreover, parallel programming and GPU computation can also speed up micromagnetic simulations by more than ten times. On the other hand, the rapidity of micromagnetic codes already allows to deal with large systems, and more elaborate tools can now be developed to study a complex physics. In the systems addressed during this PhD, one could simulate dynamic coupling between free layer and polariser, for example. It would be also interesting to add the field-like torque or the thermal fluctuations. Unfortunately, there is

currently no model including the random field in the Finite Element Method.

Nonetheless, the complexity of spintronic devices is also due to the properties of electronic transport. The ballistic model is very useful because it gives an immediate expression of the spin torque, but was derived within a very restricted model and therefore does not hold in a general case. Instead, a diffusive model should be implemented and coupled with micromagnetism. This is already a work in progress in our group (PhD of Magali Sturma).

Bibliography

[1] D. Houssameddine, S. H. Florez, J. A. Katine, J.-P. Michel, U. Ebels, D. Mauri, O. Ozatay, B. Delaet, B. Viala, L. Folks, B. D. Terris, and M.-C. Cyrille. Spin transfer induced coherent microwave emission with large power from nanoscale MgO tunnel junctions. *Applied Physics Letters*, 93(2):022505, 2008.

[2] M. N. Baibish, J. M. Broto, A. Fert, F. Nguyen Van Dau, F. Petroff, P. Eitenne, G. Creuzet, A. Friederich, and J. Chazelas. Giant Magnetoresistance of (001)Fe/(001)Cr Magnetic Superlattices. *Physical Review Letters*, 61(21):2472–2475, 1988.

[3] G. Binasch, P. Grünberg, F. Saurenbach, and W. Zinn. Enhanced magnetoresistance in layered magnetic structures with antiferromagnetic interlayer exchange. *Physical Review B*, 39(7):4828–4830, March 1989.

[4] J. A. Katine, F. J. Albert, R. A. Buhrman, E. B. Myers, and D. C. Ralph. Current-driven magnetization reversal and spin-wave excitations in Co /Cu /Co pillars. *Physical Review Letters*, 84(14):3149–52, April 2000.

[5] Stuart S. P. Parkin, Masamitsu Hayashi, and Luc Thomas. Magnetic domain-wall racetrack memory. *Science*, 320(5873):190–4, April 2008.

[6] C. J. Garcia-Cervera, Z. Gimbutas, and E. Weinan. Accurate numerical methods for micromagnetics simulations with general geometries. *Journal of Computational Physics*, 184(1):37 – 52, 2003.

[7] H. Szambolics. *Nouvelles formulations elements finis pour le micromagnetisme et deplacement de parois par courant polarise en spin.* PhD thesis, 2008.

[8] E. Kritsikis. *Modelisation de la dynamique de l'aimantation par elements finis.* PhD thesis, 2011.

[9] I. Firastrau, D. Gusakova, D. Houssameddine, U. Ebels, M.-C. Cyrille, B. Delaet, B. Dieny, O. Redon, J.-Ch. Toussaint, and L. D. Buda-Prejbeanu. Modeling of the perpendicular polarizer-planar free layer spin torque oscillator: Micromagnetic simulations. *Physical Review B*, 78(2):024437, July 2008.

[10] D. Houssameddine, U. Ebels, B. Delaët, B. Rodmacq, I. Firastrau, F. Ponthenier, M. Brunet, C. Thirion, J.-P. Michel, L. Prejbeanu-Buda, M.-C. Cyrille, O. Redon, and B. Dieny. Spin-torque oscillator using a perpendicular polarizer and a planar free layer. *Nature materials*, 6(6):441–7, June 2007.

[11] A. Vaysset, C. Papusoi, L. D. Buda-Prejbeanu, S. Bandiera, M. Marins de Castro, Y. Dahmane, J.-C. Toussaint, U. Ebels, S. Auffret, R. Sousa, L. Vila, and B. Dieny. Improved coherence of ultrafast spin-transfer-driven precessional switching with synthetic antiferromagnet perpendicular polarizer. *Applied Physics Letters*, 98(24):242511, 2011.

[12] T.L. Gilbert. A Lagrangian formulation of the gyromagnetic equation of the magnetic field. *Physical Review*, 100(1243):1955, 1948.

[13] T.L. Gilbert. Classics in Magnetics A Phenomenological Theory of Damping in Ferromagnetic Materials. *IEEE Transactions on Magnetics*, 40(6):3443–3449, November 2004.

[14] L. Landau and E. Lifshits. On the theory of the dispersion of magnetic permeability in ferromagnetic bodies. *Phys. Z. Sowjetunion*, 8:153–169, 1935.

[15] J. Mallinson. On damped gyromagnetic precession. *IEEE Transactions on Magnetics*, 23(4):2003–2004, July 1987.

[16] William Brown. Thermal Fluctuations of a Single-Domain Particle. *Physical Review*, 130(5):1677–1686, June 1963.

[17] L. W. McKeehan and P. P. Cioffi. Magnetostriction in permalloy. *Physical Review*, 28:146 – 157, 1926.

[18] G.T. Rado and J. R. Weertmann. *J. Phys. Chem. Solids*, 11:315, 1959.

[19] M. Labrune and J. Miltat. Wall structures in ferro/antiferromagnetic exchange-coupled bilayers: a numerical micromagnetic approach. *Journal of Magnetism and Magnetic Materials*, 151(1-2):231–245, November 1995.

[20] L. Néel. L'anisotropie superficielle des substances ferromagnétiques. *Comptes-rendus de l'Académie des Sciences*, 237:1468–1470, 1953.

[21] L. Néel. Anisotropie magnétique superficielle et surstructures d'orientation. *Le Journal de Physique et le Radium*, 15(4):225 – 239, 1954.

[22] A. Hubert and R. Schäfer. *Magnetic Domains: The Analysis of Magnetic Microstructures*. Springer, 1998.

[23] J. Miltat and M. J. Donahue. *Handbook of magnetism and advanced magnetic materials*, volume 2, pages 742–764. Wiley-Interscience, 2007.

[24] B. A. Kalinikos and Andrei Slavin. dipole-exchange spin wave spectrum for ferromagnetic films with mixed exchange boundary conditions. *J.Phys.C:Solid State*, 19:7013–7033, 1986.

[25] A. G. Gurevich and G. A. Melkov. *Magnetization Oscillations and Waves*, chapter 7, pages 742–764. CRC Press, 1996.

[26] K. Y. Guslienko, S. O. Demokritov, B. Hillebrands, and A. N. Slavin. Effective dipolar boundary conditions for dynamic magnetization in thin magnetic stripes. *Physical Review B*, 66(13):8–11, October 2002.

[27] K. Y. Guslienko and A. N. Slavin. Boundary conditions for magnetization in magnetic nanoelements. *Physical Review B*, 72(1):1–5, July 2005.

[28] R. F. Soohoo. *Magnetic Thin Films*. Harper & Row, 1965.

[29] C. Kittel and Physical Review. Excitation of Spin Waves in a Ferromagnet by a Uniform rf Field. *Physical Review*, I(5):1295–1297, 1958.

[30] James Clerk Maxwell. *A Treatise on Electricity and Magnetism*, volume 2, §437 and 438. Clarendon Press, Oxford, 1881.

[31] B. O. Peirce. *Elements of the theory of the Newtonian potential function*. §69. Ginn and Company, 1902.

[32] C. L. B. Shuddemagen. The Demagnetizing Factors for Cylindrical Iron Rods. *Proceedings of the American Academy of Arts and Sciences*, 43(6):185–256, 1907.

[33] J. A. Osborn. Demagnetizing Factors of the General Ellipsoid. *Physical Review*, 67(11-12):351–357, 1945.

[34] P. Rhodes, G. Rowlands, and D. R. Birchall. *J. Phys. Soc. Japan*, 17:543, 1956.

[35] R. I. Joseph. *Journal of Applied Physics*, 37:4639, 1966.

[36] D.-X. Chen, J. A. Brug, and R. B. Goldfarb. *IEEE Transactions on Magnetics*, 27:3601, 1991.

[37] P. Rhodes and G. Rowlands. *Proc. Leeds Phil. Soc.*, 6:191, 1954.

[38] M Beleggia, M De Graef, and Y T Millev. The equivalent ellipsoid of a magnetized body. *Journal of Physics D: Applied Physics*, 39(5):891–899, March 2006.

[39] E. C. Stoner and E. P. Wohlfarth. A mechanism of magnetic hysteresis in heterogeneous alloys. *Philosophical Transactions of the Royal Society of London. Series A, Mathematical and Physical Sciences*, 240(826):599–642, 1948.

[40] C. Kittel. *Introduction to solid state physics*. Wiley, 1956.

[41] J Slonczewski. Current-driven excitation of magnetic multilayers. *Journal of Magnetism and Magnetic Materials*, 159(1-2):L1–L7, June 1996.

[42] L Berger. Emmission of spin waves by a magnetic multilayer transversed by a current. *Physical Review B*, 54(13):9353–9358, 1996.

[43] M. Tsoi, A. G. M. Jansen, J. Bass, W. Chiang, M. Seck, V. Tsoi, and P. Wyder. Excitation of a Magnetic Multilayer by an Electric Current. *Physical Review Letters*, 80(19):4281–4284, 1998.

[44] J.Z Sun. Current-driven magnetic switching in manganite trilayer junctions. *Journal of Magnetism and Magnetic Materials*, 202(1):157–162, June 1999.

[45] E. B. Myers, D. C. Ralph, J. A. Katine, R. N. Louie, and R. A. Buhrman. Current-Induced Switching of Domains in Magnetic Multilayer Devices. *Science*, 285(5429):867–870, August 1999.

[46] F. J. Albert, J. A. Katine, R. A. Buhrman, and D. C. Ralph. Spin-polarized current switching of a Co thin film nanomagnet. *Applied Physics Letters*, 77(23):3809, 2000.

[47] J. Grollier, V. Cros, A. Hamzic, J. M. George, H. Jaffres, A. Fert, G. Faini, J. Ben Youssef, and H. Legall. Spin-polarized current induced switching in Co/Cu/Co pillars. *Applied Physics Letters*, 78(23):3663, 2001.

[48] J. Z. Sun, D. J. Monsma, D. W. Abraham, M. J. Rooks, and R. H. Koch. Batch-fabricated spin-injection magnetic switches. *Applied Physics Letters*, 81(12):2202, 2002.

[49] E. Myers, F. Albert, J. Sankey, E. Bonet, R. Buhrman, and D. Ralph. Thermally Activated Magnetic Reversal Induced by a Spin-Polarized Current. *Physical Review Letters*, 89(19):196801, October 2002.

[50] A. A. Tulapurkar, T. Devolder, K. Yagami, P. Crozat, C. Chappert, A. Fukushima, and Y. Suzuki. Subnanosecond magnetization reversal in magnetic nanopillars by spin angular momentum transfer. *Applied Physics Letters*, 85(22):5358, 2004.

[51] J. Slonczewski. US Patent No. 5695864, 1997.

[52] S. I. Kiselev, J. C. Sankey, I. N. Krivorotov, N. C. Emley, R. J. Schoelkopf, R. A. Buhrman, and D. C. Ralph. Microwave oscillations of a nanomagnet driven by a spin-polarized current. *Nature*, 425(6956):380–383, September 2003.

[53] Jiang Xiao, A. Zangwill, and M. D. Stiles. Macrospin models of spin transfer dynamics. *Physical Review B*, 72(1):014446, July 2005.

[54] M. D. Stiles and A. Zangwill. Anatomy of spin-transfer torque. *Physical Review B*, 66(1):014407, June 2002.

[55] Maciej Zwierzycki, Yaroslav Tserkovnyak, Paul Kelly, Arne Brataas, and Gerrit Bauer. First-principles study of magnetization relaxation enhancement and spin transfer in thin magnetic films. *Physical Review B*, 71(6):064420, February 2005.

[56] F. Albert, N. Emley, E. Myers, D. Ralph, and R. Buhrman. Quantitative Study of Magnetization Reversal by Spin-Polarized Current in Magnetic Multilayer Nanopillars. *Physical Review Letters*, 89(22):226802, November 2002.

[57] S. Zhang and Z. Li. Roles of Nonequilibrium Conduction Electrons on the Magnetization Dynamics of Ferromagnets. *Physical Review Letters*, 93(12):127204, September 2004.

[58] S. Zhang, P. Levy, and A. Fert. Mechanisms of Spin-Polarized Current-Driven Magnetization Switching. *Physical Review Letters*, 88(23):236601, May 2002.

[59] In Silicio. http://www.insilicio.fr/.

[60] M. J. Donahue and D. G. Porter. *OOMMF User's Guide, Version 1.0*. National Institute of Standards and Technology, Gaithersburg, MD, September 1999. Interagency Report NISTIR 6376, http://math.nist.gov/oommf/.

[61] M. D. Scheinfein. http://llgmicro.home.mindspring.com/.

[62] D. V. Berkov and N. L. Gorn. http://www.micromagus.de/.

[63] A. Vansteenkiste and B. Van de Wiele. MuMax: A new high-performance micromagnetic simulation tool. *Journal of Magnetism and Magnetic Materials*, 323(21):2585–2591, November 2011.

[64] L. Torres and E. Martinez. http://www.goparallel.net/.

[65] A. Drews. http://micromagnum-tis.informatik.uni-hamburg.de/.

[66] M. J. Donahue. A variational approach to exchange energy calculations in micromagnetics. *Journal of Applied Physics*, 83(11):6491, 1998.

[67] A. E. LaBonte. Two-Dimensional Bloch-Type Domain Walls in Ferromagnetic Films. *Journal of Applied Physics*, 40(6):2450, 1969.

[68] M. Schabes and A. Aharoni. Magnetostatic interaction fields for a three-dimensional array of ferromagnetic cubes. *IEEE Transactions on Magnetics*, 23(6):3882–3888, November 1987.

[69] Manfred E. Schabes and H. Neal Bertram. Magnetization processes in ferromagnetic cubes. *Journal of Applied Physics*, 64(3):1347, 1988.

[70] Jian-Gang Zhu and H. Neal Bertram. Micromagnetic studies of thin metallic films (invited). *Journal of Applied Physics*, 63(8):3248, 1988.

[71] Samuel W. Yuan, H. Neal Bertram, and H Neal Bertram. Domain-wall dynamic transitions in thin films. *Physical Review B*, 44(22):12395–12405, 1991.

[72] A. Fabian, W. Kirchner, F. Williams, T. Heider, A. Leibl, and Hubert. Three-dimensional micromagnetic calculations of magnetite using fft. *Geophys. J. Int.*, 124:89, 1996.

[73] R. D. McMichael, M. J. Donahue, D. G. Porter, and Jason Eicke. Comparison of magnetostatic field calculation methods on two-dimensional square grids as applied to a micromagnetic standard problem. *Journal of Applied Physics*, 85(8):5816, 1999.

[74] L. Buda. *Développement d'un code de calcul micromagnétique 2D et 3D : application à des systèmes réels de types films, plots et fils.* PhD thesis, 2001.

[75] B. M. Kevorkian. *Contribution à la modélisation du retournement d'aimantation. Application à des systèmes magnétiques nanostructurés ou de dimensions réduites.* PhD thesis, 1998.

[76] O. Bottauscio and A. Manzin. www.inrim.it/~botta/Micromagnetics.html.

[77] D. R. Fredkin and Bo Yang. Dynamical micromagnetics by the finite element method. *IEEE Transactions on Magnetics*, 34(6):3842–3852, 1998.

[78] H. Szambolics, J.-C. Toussaint, L.D. Buda-Prejbeanu, F. Alouges, E. Kritsikis, and O. Fruchart. Innovative Weak Formulation for the Landau-Lifshitz-Gilbert Equations. *IEEE Transactions on Magnetics*, 44(11):3153–3156, November 2008.

[79] F. Alouges and P. Jaisson. Convergence of a finite element discretization for the landau-lifshitz equations in micromagnetism. *Mathematical Models and Methods in Applied Sciences*, 16:299–313, 2006.

[80] S. Bartels. Stability and convergence of finite-element approximation schemes for harmonic maps. *SIAM J. Numer. Anal.*, 43(1):220–238, 2005.

[81] François Alouges, Evaggelos Kritsikis, and Jean-Christophe Toussaint. A convergent finite element approximation for Landau-Lifschitz-Gilbert equation. *Physica B: Condensed Matter*, 407(9):1345–1349, May 2012.

[82] D. Potts, G. Steidl, and M. Tasche. *Fast Fourier transforms for nonequispaced data: A tutorial*, pages 247–270. Birkhäuser, Boston, 2001.

[83] Evaggelos Kritsikis, Jean-Christophe Toussaint, Olivier Fruchart, Helga Szambolics, and Liliana Buda-Prejbeanu. Fast computation of magnetostatic fields by nonuniform fast Fourier transforms. *Applied Physics Letters*, 93(13):132508, 2008.

[84] L. Greengard and V. Rokhlin. A Fast Algorithm for Particle Simulations. *Journal of Computational Physics*, 135(2):280–292, August 1997.

[85] L. Greengard. *The rapid evaluation of potential fields in particle systems.* MIT Press, Cambridge, 1988.

[86] E. Kritsikis, A. Vaysset, L. D. Buda-Prejbeanu, F. Alouges, and J.-C. Toussaint. Beyond first-order finite element schemes in micromagnetics. *Journal of Computational Physics*, 256:357–366, January 2014.

[87] R. D. McMichael. http://www.ctcms.nist.gov/~rdm/mumag.org.html.

[88] J. Z. Sun. Spin-current interaction with a monodomain magnetic body: A model study. *Physical Review B*, 62(1):570–578, July 2000.

[89] M. D. Stiles and J. Miltat. Spin Transfer Torque and Dynamics.

[90] D. V. Berkov and J. Miltat. Spin-torque driven magnetization dynamics: Micromagnetic modeling. *Journal of Magnetism and Magnetic Materials*, 320(7):1238–1259, April 2008.

[91] S. I. Kiselev, J. C. Sankey, I. N. Krivorotov, N. C. Emley, M. Rinkoski, C. Perez, R. A. Buhrman, and D. C. Ralph. Current-Induced Nanomagnet Dynamics for Magnetic Fields Perpendicular to the Sample Plane. *Physical Review Letters*, 93(3):036601, July 2004.

[92] W. Rippard, M. Pufall, S. Kaka, T. Silva, and S. Russek. Current-driven microwave dynamics in magnetic point contacts as a function of applied field angle. *Physical Review B*, 70(10):100406, September 2004.

[93] P. K. Muduli, O. G. Heinonen, and Johan Å kerman. Decoherence and Mode Hopping in a Magnetic Tunnel Junction Based Spin Torque Oscillator. *Physical Review Letters*, 108(20):207203, May 2012.

[94] I. N. Krivorotov, N. C. Emley, J. C. Sankey, S. I. Kiselev, D. C. Ralph, and R. A. Buhrman. Time-domain measurements of nanomagnet dynamics driven by spin-transfer torques. *Science (New York, N.Y.)*, 307(5707):228–231, January 2005.

[95] D. Gusakova, M. Quinsat, J. F. Sierra, U. Ebels, B. Dieny, L. D. Buda-Prejbeanu, M.-C. Cyrille, V. Tiberkevich, and A. N. Slavin. Linewidth reduction in a spin-torque nano-oscillator caused by non-conservative current-induced coupling between magnetic layers. *Applied Physics Letters*, 99(5):052501, 2011.

[96] Kiwamu Kudo, Tazumi Nagasawa, Hirofumi Suto, Tao Yang, Koichi Mizushima, and Rie Sato. Influence of dynamical dipolar coupling on spin-torque-induced excitations in a magnetic tunnel junction nanopillar. *Journal of Applied Physics*, 111(7):07C906, 2012.

[97] B. Montigny. *Transfert de spin et dynamique de l'aimantation.* PhD thesis, 2007.

[98] I. Krivorotov, D. Berkov, N. Gorn, N. Emley, J. Sankey, D. Ralph, and R. Buhrman. Large-amplitude coherent spin waves excited by spin-polarized current in nanoscale spin valves. *Physical Review B*, 76(2):024418, July 2007.

[99] G. Siracusano, G. Finocchio, A. La Corte, G. Consolo, L. Torres, and B. Azzerboni. Nonstationary magnetization dynamics driven by spin transfer torque. *Physical Review B*, 79(10):104438, March 2009.

[100] G. Finocchio, G. Siracusano, V. Tiberkevich, I. N. Krivorotov, L. Torres, and B. Azzerboni. Time-domain study of frequency-power correlation in spin-torque oscillators. *Physical Review B*, 81(18):184411, May 2010.

[101] J. C. Goswami and A. K. Chan. *Fundamentals of Wavelets: Theory, Algorithms and Applications*. Wiley, New York, 2000.

[102] R. D. McMichael and M. D. Stiles. Magnetic normal modes of nanoelements. *Journal of Applied Physics*, 97(10):10J901, 2005.

[103] Mario Carpentieri, Marco Ricci, Pietro Burrascano, and Luis Torres. Spreading sequences for fast switching process in spin-valve nanopillars. *Applied Physics Letters*, 98(12):122504, 2011.

[104] V. Naletov, G. de Loubens, G. Albuquerque, S. Borlenghi, V. Cros, G. Faini, J. Grollier, H. Hurdequint, N. Locatelli, B. Pigeau, A. Slavin, V. Tiberkevich, C. Ulysse, T. Valet, and O. Klein. Identification and selection rules of the spin-wave eigenmodes in a normally magnetized nanopillar. *Physical Review B*, 84(22):224423, December 2011.

[105] U. Ebels, D. Houssameddine, I. Firastrau, D. Gusakova, C. Thirion, B. Dieny, and L. Buda-Prejbeanu. Macrospin description of the perpendicular polarizer-planar free-layer spin-torque oscillator. *Physical Review B*, 78(2):024436, July 2008.

[106] O. Klein, G. de Loubens, V. Naletov, F. Boust, T. Guillet, H. Hurdequint, A. Leksikov, A. Slavin, V. Tiberkevich, and N. Vukadinovic. Ferromagnetic resonance force spectroscopy of individual submicron-size samples. *Physical Review B*, 78(14):144410, October 2008.

[107] Th. Gerrits, H. A. M. Van Den Berg, J. Hohlfeld, L. Bär, and Th. Rasing. Ultrafast precessional magnetization reversal by picosecond magnetic field pulse shaping. *Nature*, 418(6897):509–512, August 2002.

[108] S. Kaka and S. E. Russek. Precessional switching of submicrometer spin valves. *Applied Physics Letters*, 80(16):2958, 2002.

[109] H. Schumacher, C. Chappert, R. Sousa, P. Freitas, and J. Miltat. Quasiballistic Magnetization Reversal. *Physical Review Letters*, 90(1):017204, January 2003.

[110] H. Schumacher, C. Chappert, P. Crozat, R. Sousa, P. Freitas, J. Miltat, J. Fassbender, and B. Hillebrands. Phase Coherent Precessional Magnetization Reversal in Microscopic Spin Valve Elements. *Physical Review Letters*, 90(1):017201, January 2003.

[111] C. Serpico, I. D. Mayergoyz, and G. Bertotti. Analytical solutions of Landau-Lifshitz equation for precessional switching. *Journal of Applied Physics*, 93(10):6909, 2003.

[112] W. Hiebert, L. Lagae, and J. De Boeck. Spatially inhomogeneous ultrafast precessional magnetization reversal. *Physical Review B*, 68(2):020402, July 2003.

[113] T. Devolder, J. Hayakawa, K. Ito, H. Takahashi, S. Ikeda, P. Crozat, N. Zerounian, Joo-Von Kim, C. Chappert, and H. Ohno. Single-Shot Time-Resolved Measurements of Nanosecond-Scale Spin-Transfer Induced Switching: Stochastic Versus Deterministic Aspects. *Physical Review Letters*, 100(5):057206, February 2008.

[114] Z. Li and S. Zhang. Magnetization dynamics with a spin-transfer torque. *Physical Review B*, 68(2):024404, July 2003.

[115] T. Devolder, C. Chappert, J. Katine, M. Carey, and K. Ito. Distribution of the magnetization reversal duration in subnanosecond spin-transfer switching. *Physical Review B*, 75(6):064402, February 2007.

[116] I. Krivorotov, N. Emley, R. Buhrman, and D. Ralph. Time-domain studies of very-large-angle magnetization dynamics excited by spin transfer torques. *Physical Review B*, 77(5):054440, February 2008.

[117] Y.-T. Cui, G. Finocchio, C. Wang, J. A. Katine, R. A. Buhrman, and D. C. Ralph. Single-Shot Time-Domain Studies of Spin-Torque-Driven Switching in Magnetic Tunnel Junctions. *Physical Review Letters*, 104(9):097201, March 2010.

[118] T. Devolder, C. Chappert, P. Crozat, A. Tulapurkar, Y. Suzuki, J. Miltat, and K. Yagami. Precharging strategy to accelerate spin-transfer switching below the nanosecond. *Applied Physics Letters*, 86(6):062505, 2005.

[119] Y.-T. Cui, J. Sankey, C. Wang, K. Thadani, Z.-P. Li, R. Buhrman, and D. Ralph. Resonant spin-transfer-driven switching of magnetic devices assisted by microwave current pulses. *Physical Review B*, 77(21):214440, June 2008.

[120] Samir Garzon, Longfei Ye, Richard Webb, Thomas Crawford, Mark Covington, and Shehzaad Kaka. Coherent control of nanomagnet dynamics via ultrafast spin torque pulses. *Physical Review B*, 78(18):180401, November 2008.

[121] T. Devolder, C. Chappert, and K. Ito. Subnanosecond spin-transfer switching: Comparing the benefits of free-layer or pinned-layer biasing. *Physical Review B*, 75(22):224430, June 2007.

[122] G. Finocchio, I. Krivorotov, L. Torres, R. Buhrman, D. Ralph, and B. Azzerboni. Magnetization reversal driven by spin-polarized current in exchange-biased nanoscale spin valves. *Physical Review B*, 76(17):174408, November 2007.

[123] T. Devolder, P. Crozat, J.-V. Kim, C. Chappert, K. Ito, J. A. Katine, and M. J. Carey. Magnetization switching by spin torque using subnanosecond current pulses assisted by hard axis magnetic fields. *Applied Physics Letters*, 88(15):152502, 2006.

[124] O. Redon, B. Dieny, and B. Rodmacq. US Patent No. 6532164, 2003.

[125] A. D. Kent, B. Ozyilmaz, and E. del Barco. Spin-transfer-induced precessional magnetization reversal. *Applied Physics Letters*, 84(19):3897, 2004.

[126] K. J. Lee, O. Redon, and B. Dieny. Analytical investigation of spin-transfer dynamics using a perpendicular-to-plane polarizer. *Applied Physics Letters*, 86(2):022505, 2005.

[127] Dmitri E. Nikonov, George I. Bourianoff, Graham Rowlands, and Ilya N. Krivorotov. Strategies and tolerances of spin transfer torque switching. *Journal of Applied Physics*, 107(11):113910, 2010.

[128] O. J. Lee, V. S. Pribiag, P. M. Braganca, P. G. Gowtham, D. C. Ralph, and R. A. Buhrman. Ultrafast switching of a nanomagnet by a combined out-of-plane and in-plane polarized spin current pulse. *Applied Physics Letters*, 95(1):012506, 2009.

[129] C. Papusoi, B. Delaet, B. Rodmacq, D. Houssameddine, J.-P. Michel, U. Ebels, R. C. Sousa, L. Buda-Prejbeanu, and B. Dieny. 100 ps Precessional Spin-Transfer Switching of a Planar Magnetic Random Access Memory Cell With Perpendicular Spin Polarizer. *Applied Physics Letters*, 95(7):072506, 2009.

[130] H. Liu, D. Bedau, D. Backes, J. A. Katine, J. Langer, and A. D. Kent. Ultrafast switching in magnetic tunnel junction based orthogonal spin transfer devices. *Applied Physics Letters*, 97(24):242510, 2010.

[131] G. E. Rowlands, T. Rahman, J. A. Katine, J. Langer, A. Lyle, H. Zhao, J. G. Alzate, A. A. Kovalev, Y. Tserkovnyak, Z. M. Zeng, H. W. Jiang, K. Galatsis, Y. M. Huai, P. Khalili Amiri, K. L. Wang, I. N. Krivorotov, and J.-P. Wang. Deep subnanosecond spin torque switching in magnetic tunnel junctions with combined in-plane and perpendicular polarizers. *Applied Physics Letters*, 98(10):102509, 2011.

[132] O. J. Lee, D. C. Ralph, and R. A. Buhrman. Spin-torque-driven ballistic precessional switching with 50 ps impulses. *Applied Physics Letters*, 99(10):102507, 2011.

[133] S. S. P. Parkin, D. Mauri, and Kasuya Yosida. Spin engineering:. *Physical Review B*, 44(13):7131–7134, 1991.

[134] Zhiwei Hou, Zongzhi Zhang, Jianwei Zhang, and Yaowen Liu. Modeling of spin-torque driven magnetization dynamics in a spin-valve with combined in-plane and out-of-plane polarizers. *Applied Physics Letters*, 99(22):222509, 2011.